SELF-ASSEMBLY OF PROTEIN-BASED SUPRASTRUCTURES

A Dissertation
Presented to
The Academic Faculty

by

Won Min Park

In Partial Fulfillment
of the Requirements for the Degree
Doctor of Philosophy in the
School of Chemical & Biomolecular Engineering

Georgia Institute of Technology
May 2015

SELF-ASSEMBLY OF PROTEIN-BASED SUPRASTRUCTURES

Approved by:

Dr. Julie A. Champion, Advisor
School of Chemical & Biomolecular Engineering
Georgia Institute of Technology

Dr. Julia E. Babensee
Wallace H. Coulter Department of Biomedical Engineering
Georgia Institute of Technology

Dr. Sven Holger Behrens
School of Chemical & Biomolecular Engineering
Georgia Institute of Technology

Dr. Andreas S. Bommarius
School of Chemical & Biomolecular Engineering
Georgia Institute of Technology

Dr. Athanassios Sambanis
School of Chemical & Biomolecular Engineering
Georgia Institute of Technology

Date Approved: January 14, 2015

Dedicated to my parents

ACKNOWLEDGEMENTS

I would like to thank my advisor, Dr. Julie Champion. Her guidance and encouragement greatly helped me finish this thesis, and her kindness and patience truly helped me overcome the hardest moment. I would also like to thank my committee members, Dr. Julia Babensee, Dr. Sven Behrens, Dr. Andreas Bommarius, and Dr. Athanassios Sambanis, for their helpful advice and suggestions.

I am also grateful to my lab members, Lina Herrera Estrada, Trudy Padmore, Anusha Garapaty, Kevin Ling, Timothy Chang, and Xingjie Zan. It was also a pleasure to work with undergraduate students, Phumthep Bunnak, Sterling Deng, and Christine Yee.

I wish to express my sincere appreciation to my parents. They have been always supportive to me, and I would not have been able to continue my study without their love and sacrifice. Also, I am very grateful to my sister, brothers-in-law, and parents-in-law. I would also like to thank all of my friends in South Korea and at Georgia Tech for their support. I would like to thank Mincheol Chang and Jonathan Park for their technical assistance and discussion.

Additionally, I would like to thank the funding organizations, the National Science Foundation (1032413) and GT Emory Center for Regenerative Engineering & Medicine. I acknowledge Dr. Nicholas Hud and the Hud lab members for use of CD.

Most importantly, I wish to thank my wife, Soo Young Jeon, and my adorable son, Daniel Junsu Park. She has been such a dedicated supporter, encouraging me all the time. She has sacrificed everything for me, and I appreciate every moment we have together. They are priceless gifts in my life, and I truly appreciate all of their love.

TABLE OF CONTENTS

LIST OF TABLES

Page

LIST OF FIGURES

LIST OF SYMBOLS AND ABBREVIATIONS

2D	two-dimensional
a	concentration proportionality factor
a_0	average head area
a_1	head area of globular domains
a_2	head area of coiled coils
ATR	attenuated total reflection
b	concentration proportionality factor
BP	band pass emission filter
C_{10}	alanylglycine-rich repeat
CD	circular dichroism
C	concentration
C_i	concentration for component i
d	diameter
D	diffusivity
D_i	diffusivity for component i
DIC	differential interference contrast
DLS	dynamic light scattering
DMSO	dimethyl sulfoxide
E_a	activation energy
ECM	extracellular matrix
EGFP	enhanced green fluorescent protein
ELP	elastin-like polypeptide
FBS	fetal bovine serum

FGF4	fibroblast growth factor 4
FITC	fluorescein isothiocyanate
FT-IR	Fourier transform infrared spectroscopy
GFP	green fluorescent protein
GST	glutathione S-transferase
IPTG	isopropyl β-D-1-thiogalactopyranoside
kbp	kilobase pair
k_c	rate constant for coacervation
K_d	dissociation constant
kDa	kilodalton
Kgp	lysine-specific gingipain
k_m	rate constant for maturation
k_{off}	rate constant for dissociation
k_{on}	rate constant for association
l_c	critical length
L	characteristic length for systems
LP	high pass emission filter
mCherry	monomeric Cherry fluorescence protein
MSD	mean-square displacement
MTT	3-4,5-dimethylthiazol-2-yl-2,5-diphenyltetrazolium bromide
NRMSD	normalized root-mean-square deviations
OD	optical density
P	packing parameter
PAR	protease-activated receptor
PBS	phosphate buffered saline

PCR	polymerase chain reaction
PDB	Protein Data Bank archive
RBS	ribosomal binding site
RFU	relative fluorescence units
Rgp	arginine-specific gingipain
RgpA	arginine-specific gingipain A
RgpB	arginine-specific gingipain B
SDM	site-directed mutagenesis
SDS-PAGE	tricine sodium dodecyl sulfate polyacrylamide gel electrophoresis
SEM	scanning electron microscope
T	temperature
TEM	transmission electron microscope
TNF-α	tumor necrosis factor-alpha
T_t	transition temperature
V	volume
YT	yeast extract and tryptone
Z_E	glutamic acid-rich leucine zipper
Z_R	arginine-rich leucine zipper
τ	lag time
τ_c	characteristic time for coacervation
τ_d	characteristic time for diffusion
χ	molar ratio

SUMMARY

Protein self-assembly is a versatile bottom-up strategy to build biological materials. It is mediated by non-covalent interactions, which are involved in formation of diverse biological materials in nature. Inspired by the principle, we developed strategies for self-assembly of protein-based suprastructures from recombinant protein building blocks. The suprastructures were designed as modular systems which enable incorporation folded functional proteins. Morphology of the suprastructures was manipulated into spheres, vesicles, nanosheets and porous particles, by engineering protein building blocks, controlling self-assembly processes, and combining inorganic nanocrystals into hybrid materials.

First, we demonstrated self-assembly of spherical protein coacervates in the extracellular matrix (ECM). It is an *in-situ* protein self-assembly system, which is mediated by spontaneous diffusion–coacervation and high-affinity binding of recombinant protein building blocks. The self-assembled protein particles are entrapped, shrank, and dissociated in the ECM, providing a potential as a "carrier-free" protein delivery system.

Second, we developed a strategy for self-assembly of vesicles from folded proteins. In aqueous solution, recombinant protein complex amphiphiles self-assembled into hollow vesicles via temperature-responsive inverse phase transition. Preferential encapsulation of various cargo can be achieved, which include protein coacervates, small molecules, and nanoparticles. Our strategy offers a versatile method to create protein-based delivery vehicles with biological functionality.

Third, self-assembly of 2D nanosheets was demonstrated. Under controlled processes, designed recombinant protein building blocks self-assembled into nanosheets. For example, drying method induced formation of large protein sheets. Also, full-length folded functional protein domains were able to be incorporated.

Lastly, we developed hierarchically structured porous protein-inorganic hybrid supraparticles. Self-clustering hybrid flower-shaped nanoparticles were prepared, and their assembly into porous particles with complex morphology was controlled at the air-water interface. The incorporated proteins in the hybrid material provide high-affinity binding sites. Various proteins can be immobilized, and we investigated immobilization of a protease. When immobilized, the enzyme showed enhanced inactivation of a pro-inflammatory cytokine, tumor necrosis factor-α (TNF-α).

Overall, we demonstrated new approaches to create protein-based suprastructures. Also, we provided fundamentals which are critical and specific for self-assembly of the developed suprastructures. The modular design approach for integration of diverse functional domains and the control in morphology offer opportunities for practical applications.

CHAPTER 1

INTRODUCTION

1.1 Self-Assembled Protein Biomaterials

Self-assembly is defined as the autonomous process during which components self-organize into structures.[1] It is mediated by non-covalent interactions including hydrogen bonds, electrostatic interactions, hydrophobic interactions, and van der Waals interactions.[2] Proteins are biopolymers which have weak non-covalent interactions to carry out biological functions. For example, receptor–ligand binding interactions regulate diverse biological processes,[3] and antibodies identify and neutralize antigens in the immune system.[4] In addition, structural scaffolds in the body are built from self-assembled proteins. In the extracellular matrix (ECM), collagens are present as self-assembled fibrils and provide mechanical strength.[5] Laminins are cross-shaped proteins that self-assemble into cell-associated networks in basement membranes.[6] Amelogenin, the ECM protein in dental enamel, undergoes stepwise assembly into high-order structures via cooperative interactions with minerals.[7] Indeed, protein self-assembly is how nature builds biological materials.

Natural protein biomaterials have been extensively used for regenerative medicine and tissue engineering.[8,9] However, direct harvest and use of these materials have shortcomings including limitations in tuning their properties,[10] long processing times with increasing cost of production,[11] and complexity associated with purification.[12] As an alternative, recombinant protein engineering offers a number of advantages. Recombinant DNA technology is a powerful tool to engineer proteins. Primary structure can be modified by changing the amino acid sequence, and it can lead to engineering of secondary, tertiary, quaternary structure, and the consequent function. Also, methods for

high-yield expression and purification of recombinant proteins have been established, providing benefits over natural proteins.[13,14]

Importantly, recombinant proteins can be customized to self-assemble into biomaterials with properties tuned for specific applications. Tuning of self-assembling protein domains can allow the subsequent control in the resulting material properties.[15] Also, multiple domains can be combined by a modular design approach. It enables incorporation of diverse structural and functional domains in a single protein building block.[10] The growing interest and advances in recombinant protein technology are predicted to allow creation of biomaterials with diverse and sophisticated physical and biological properties.

1.2 Biological Functionality of Biomaterials

Biological functionality of biomaterials is the requirement for effective regulation of signaling in biological environments. Elaboration of such materials that can manipulate biological signals has become a growing trend in biomaterial design.[12] In general, biological functionality of materials is achieved by incorporation of moieties for biological recognition that include cellular adhesion, receptor-binding, and proteolysis.[10,12,16] For example, presentation of cell-binding domains greatly influences cell morphology and behaviors.[17,18] Tethered growth factors regulates functions of cells that interact with the material.[19] A convenient strategy is incorporation of functional peptides.[10,16] They can be chemically conjugated to synthetic polymers or the specific amino acid sequences can be inserted into the sequence of peptides or proteins. There has been a rapid increase in the library of biofunctional domains, which continues to expand through repurposing of the original known functionality.[10]

On the other hand, biological functionality of full-length folded proteins can be superior to those from peptides. For example, biocatalytic properties are difficult to

achieve by incorporation of peptides. Although physical entrapment of folded proteins inside biomaterials can be a simple approach, sustained release of proteins is often required.[20] Chemical conjugation of proteins to materials can be an alternative, but the conjugation processes might hamper protein activity.[21] Self-assembly can be a powerful strategy for specific incorporation of folded proteins in biocompatible environments. Nevertheless, such strategies remain underdeveloped. A few recent studies have illustrated self-assembled protein biomaterials that carry full-length folded proteins, including enzymes, antigens,[22] and protein therapeutics.[23] This new approach has significant implications in development of biomaterials with enhanced biological functionality. It is predicted to offer new opportunities in tissue engineering, vaccination, and drug delivery.

1.3 Physical Properties of Biomaterials

Besides biological properties, physical properties of biomaterials have also been recognized to regulate biological responses.[24] There is a growing interest in size, shape, mechanical properties, and surface topology. New design parameters related to these physical properties of biomaterials can be used to control biological responses. For example, size of particles influences their biodistribution[25] and clearance[26] *in vivo*. Phagocytosis of particles by macrophages strongly depends on shape[27] and size,[28] as the local geometry of particles dictate initiation of internalization. Elasticity and stiffness of biomaterials has been reported to influence development and growth of cellular architecture.[29,30] Also, it has been established that surface topology plays a decisive role in cell morphology, adhesion or motility.[31]

Self-assembly is a versatile “bottom-up” strategy to fabricate biomaterials with controlled morphologies at nano- and micrometer length scales.[2] In nature, we can find many examples of self-assembled protein nano- and microstructures, including

microtubules, viruses, clathrin lattices, and actin filaments.[32] Similarly, protein motifs and domains have been engineered to self-assemble into artificial supramolecular architectures. Fibers,[33] cages,[34] lattices,[35] and even more complex structures[36] have been assembled from engineered protein building blocks. Furthermore, a computational method enabled the design of self-assembled protein nanostructures with high accuracy.[37] Although the tuned protein structures have been demonstrated in fundamental aspects, their structural features have a great potential in applications. In fact, self-assembled protein nanospheres have been successfully used for cancer treatment.[38]

1.4 Motivations and Objectives

As discussed in the previous sections, consideration of both biological and physical properties of protein biomaterial is essential for practical applications. However, development of self-assembled protein biomaterials has mainly focused on bulk materials such as hydrogels. Also, incorporation of folded proteins into building blocks is challenging because balancing self-assembling property and biological function in a single building block is difficult to achieve. For example, self-assembling proteins, which were created using protein design strategies, are lack of biological functionality,[35,37] or a simple type of assembly has only been achieved using functional proteins.[39] Therefore, nano- and microstructured colloidal protein particles that carry full-length folded proteins would be a new generation of biomaterials with enhanced control over both physical and biological properties. This approach can reduce the potential adverse effects such as toxicity concerns,[40] foreign body responses,[41] and immunogenicity,[12] which can be caused by use of synthetic or biological bulk materials. In a recent study, self-assembled protein nanoparticles containing a growth factor showed an enhanced performance in wound treatment, eliminating the use of scaffold materials.[39] In this thesis, I demonstrate development of protein-based colloidal suprastructures with controlled morphologies. It

is a generalized system that incorporates folded proteins as part of the building blocks. Self-assembly of recombinant protein can significantly simplify steps required for material fabrication. It also provides biocompatible environments which are necessary for use of folded proteins. Also, well-established methods are available for production of recombinant proteins in reasonable quantities.

The objectives of this thesis are summarized as: (1) creation and production of recombinant protein building blocks and understanding of their self-assembly into protein-based colloidal suprastructures, (2) development of a modular and generalized system to incorporate fully folded and functional proteins into the suprastructures, (3) control of their morphology at nano- and micrometer length scale, (4) use for a practical application.

1.5 Thesis Overview

To achieve the objectives, I designed and produced recombinant fusion proteins which combine different types of protein motifs and domains: leucine zipper coiled coils, elastin-like polypeptides, random coils, fluorescent proteins, and enzymes. Depending on the nature of protein building blocks or controls in self-assembly processes, the morphology of colloidal suprastructures was manipulated into spheres, vesicles, nanosheets, and porous particles. All of the suprastructures were created as modular systems that can integrate fusion proteins containing fully folded globular domains, demonstrated here with fluorescent proteins or enzymes.

In Chapter 2, a brief introduction of the protein motifs and domains used in this thesis is provided. Design rationales for the fusion proteins are discussed, followed by a description of experimental details for cloning, expression, and purification. In Chapter 3, a protein self-assembly strategy in the ECM is described. It is a concept of “carrier-free” protein delivery, where transport of proteins in the ECM is controlled by their self-

assembly inside the matrix. Chapter 4 illustrates the thermally triggered self-assembly of folded proteins into vesicles. They incorporate globular proteins in the vesicular membrane, and can encapsulate small molecules, proteins, and nanoparticles. Chapter 5 presents a strategy to fabricate protein nanosheets via template-assisted self-assembly. Chapter 6 describes hierarchically structured protein-inorganic hybrid supraparticles that are assembled from flower-shaped hybrid nanoparticles. In Chapter 7, Immobilization and characterization of a cysteine protease is demonstrated as an application for cytokine inactivation. In Chapter 8, contributions of this thesis are summarized, and recommended future work and guidelines for applications are provided.

CHAPTER 2

BIOSYNTHESIS OF RECOMBINANT FUSION PROTEINS

2.1 Biomimetic Protein Motifs

2.1.1 Coiled Coils

Coiled coils are superhelical protein motifs composed of two or more assembled α-helical peptides.[42] They are structural motifs that mediate oligomerization of subunits, and analysis indicates approximately 2–3% of all protein residues form coiled coils.[43,44] The primary structure of the coiled coil is the heptad repeat pattern $(abcdefg)_n$ where n is the number of repeats.[42] Hydrophobic amino acids are positioned at *a* and *d*, which form the tightly packed hydrophobic core of the coiled coils (Figure 2.1). Amino acids with complementary charged side groups occupy the positions *e* and *g*. The interaction of side chains at *e* and *g* forms the stabilizing interstrand salt bridge. Leucine zippers are dimeric coiled coils which mediate dimerization of the DNA binding domains (bZIP and bHLH-ZIP) in transcription factors.[45-47] Occupation of the position *d* by leucine residues is the characteristic of leucine zippers, which is critical for dimerization.[47,48] Among the artificially designed leucine zippers is a hetero-dimerizing leucine zipper pair that forms a strong complex with a dissociation constant $K_d \sim 10^{-15}$ M,[49] which compares to the affinity between streptavidin and biotin. The arginine-rich (Z_R) and glutamic acid-rich (Z_E) leucine zipper strands form stabilizing salt bridges between the arginine and glutamic acid residues located at positions *e* and *g* (Figure 2.1). Because of the exceptional affinity, the leucine zipper Z_E/Z_R has been utilized in the assembly of chimeric proteins for robust protein immobilization[50,51] and creation of biomolecular architectures.[52]

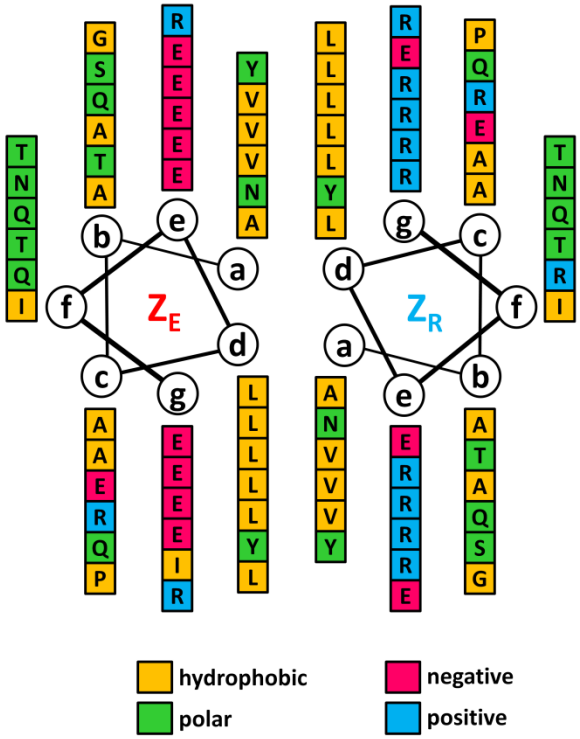

Figure 2.1 The helical wheel diagram for the heptad repeats of Z_E and Z_R.

2.1.2 Elastin-Like Polypeptides

Elastin-like polypeptides (ELPs) are artificial repetitive polypeptides derived from tropoelastin, which is predominantly found in the ECM.[53] Commonly, ELPs consist of pentapeptide repeats of $(VPGXG)_n$, where n is the number of repeats and X is a guest residue except proline. They undergo inverse phase transition from soluble to insoluble in aqueous phase when the temperature is elevated above the transition temperature (T_t).[54] The unordered conformation of ELP below T_t changes to β-turn above T_t.[55] This behavior can be affected by composition and length of the repeats, ELP concentration, and ionic strength.[56] Because of the attractive temperature-responsive properties, ELP-based

polypeptides have been extensively used for thermally triggered self-assembly of supramolecular structures including hydrogels, micelles, films, and fibers.[57]

2.1.3 Random Coils

Random coils are polypeptide chains with no regular secondary structures. An artificial random coil developed in the lab is the alanylglycine-rich repeat (C_{10}).[58] The repetitive sequence is $[(AG)_3PEG]_{10}$, and it has been characterized to be water soluble and lack regular secondary structures. Although poly(glycylalanine) is arranged antiparallel β-sheets in solid, the odd number of residues in the repeat frustrates formation of secondary structures. C_{10} is a flexible polyelectrolyte segment and has been used to connect coiled coils in protein building blocks that form protein hydrogels.[59,60] It retained water and prevented precipitation of the protein building blocks.

2.2 Design of Recombinant Fusion Proteins

In this thesis, the hetero-dimeric leucine zippers Z_E and Z_R are the most important protein motifs used in design of recombinant protein building blocks. The rationale is that the strand Z_E is combined with folded globular proteins so that fusion proteins containing Z_E can be integrated with self-assembling proteins containing Z_R to form suprastructures. In this concept, folded globular proteins are part of the protein building blocks and are incorporated into protein-based suprastructures. It is hypothesized that the extremely high affinity between Z_E and Z_R should be superior to any interactions between the folded globular proteins, offering a simple and robust strategy to integrate the chosen folded protein into suprastructures. That way, a modular and generalized platform can be realized, and it can incorporate a variety of biologically functional proteins including enzymes, growth factors, ligands, and cytokines.

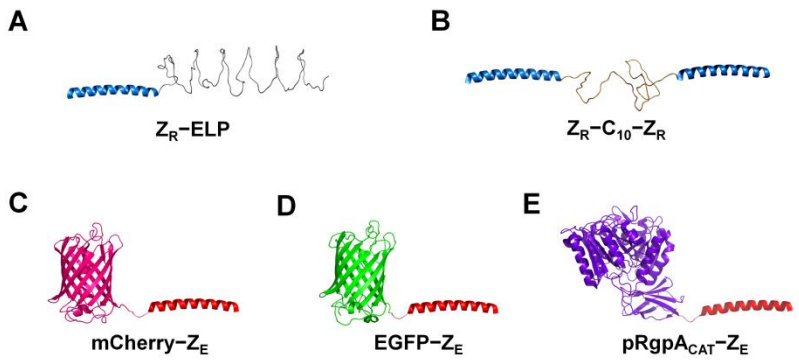

Figure 2.2 Recombinant fusion proteins. (A) Z_R–ELP, (B) Z_R–C_{10}–Z_R, (C) mCherry–Z_E, (D) EGFP–Z_E, (E) pRgpA$_{CAT}$–Z_E (PDB ID: 2H5Q for mCherry, 1EMK for EGFP, and 1CVR for RgpB which is a homolog to pRgpA$_{CAT}$).

Two proteins containing self-assembling domains were used to build protein suprastructures. First, a fusion protein of Z_R and ELP (Z_R–ELP[51]) was produced (Figure 2.2A). The inverse phase transition of ELP can be exploited for temperature dependent protein self-assembly. It is a diblock co-polypeptide with molecular weight of 17 kDa, and combination of the two blocks in a single protein provides temperature-responsive amphiphilicity. Second, two identical strands of Z_R were fused with the random coil fragment C_{10} to construct a triblock co-polypeptide, Z_R–C_{10}–Z_R (19 kDa) (Figure 2.2B). Attractive interactions between side chains of C_{10} under controlled processes can drive self-assembly of the building blocks, and its flexibility can be exploited to fabricate protein-inorganic hybrid suprastructures. Detailed strategies for self-assembly of specific suprastructures are described in Chapter 3, 4, 5, and 6.

The counterpart building blocks, which carry folded globular protein domains for biofunctionality, were also created. As model proteins, fluorescent proteins (mCherry[61] and EGFP[62]) were chosen. They are folded globular proteins that exhibit red and green

fluorescence, which are beneficial for characterization of the formed suprastructures and can be used for fundamental studies of their self-assembling characteristics. The glutamic acid-rich leucine zipper strand Z_E was fused to the C-termini of either mCherry or EGFP in the form of diblock fusion proteins, mCherry−Z_E or EGFP−Z_E (34 kDa) (Figure 2.2C,D). An affinity tag (His_6) was inserted at the C-termini of the fusion proteins and used for purification.

In the same way, an enzyme was also fused to Z_E. Particularly, the catalytic domain of a pathogenic cysteine protease RgpA was chosen as a potential therapeutic protein. Briefly, the protease RgpA is a virulence factor secreted from *Porphyromonas gingivalis*.[63] It is an arginine-specific protease and has shown proteolytic activity toward the pro-inflammatory cytokine, tumor necrosis factor-α (TNF-α).[64,65] The proteolytic inactivation of TNF-α is a promising property of RgpA to suppress inflammatory responses. The propeptide and catalytic domain of RgpA ($pRgpA_{CAT}$) was selected from the full-length enzyme, and Z_E was fused to the C-terminus of the catalytic domain to construct the fusion protein $pRgpA_{CAT}$−Z_E (Figure 2.2E). The C-terminus of the fusion protein was also tagged with His_6 for affinity chromatography.

Overall, two artificial self-assembling co-polypeptides and three fusion proteins containing folded globular protein domains were created and produced. Protein sequences for the five fusion proteins (Z_R−ELP, Z_R−C_{10}−Z_R, mCherry−Z_E, EGFP−Z_E, $pRgpA_{CAT}$−Z_E) are provided in Appendix A. Characterizations of self-assembling behaviors of the co-polypeptides will be provided in the following chapters.

2.3 Experimental Details

2.3.1 Materials

Oligonucleotide primers were synthesized by Eurofins MWG Operon, and DNA polymerase (PfuUltra II Fusion HS) was purchased from Agilent Technologies. The *E. coli* strains XL1-Blue (Agilent Technologies) and AFIQ-BL21 were kind gifts from Prof. D. Tirrell at California Institute of Technology. The plasmids containing Z_R−ELP, mCherry, and Z_E fragments were also kindly provided by Profs. D. Tirrell and K. Zhang (University of Minnesota). The plasmid containing EGFP was a gift from Prof. A. Bommarius at Georgia Institute of Technology. The chromosomal DNA of *P. gingivalis* W50 was a gift from Dr. Joe Aduse-Opoku at Queen Mary University of London. The expression vector pQE60 (3.4 kbp) and nickel nitrilotriacetic acid (Ni-NTA) resin were purchased from Qiagen.

2.3.2 Cloning

pQE60-$His_6Z_E/Z_R{-}C_{10}{-}Z_R$

The gene fragment for Z_R was PCR-amplified using primer pairs FZR1, RZR1 and FZR2, RZR2 (see Appendix C for all primer sequences). In a single step, the two types of resulting fragments for Z_R were ligated into the *NcoI* and *BglII* restriction sites of the pQE60 vector (3.4kbp). As a result, the plasmid pQE60-$Z_R{-}Z_R$ was constructed. Next, the restriction site *SalI* was inserted to a gift plasmid from Profs. A. Sugawara-Narutaki and D. Tirrell, by site-directed mutagenesis (SDM) using primers FSDM1 and RSDM1. Then, the C_{10} fragment was excised from the resulting plasmid by digestion using *HindIII* and *SalI*. The excised fragment was inserted between the two Z_R fragments in pQE60-$Z_R{-}Z_R$, where the *HindIII* site at the end of the $Z_R{-}Z_R$ fragment was removed by SDM using primers FSDM2 and RSDM2. Next, an additional DNA fragment, which

contains a ribosomal binding site (RBS) and the gene encoding His_6Z_E, was excised from the plasmid pQE60-His_6Z_E/Z_R−ELP by digestion with *EcoRI*, and inserted into the *EcoRI* site of pQE60-Z_R−C_{10}−Z_R plasmid. In the final step, a stop codon was inserted at the end of the gene encoding Z_R−C_{10}−Z_R by SDM with primers FSDM3 and RSDM3.

pQE60-mCherry−Z_E

The two gene fragments encoding either mCherry or Z_E were amplified by PCR using two pairs of primers FMF, RMF and FZE, RZE. The amplified fragments were assembled into a 0.9 kbp fragment that encodes mCherry-Z_E via PCR-assembly, and amplified using primers FMF and RZE. The resulting PCR product was digested using a single restriction enzyme, *BglII*, and ligated into the *BglII* restriction site of pQE60 (3.4kbp) vector. The sequence for C-terminal His_6 tag is provided in pQE60 vector.

pQE60-EGFP−Z_E

In the first step, two gene fragments encoding either EGFP or Z_E were amplified using two pairs of primers FEF, REF and FZE, RZE, respectively. In the second step, the amplified gene fragments were assembled by PCR-assembly, and amplified with primers FZE and RZE. The resulting DNA construct was digested and ligated into the *BglII* restriction site of the pQE60 vector.

pQE60-pRgpA$_{CAT}$−Z_E

The gene encoding pRgpA$_{CAT}$ was amplified from the chromosomal DNA of *P. gingivalis* W50, using primers FRGP and RRGP. Using PCR-assembly technique, the amplified gene fragment was assembled with the Z_E-encoding sequence that was PCR-amplified using primers FZE and RZE. In the following step, the assembled fragment for pRgpA$_{CAT}$−Z_E was amplified by PCR with primers FRGP and RZE. The 1.6 kbp fragment was digested and inserted between the *NcoI* and *BglII* restriction sites of the pQE60 vector.

2.3.3 Expression

Z_R−ELP, Z_R−C_{10}−Z_R, mCherry−Z_E, and EGFP−Z_E

Both Z_R−ELP and Z_R−C_{10}−Z_R were co-expressed with His_6Z_E to prevent degradation during expression.[51] The co-expressed His_6Z_E forms protein complexes His_6Z_E/Z_R−ELP or His_6Z_E/Z_R−C_{10}−Z_R, which are resistant to proteolysis in the cytoplasm. All plasmids (pQE60-His_6Z_E/Z_R−ELP, pQE60-His_6Z_E/Z_R−C_{10}−Z_R, pQE60-mCherry−Z_E, and pQE60-EGFP−Z_E) were transformed into *E.coli* strain AFIQ-BL21 for expression. All cell cultures were grown at 37°C in 2X yeast extract and tryptone (YT) media containing ampicillin (200 mg/L) and chloramphenicol (34 mg/L). When the cell culture optical density (OD) at 600 nm reached 0.8, protein expression was induced by 1.0 mM of isopropyl β-D-1-thiogalactopyranoside (IPTG). Cells were harvested by centrifugation after 5 hours of expression at 37°C.

$pRgpA_{CAT}$−Z_E

All plasmids pQE60-$pRgpA_{CAT}$−Z_E was transformed into *E.coli* strain AFIQ-BL21 for expression. Cell culture was grown at 37°C in 2X YT media containing ampicillin (200 mg/L) and chloramphenicol (34 mg/L). When the cell culture OD at 600 nm reached 0.6, the temperature was decreased to 30°C. Then, protein expression was induced by 0.2 mM IPTG. Cells were harvested by centrifugation after 20 min of expression at 30°C.

2.3.4 Purification

All recombinant fusion proteins were purified according to manufacturer instructions (Qiagen) except Z_R−ELP and Z_R−C_{10}−Z_R. Purified proteins were analyzed using tricine sodium dodecyl sulfate polyacrylamide gel electrophoresis (SDS-PAGE). In

order to avoid hydrolysis during boiling, all protein samples were prepared by reducing proteins at room temperature for 30 min.

Z_R−ELP and Z_R−C_{10}−Z_R

The harvested cells were centrifuged and resuspended in lysis buffer containing 8 M urea, 10 mM Tris-Cl, and 100 mM Na_2HPO_4 (pH 8.0), and lysed by a cycle of freezing-thawing and ultrasonication. After centrifugation, the cleared cell lysate containing complexes either His_6Z_E/Z_R−ELP or His_6Z_E/Z_R−C_{10}−Z_R was incubated with Ni-NTA resin. After washing at pH 6.3, either Z_R−ELP or Z_R−C_{10}−Z_R was collected from elution buffer containing 6 M guadinine hydrochloride, 10 mM Tris-Cl, and 100 mM Na_2HPO_4 (pH 8.0). The elution buffer isolated either Z_R−ELP or Z_R−C_{10}−Z_R from the complexes bound to the NTA resin. Purified proteins were dialyzed into deionized water.

mCherry−Z_E

According to manufacturer instructions, mCherry−Z_E was purified under the denaturing condition. All buffers contained 8 M urea, 10 mM Tris-Cl, and 100 mM Na_2HPO_4 and were adjusted to different pH values. Harvested cells were frozen, thawed, and sonicated in buffer at pH 8.0, and the cell lysate was cleared by centrifugation. The cleared cell lysate was incubated with Ni-NTA resin. After washing at pH 6.3, the protein was eluted from the resin at pH 4.5. After dialysis into phosphate buffered saline (PBS, pH 7.4), aggregates of insoluble protein were removed by centrifugation.

EGFP−Z_E and pRgpA$_{CAT}$−Z_E

According to manufacturer's instructions, either EGFP−Z_E or pRgpA$_{CAT}$−Z_E was purified under native conditions. All prepared buffers contained 50 mM Na_2HPO_4, 300 mM NaCl, and 10 − 250 mM imidazole at pH 8.0. After cell lysis by freeze-thaw and sonication, the cleared cell lysate in buffer containing 10 mM imidazole was incubated

with Ni-NTA, washed (20 mM imidazole), and eluted in the presence of 250 mM imidazole. The eluted solution was dialyzed into PBS (pH 7.4).

2.4 Results and Discussion

The Coomassie-stained SDS-PAGE images confirmed successful expression and purification of the fusion proteins. As observed in Figure 2.3A, the diblock and triblock co-polypeptides Z_R−ELP (17 kDa) and Z_R−C_{10}−Z_R (19 kDa) were purified. Although purified Z_R−C_{10}−Z_R appears at higher molecular weight (34 kDa) than prediction, it is consistent with previous work on an artificial co-polypeptide containing two strands of Z_R, which also runs at a higher molecular weight.[52] I hypothesize that the two Z_R strands connected by the linker chain C_{10} might dimerize even in the presence of SDS. It is known that Z_R forms the homodimer Z_R/Z_R with a dissociation constant $K_d \sim 10^{-7}$ M.[49] The yields for Z_R−ELP and Z_R−C_{10}−Z_R from 1L culture were approximately 200 mg and 45 mg, respectively. Expression and purification of the fusion proteins containing fluorescent proteins (mCherry−Z_E and EGFP−Z_E) was also analyzed using SDS-PAGE (Figure 2.3). Since the N=C bond of the chromophore of mCherry is hydrolyzed by boiling commonly performed during sample preparation,[66] unboiled mCherry−Z_E was analyzed. The fusion protein mCherry−Z_E (34 kDa) was very resistant to denaturation by SDS and urea, especially without boiling, showing fluorescence even in the gel. Therefore, the gel also contains partially folded mCherry−Z_E proteins, which exhibit different mobilities, but are still fluorescent (~45 kDa and ~30 kDa). EGFP−Z_E also appeared as the fully folded fraction (34 kDa) and partially folded fraction (slightly below 34 kDa) in the SDS-PAGE gel. Fluorescence from those protein bands confirmed that they are from either mCherry−Z_E or EGFP−Z_E, not impurities (Figure 2.3B,C).

Cysteine proteases are expressed as zymogens, which are combined with propeptide domains.[67] They are inactive but processed to active forms by cleavage of the

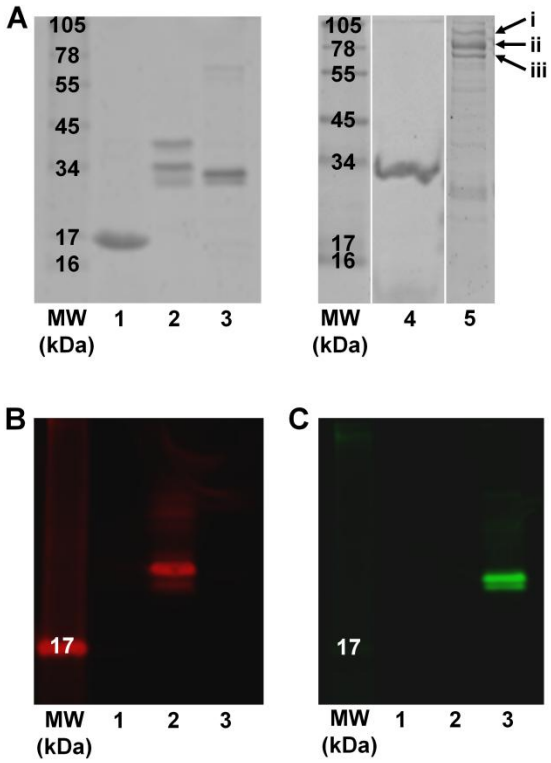

Figure 2.3 SDS-PAGE gel images from Coomassie Blue staining (A) and fluorescence of mCherry−Z_E (B) and EGFP−Z_E (C): Z_R−ELP (lane 1), mCherry−Z_E (lane 2), EGFP−Z_E (lane 3), Z_R−C_{10}−Z_R (lane 4), and pRgpA$_{CAT}$−Z_E (lane 5). Arrows in lane 5 indicate full-length (i), partially cleaved (ii), and fully cleaved pRgpA$_{CAT}$−Z_E (iii), respectively. Fluorescence from the protein bands was imaged at filter settings of excitation 532 nm/emission 610 nm (mCherry−Z_E) and excitation 488 nm/emission 526 nm (EGFP−Z_E).

N-terminal peptides. The propeptide domain of RgpA is also critical for folding of RgpA.[63] The full length 84 kDa $pRgpA_{CAT}{-}Z_E$ zymogen was purified. The intermediate with partially cleaved propeptide (72 kDa) and the mature enzyme with full cleavage of propetide (60 kDa) were also observed by SDS-PAGE (Figure 2.3A). The cleavage of the propeptide domain is known to be autolytically processed.[63] Thus, observation of the autolytic cleavage of the propeptide domain confirms that the purified $pRgpA_{CAT}{-}Z_E$ is properly folded with retained proteolytic activity.

2.5 Conclusion

In this chapter, biosynthesis of recombinant fusion proteins was demonstrated. Two artificial self-assembling co-polypeptides ($Z_R{-}$ELP, $Z_R{-}C_{10}{-}Z_R$) and three fusion proteins that carry folded globular protein domains (mCherry$-Z_E$, EGFP$-Z_E$, $pRgpA_{CAT}{-}Z_E$) were designed and produced. Proteolytic degradation of proteins containing Z_R was prevented by co-expression of His_6Z_E. The folded globular proteins were fused with Z_E using PCR-assembly, and the observed activities of mCherry, EGFP, $pRgpA_{CAT}$ indicate that this design approach can be extended to other folded functional proteins.

CHAPTER 3

TWO-STEP PROTEIN SELF-ASSEMBLY IN THE EXTRACELLULAR MATRIX[1]

3.1 Introduction

Therapeutic proteins require controlled delivery to the target tissue to maintain the local concentration over a prolonged period of time. A common approach is to delay protein release with a hydrogel matrix, which provides affinity interactions or diffusive barriers.[68] Physical entrapment of proteins in a matrix allows sustained release due to free volume, hydrodynamic drag, and obstruction effects.[69] Affinity-based approaches exploit specific binding interactions between natural[70] or engineered binding ligands[71] attached to the hydrogel matrix and therapeutic proteins. However, hydrogel-based approaches inherently involve relatively large amounts of carrier material compared to the entrapped protein therapeutic. Toxicity concerns may arise from synthetic crosslinkers or initiators used in polymerization,[40,72] or modification of biological polymers.[73] Biocompatibility issues, such as the foreign body response, may be present at the interface between tissue and materials.[41] Thus, a strategy that uses no or a minimal amount of carrier material is ideal, to eliminate these challenges. Herein, we demonstrate that the concept of "carrier-free" can be realized by adopting a different physical principle, protein self-assembly.

Self-assembly has been exploited as a useful tool to fabricate ordered structures from peptides[2] or proteins.[35] While much effort has been focused on fabrication of self-assembled matrices,[60,74-77] recent studies reported that protein properties, including binding avidity,[78] bioactivity,[52] and stability,[79] are modulated by protein self-assembly. In

---

[1] Reproduced with permission from Park, W. M. and Champion, J. A. *Angew. Chem. Int. Ed.* **2013**, 52, 8098–8101. Copyright 2013 Wiley-VCH Verlag GmbH & Co. KGaA, Weinheim.

this study, we describe a self-assembly system in which proteins self-control their molecular transport in a model extracellular matrix (ECM). Engineered protein building blocks spontaneously self-assemble into particles in the ECM, become trapped, and dissociate to be released at a controlled rate. This protein self-assembly is mediated by temperature-responsive coacervation and dissociation, and by specific binding of high-affinity protein motifs under physiological conditions. Since the ECM selectively regulates microscopic motion of objects depending on their size,[80] the diffusion of protein building blocks is modulated as they form particles under non-equilibrium conditions.

3.2 Experimental Details

3.2.1 Materials

Matrigel^{TM} was purchased from BD Bioscience. PBS (1X, pH 7.4) containing NaCl (137 mM), KCl (2.7 mM), Na_2HPO_4 (10 mM), KH_2PO_4 (1.8 mM) was prepared in the lab.

3.2.2 Characterization of Inverse Phase Transition

Aqueous solutions of Z_R–ELP at various concentrations (1, 2, 4, 8, 16, 32 μM) were prepared in PBS (pH 7.4). The OD of the samples at 350 nm was obtained using a UV/vis spectrophotometer (Beckman Coulter) while the temperature increased at a rate of 1 °C/min. The transition temperature (T_t), at which *dOD/dT* is maximized, was estimated from the turbidity profiles.

Kinetics of the inverse phase transition was also analyzed by measuring the turbidity profile over time. Three concentrations, at which the transition occurs with a temperature elevation from 25 °C to 37 °C, were chosen, and OD at 350 nm was recorded for 15 min. A mathematical model,[81] which has been used for coacervation of

tropoelastin, was used to estimate the rate constant for coacervation (k_c) from the turbidity profiles:

$$OD = -ae^{-k_c t} + be^{-k_m t} + c \quad (3.1)$$

where OD is a function of the concentration proportionality factors (*a, b*), the baseline (*c*), and the rate constant for maturation (k_m). The turbidity profiles at three different concentrations of Z_R–ELP (4, 8, 16 μM) were fitted to the mathematical model.

The rate constant for coacervation (k_c) was estimated at various temperatures (24, 28, 31, 34, 36, 40 °C) and the calculated values for $ln(k_c)$ were plotted as a function of *1/T*. The Arrhenius model was used to calculate activation energy (E_a).

3.2.3 Estimation of Binding Kinetics

An aqueous solution of Z_R–ELP (8 μM in PBS) was incubated at 37 °C for 20 min. The solution became turbid, and 2 μL of the sample was placed on the pre-warmed glass substrate in a temperature controlled incubation chamber at 37 °C. After addition of mCherry–Z_E at different concentrations (0.04, 0.2, 1 μM), the coacervated Z_R–ELP particles were monitored for 2 min using a fluorescence microscope (Axio Observer.Z1, Carl Zeiss) with a 100X objective (excitation: 565/30 nm, emission: 620/60 nm). The fluorescence intensity profiles were quantified as a function of incubation time, and fitted to a bimolecular binding model[82] (Equation 3.2) to estimate the association rate constant k_{on}:

$$I(t) = I_{\max} \frac{k_{on}C_0}{k_{on}C_0 + k_{off}} \left\{1 - e^{-\left(k_{on}C_0 + k_{off}\right)t}\right\} \quad (3.2)$$

where *I(t)* is the fluorescence intensity, I_{max} is the maximum intensity at saturation, C_0 is the initial concentration of mCherry–Z_E, and k_{on} and k_{off} are the rate constants for association and dissociation, respectively.

3.2.4 Preparation of Matrigel Film and Analysis of Self-Assembly

Matrigel™ was cast as a thin film (5 mm × 5 mm × 0.5 mm) by loading the solution into a mold of two polycarbonate plates. Matrigel solution (15 μL) was pre-warmed at 37 °C for 5 min, loaded in the mold, and warmed at 37 °C for 5 min. In order to prevent drying at the interface, the Matrigel film was further allowed to gelate while covered with pre-warmed PBS for 10 min. The top plate was removed, and 5 μL of Z_R–ELP (8 μM) solution was placed as a thin layer on the top of the Matrigel film. After incubation for 20 min, a solution of mCherry–Z_E was added at a concentration of 1 μM for an incubation of 10 min. The Matrigel film was then washed with pre-warmed PBS for 1 min before imaging. The resulting self-assembled particles in Matrigel were imaged using a fluorescence microscope with a 100X objective. While imaging, the Matrigel film samples were placed in an incubation chamber that maintained temperature at 37 °C. The images of individual particles at different depths were also taken from the Matrigel films using a 100X objective in order to demonstrate inhomogeneity of particle density along the depth. The changes in particle size and fluorescence intensity over time were also characterized by imaging samples in 100 μL of PBS at 37 °C for 0.5, 12, and 24 hours. We validated the method of particle sizing from micrographs by comparing size distributions of particles in PBS obtained with dynamic light scattering (DLS). In a control experiment, formation of particles was investigated when Z_R-ELP and Matrigel solution were pre-mixed at 4 °C, warmed up to 37 °C, and followed by addition of mCherry–Z_E to the formed Matrigel matrix. For scanning electron microscope (SEM) imaging, the samples were fixed with glutaraldehyde (1.0 %) for 2 hours. After washing with deionized water for 30 min, the fixed samples were freeze-dried. The samples were sputter-coated with gold, and imaged with Zeiss Ultra60 FE-SEM at 5 kV. A sample of Matrigel treated with only PBS was also imaged as a control.

For the study on the particle layer formation, the narrow side of Matrigel film between polycarbonate plates was exposed to solutions of Z_R–ELP (4, 8, 16 μM) and

mCherry–Z_E (1 μM) in series as described above. The interface region between solution and Matrigel phase was imaged, and the averaged intensity profiles of the fluorescence layer, where the self-assembled particles formed, were quantified from the images obtained using a 10X objective.

3.2.5 Determination of Diffusivities

Diffusivity of mCherry–Z_E was determined by obtaining fluorescence intensity profiles in Matrigel. A solution of mCherry–Z_E (1 μM) was placed at the narrow side of a thin Matrigel film (5 mm × 5 mm × 0.5 mm), and the fluorescence intensity profiles were obtained as a function of time. The intensities at different time and positions were fitted to a Fickian diffusion model (Equation 3.3):

$$\frac{\partial C}{\partial t} = D\frac{\partial^2 C}{\partial x^2} \tag{3.3}$$

$$C = 0 \quad \text{for} \quad 0 < x < l, \quad t = 0 \tag{3.4a}$$

$$C = C_1(t) \quad \text{for} \quad x = 0, \quad t > 0 \tag{3.4b}$$

$$C = C_2(t) \quad \text{for} \quad x = l, \quad t > 0 \tag{3.4c}$$

where C is the concentration of mCherry–Z_E, which is proportional to fluorescence intensity, and D is the diffusivity. The initial and boundary conditions are provided in Equation 3.4. The interface between the solution and Matrigel is defined as the coordinate where $x = 0$, and l is the length of the Matrigel film. Since the length, l, was long enough so that mCherry–Z_E molecules could not reach to the end, $C_2(t)$ remained zero during the experiment. From the boundary conditions, an analytical solution is provided in the form of complementary error function:[83]

$$\frac{C(x,t)}{C_1} = erfc\left(\frac{x}{2\sqrt{Dt}}\right) \tag{3.5}$$

The average fluorescence profiles were fitted to determine the diffusivity of mCherry–Z_E using least square method.

The diffusivity of the self-assembled mCherry–Z_E/Z_R–ELP particles was determined either in Matrigel or solution phase by tracking trajectories of particles' positions. The particles were prepared in Matrigel or in PBS as described in the previous section, and fluorescence and differential interference contrast (DIC) images were obtained using a microscope (100X). Imaging was performed for 6 s at a rate of 11.3 frames/s, and the time-dependent positions were acquired by tracking the particles in the images using AxioVision particle tracking software. The mean-square displacement (MSD) was calculated from the pseudo two-dimensional trajectory of the particles. The mean-square displacement, $\langle \Delta r^2(\tau) \rangle$, is:

$$\left\langle \Delta r^2(\tau) \right\rangle = \frac{1}{N} \sum_{i=0}^{N} \left[r_i(t+\tau) - r_i(t) \right]^2 \qquad (3.6)$$

where r is a position vector for a particle at time t, and τ is lag time. Diffusivity follows the relation MSD(τ) = 4Dτ for the pseudo two-dimensional motion of particles in Matrigel.[84] Thus, we could calculate the diffusivity for the particles from the slopes in the plot of MSD vs. lag time (τ).

3.2.6 Circular Dichroism Spectroscopy

The circular dichroism (CD) spectra for proteins at different states of self-assembly in solution phase (PBS, pH 7.4) were recorded on a Jasco J-810 spectrometer. Z_R–ELP and self-assembled mCherry–Z_E/Z_R–ELP particles were prepared in PBS (pH 7.4). The measurements were performed in a 0.5-cm-length cuvette, and the average spectra of five measurements were obtained from a wavelength range of 200 – 300 nm with 1 nm increments. The unit for mean residue ellipticity was converted with respect to total protein concentration and average number of amino acid residues. Estimation of

secondary structure content was performed with CDSSTR program provided in CDPro software package.

3.2.7 Estimation of Protein Retention in the ECM

Protein retention in the ECM was estimated by quantifying release of the model therapeutic protein, mCherry–Z_E, from Matrigel. A thin Matrigel film (30 μL, 1.5 mm thick) was cast on the bottom of cylindrical tube, where mCherry–Z_E and Z_R–ELP were assembled as particles at the bottom surface. The film was covered with 150 μL of pre-warmed PBS (pH 7.4), and incubated at 37°C. The release buffer solution was sampled at 1, 2, 4, 8, 16, 24, 48, 72, 96 hours and replaced with fresh buffer solution. The concentration of mCherry in the samples was quantified by measuring fluorescence intensity (excitation: 585/9.0 nm, emission: 610/13.5 nm) using a microplate reader. The intensity of each sample was converted to concentration by a calibration curve, and the remaining amount of mCherry in the Matrigel was calculated. The experiment was performed in triplicate, and the control experiment was conducted with same amount of mCherry–Z_E without Z_R–ELP.

3.3 Modeling Details

Formation of particles in the ECM follows a reaction-diffusion model, which is based on gel-phase diffusion of dispersed monomeric Z_R–ELP, its coacervation, diffusion of mCherry–Z_E, and its binding to the Z_R-ELP coacervates (Equation 3.7).

$$\frac{\partial C_e}{\partial t} = D_e \frac{\partial^2 C_e}{\partial x^2} + R_e \tag{3.7a}$$

$$\frac{\partial C_c}{\partial t} = D_c \frac{\partial^2 C_p}{\partial x^2} + R_c \tag{3.7b}$$

$$\frac{\partial C_m}{\partial t} = D_m \frac{\partial^2 C_m}{\partial x^2} + R_m \tag{3.7c}$$

$$\frac{\partial C_p}{\partial t} = D_p \frac{\partial^2 C_p}{\partial x^2} + R_p \tag{3.7d}$$

where concentration, C_i, diffusivity, D_i, and reaction terms, R_i, were included in the model. The subscript *i* denotes the component in the self-assembly system (*e*: monomeric dispersed Z_R–ELP, *c*: coacervates of Z_R–ELP, *m*: monomeric dispersed mCherry–Z_E, *p*: the self-assembled mCherry–Z_E/Z_R–ELP particles). Since the determined diffusivity of mCherry–Z_E was in agreement with an empirical correlation for diffusivity as a function of hydrodynamic radius of macromolecules,[83] the diffusivity of monomeric Z_R–ELP (hydrodynamic diameter, $d_H \approx 4.7$ nm) was calculated to be 96.1 $\mu m^2/s$ from the correlation. As the coacervation kinetics was estimated to be a first order reaction, the reaction terms for coacervation were expressed as $R_c = -R_e = k_c C_e$. The affinity binding of mCherry–Z_E was expressed as $R_p = -R_m = k_{on} C_m C_c - k_{off} C_p$ where k_{on} and k_{off} are the association and dissociation rate constants, respectively. Also, coacervation of Z_R–ELP was modeled to occur only above the minimal concentration of Z_R–ELP at 37 °C (~ 1.9 μM). The initial and boundary conditions are:

1. The first step (coacervation)

$C_e = C_{e,b}$ for $x = 0$, $t = 0$ (3.8a)

$C_e = 0$ for $0 < x \leq l$, $t = 0$ (3.8b)

$C_c = 0$ for $0 \leq x \leq l$, $t = 0$ (3.8c)

$$D_e^l \frac{\partial C_e}{\partial x}\bigg|_{x=-0} = D_e \frac{\partial C_e}{\partial x}\bigg|_{x=+0} \quad \text{for} \quad x = 0, \quad t > 0 \tag{3.8d}$$

$$D_c^l \frac{\partial C_c}{\partial x}\bigg|_{x=-0} = D_c \frac{\partial C_c}{\partial x}\bigg|_{x=+0} \quad \text{for} \quad x = 0, \quad t > 0 \tag{3.8e}$$

$$\frac{\partial C_e}{\partial x} = \frac{\partial C_c}{\partial x} = 0 \quad \text{for} \quad x = l, \quad t > 0 \tag{3.8f}$$

2. *The second step (affinity-binding)*

$C_e = C_{e0}(x)$ for $0 \le x \le l$, $t = 0$ (3.9a)

$C_c = C_{c0}(x)$ for $0 \le x \le l$, $t = 0$ (3.9b)

$C_m = C_{m,b}$ for $x = 0$, $t = 0$ (3.9c)

$C_m = 0$ for $0 < x \le l$, $t = 0$ (3.9d)

$C_p = 0$ for $0 \le x \le l$, $t = 0$ (3.9e)

$$D_e^l \left.\frac{\partial C_e}{\partial x}\right|_{x=-0} = D_e \left.\frac{\partial C_e}{\partial x}\right|_{x=+0} \quad \text{for } x = 0, \quad t > 0 \quad (3.9f)$$

$$D_c^l \left.\frac{\partial C_c}{\partial x}\right|_{x=-0} = D_c \left.\frac{\partial C_c}{\partial x}\right|_{x=+0} \quad \text{for } x = 0, \quad t > 0 \quad (3.9g)$$

$$D_m^l \left.\frac{\partial C_m}{\partial x}\right|_{x=-0} = D_m \left.\frac{\partial C_m}{\partial x}\right|_{x=+0} \quad \text{for } x = 0, \quad t > 0 \quad (3.9h)$$

$$D_p^l \left.\frac{\partial C_p}{\partial x}\right|_{x=-0} = D_p \left.\frac{\partial C_p}{\partial x}\right|_{x=+0} \quad \text{for } x = 0, \quad t > 0 \quad (3.9i)$$

$$\frac{\partial C_e}{\partial x} = \frac{\partial C_c}{\partial x} = \frac{\partial C_m}{\partial x} = \frac{\partial C_p}{\partial x} = 0 \quad \text{for } x = l, \quad t > 0 \quad (3.9j)$$

where the concentrations in the bulk solution phase are indicated as $C_{i,b}$. The diffusivities D_i^l in the solution phase were estimated from the experiments or the Stokes-Einstein equation.[85] The boundary conditions account for our experimental observations that the diffusive fluxes from the solution phase equal the fluxes that enter the Matrigel phase and that the partition coefficient is close to unity, as described above. $C_{e,b}$ was assumed to follow coacervation kinetics ($C_{e,b} = C_{e,b}^0 \exp(-k_c t)$) as coacervation simultaneously occurs in both solution and Matrigel phases. In order to reflect the discrepancy during initial kinetics, coacervation was implemented to have a concentration dependent lag time ($\tau_c = -0.7213 \ln C_e + 2$, correlated from the coacervation kinetics). For three values of the initial concentration of Z_R–ELP ($C_{e,b}^0$) in the solution phase (4, 8, 16 μM), the distribution of self-assembled particles in Matrigel was predicted using Matlab. From the first step

(coacervation), the concentration profiles of monomeric ($C_{e0}(x)$) and coacervates of Z_R–ELP ($C_{c0}(x)$) were obtained, and used as initial conditions for the second step (affinity-binding).

3.4 Results

3.4.1 Two-Step Protein Self-Assembly in the ECM

The system is built from two different diblock fusion proteins. The first component (mCherry–Z_E) is constructed from a globular fluorescent protein mCherry,[61] which serves as a model for a therapeutic protein, and a glutamic acid-rich leucine zipper (Z_E). An arginine-rich leucine zipper (Z_R) and elastin-like polypeptide (ELP) comprise the second component (Z_R–ELP)[51] (Figure 3.1A). ELP is composed of a pentapeptide repeat derived from tropoelastin, which undergoes a temperature-responsive inverse phase transition from soluble to coacervate phase.[54] The leucine zipper motifs Z_E and Z_R form heterodimeric α-helical coiled-coils with a dissociation constant, $K_d \approx 10^{-15}$ M.[49] The fusion proteins were produced separately via bacterial protein synthesis and purified.[51] In aqueous solution, Z_R–ELP showed the expected inverse phase transition as characterized by an increase in light scattering upon temperature elevation (Figure 3.1B and Figure 3.2). The transition temperature is dependent on the concentration of Z_R–ELP in PBS (pH 7.4), and Z_R–ELP at 1.9 to 24 μM formed coacervates when the solution was heated from 25 to 37 °C. Subsequent addition of mCherry–Z_E resulted in rapid binding to the Z_R-ELP coacervates within a minute (Figure 3.3), showing an association rate constant of $k_{on} \approx 1.5 \times 10^5$ $M^{-1}s^{-1}$ (Figure 3.1C). As elucidated by kinetic analysis (Figure 3.2) and circular dichroism (Figure 3.4 and Table 3.1), Z_R/Z_R coiled-coils of Z_R–ELP simultaneously unfold during the phase transition followed by subsequent refolding of Z_R/Z_E heterodimer coiled-coils upon binding of mCherry–Z_E.

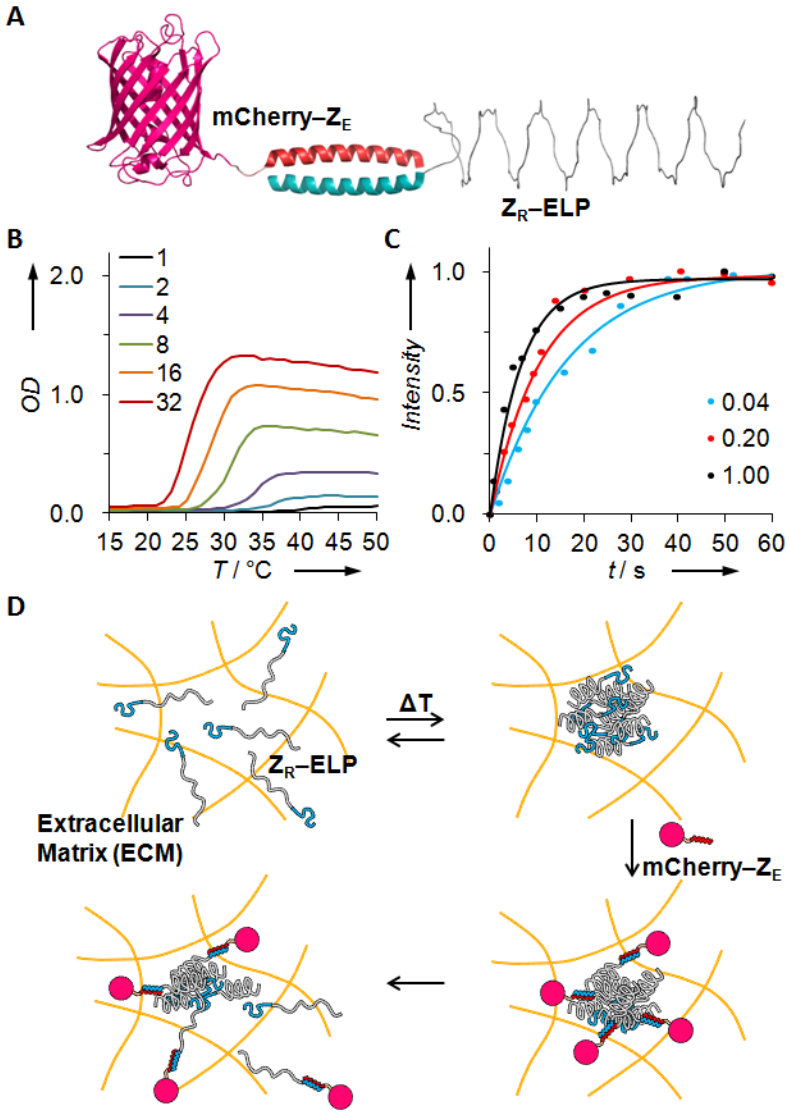

Figure 3.1 Protein building blocks and their self-assembly in solution phase and in ECM. (A) The recombinant engineered protein building blocks, mCherry–Z_E and Z_R–ELP, are produced separately, but self-assemble via formation of coiled-coils (PDB ID: 2H5Q for mCherry). (B) The inverse phase transition of Z_R–ELP in aqueous solution: Temperature vs. optical density (OD at λ = 350 nm) measured at different concentrations of Z_R–ELP (1, 2, 4, 8, 16, 32 μM). (C) The binding kinetics estimated by fluorescence intensity changes of the Z_R–ELP coacervates upon incubation with mCherry–Z_E (0.04, 0.2, 1 μM). The measured intensities (dots) were fitted to a bimolecular binding model (lines). (D) Schematic illustration of the *in situ* self-assembly of mCherry–Z_E and Z_R–ELP in ECM.

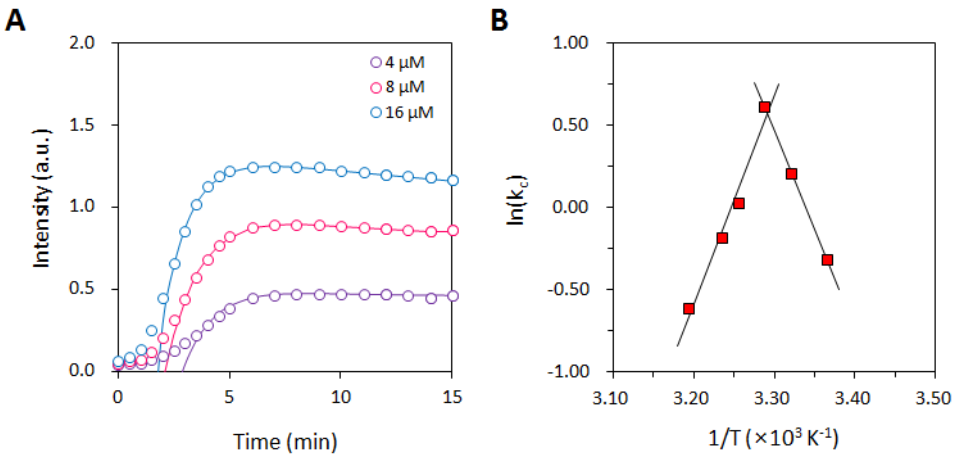

Figure 3.2 Kinetics of the inverse phase transition of Z_R–ELP. (A) The turbidity profile of Z_R–ELP (4, 8, 16 μM) in PBS (pH 7.4) as temperature increases from 25 °C to 37 °C: the turbidity profile was measured at 350 nm (open circles) and fitted to the mathematical model (Equation 3.1) (solid lines) to estimate k_c. As a result, k_c was estimated to be 0.70 ± 0.12 min^{-1} at 37 °C. (B) The plot of *ln* (k_c) vs. *1/T* ($\times 10^3$ K^{-1}): activation energy for coacervation was calculated from the fitted linear slopes (solid lines). The slope of *ln* (k_c) vs. 1/T showed two different values depending on temperature. In the lower temperature region (24 to 30 °C), E_a was calculated as 23.7 kcal mol^{-1}, whereas a negative value (–25.2 kcal mol^{-1}) was obtained for the higher temperature region (30 to 40 °C). The negative E_a indicates that coacervation of Z_R–ELP does not have an energy barrier and k_c decreases with increasing temperature. We hypothesize that Z_R/Z_R homodimers start to unfold and deform above 30 °C so that the reaction rate for coacervation becomes slower as temperature increases.

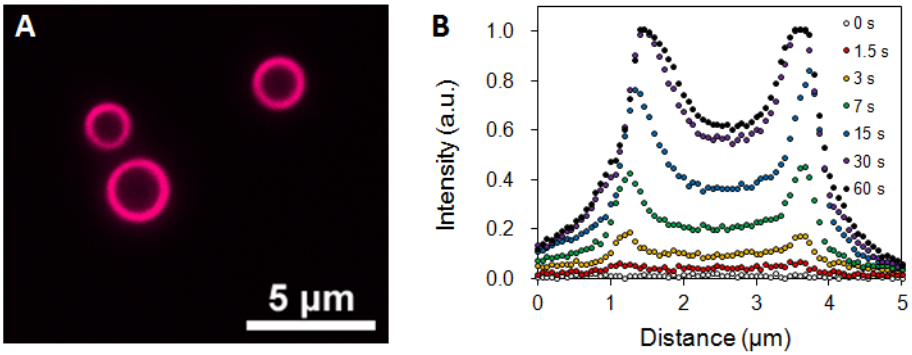

Figure 3.3 Affinity binding of mCherry–Z_E to Z_R–ELP coacervates. (A) Fluorescence micrographs of mCherry–Z_E/Z_R–ELP particles in solution phase. (B) The changes in the particle fluorescence intensity profile during 1 min of incubation.

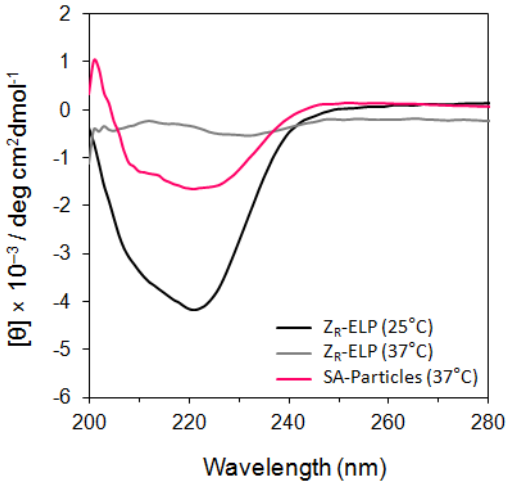

Figure 3.4 The changes in secondary structure of the protein building blocks. The CD spectra of dispersed monomeric (25 °C, black) and coacervated Z_R–ELP (37 °C, gray), and the self-assembled mCherry–Z_E/Z_R–ELP particles (37 °C, pink). 8 μM of Z_R–ELP was prepared in PBS (pH 7.4), and it was mixed with 1 μM of mCherry–Z_E for analysis.

Table 3.1 The secondary structure of the protein building blocks analyzed from the CD spectra (Figure 3.4). Comparison of calculated and experimental results is provided in normalized root-mean-square deviations (NRMSD).

Samples	Residues in leucine zippers (Z_R / Z_E) (%)	α-helix (%)	β-strand (%)	Turn and unordered (%)	NRMSD
Z_R-ELP (25°C)	29.4 / 0.0	35.1	13.5	52.2	0.036
Z_R-ELP (37°C)	29.4 / 0.0	2.0	38.5	57.9	0.322
SA mCherry-Z_E/Z_R-ELP Particles (37°C)	27.8 / 1.6	7.0	36.2	56.0	0.108

Next, we performed the two-step self-assembly of the fusion protein components in the ECM as illustrated in Figure 3.1D, using a reconstituted ECM hydrogel (Matrigel^{TM}) as a model for the native ECM. The inverse phase transition of soluble Z_R–ELP (25°C) that permeated through the ECM hydrogel (37°C) resulted in the *in situ* formation of coacervated particles. In the second step, mCherry–Z_E was added and bound to the particles via the high-affinity interaction between the leucine zipper motifs. As a result, we observed formation of fluorescent particulates of mCherry–Z_E/Z_R–ELP in the ECM hydrogel (Figure 3.5A,B and Figure 3.6A) with diameters ranging from 330 nm to 1.6 μm. Interestingly, we found particulates with irregular shapes that seemed to be from incomplete coalescence of coacervated Z_R–ELP nanoparticles (Figure 3.5C). In aqueous solution, Z_R–ELP grows into microspheres with smooth surfaces by the coacervation-coalescence process, and the binding of mCherry–Z_E does not influence the surface morphology (Figure 3.3). Therefore, the observation of non-spherical particles in the ECM hydrogel indicates that the coalescence of the coacervates is limited by the presence of the matrix. When Z_R–ELP was premixed with ECM solution at 4 °C and warmed up, it formed large coalesced particles (~ 10 μm) with irregular shapes due to initial absence of

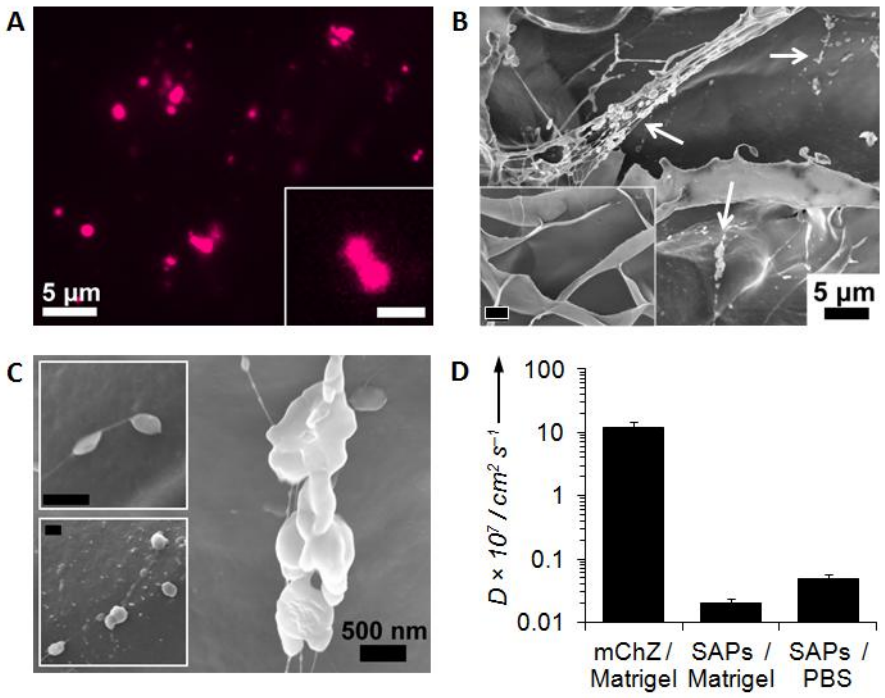

Figure 3.5 The mCherry–Z_E/Z_R–ELP particles that self-assembled in ECM hydrogel. (A) Fluorescence micrographs of particles formed in Matrigel (inset scale bar 1 µm) (B, C) Scanning electron micrographs of the particles (arrowed): the particle-embedded Matrigel was fixed with glutaraldehyde for 2 hr, and freeze-dried. For comparison, the Matrigel treated with only PBS was imaged (inset in (B), scale bar 5 µm, insets in (C), scale bars 500 nm). (D) Diffusivity (*D*) of mCherry–Z_E (mChZ) and self-assembled particles (SAPs) in Matrigel or PBS.

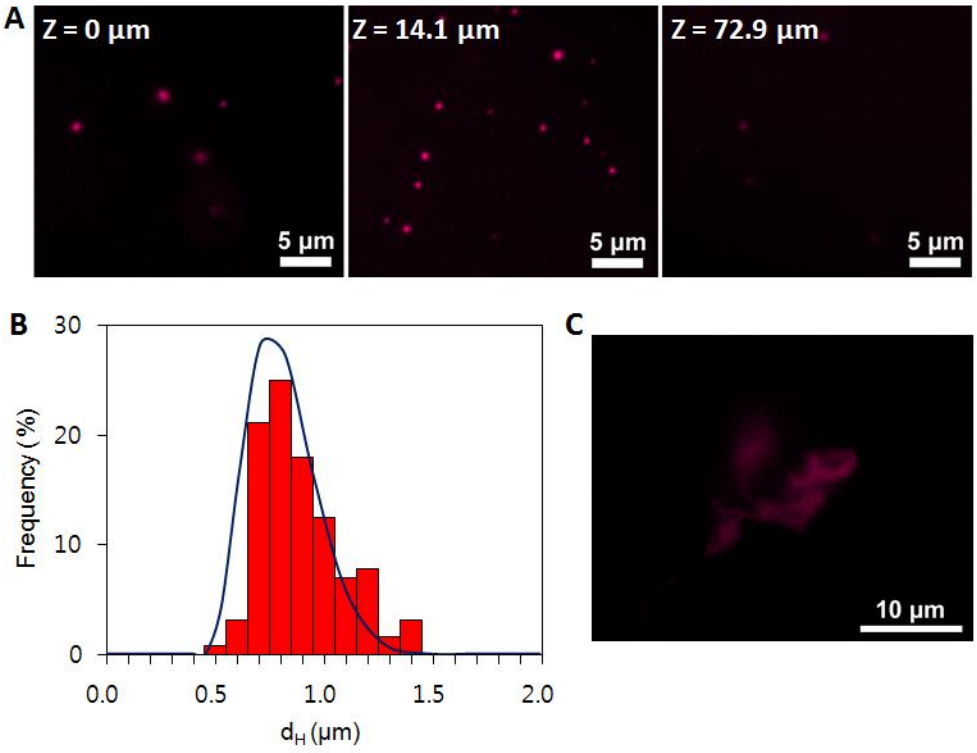

Figure 3.6 Characterization of mCherry–Z_E/Z_R–ELP particles (A) Particles at different depths: Z = 0 µm (near the interface), 14.1 µm, and 72.9 µm. (B) Comparison of size distributions of the particles in PBS obtained from micrographs (bars) and DLS (line). (C) Morphology of mCherry–Z_E/Z_R–ELP particles from premixing of Z_R–ELP and Matrigel solution at 4°C: The mixed solution was warmed up to 37°C and mCherry–Z_E was added afterwards.

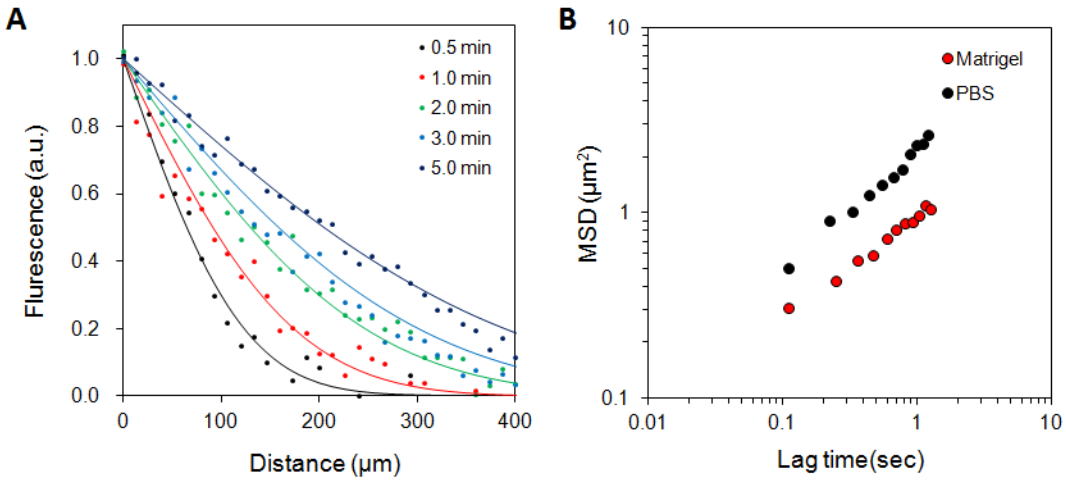

Figure 3.7 Determination of diffusivities for mCherry–Z_E and self-assembled mCherry–Z_E/Z_R–ELP particles. (A) The fluorescence intensity gradient of mCherry–Z_E in Matrigel (points) was fitted to a Fickian diffusion model (solid line) to estimate the diffusivity, D. (B) MSD was plotted as a function of lag time for the self-assembled particles in Matrigel (red) and in PBS (black).

the matrix (Figure 3.6C). Hindered by the matrix, the self-assembled mCherry–Z_E/Z_R–ELP particles formed in the ECM hydrogel showed reduced diffusivity. Estimated from particle trajectories, the diffusivity of mCherry–Z_E/Z_R–ELP particles was 2.5 fold lower in the ECM hydrogel than in aqueous solution, and 500 fold lower than that of monomeric mCherry–Z_E in the ECM hydrogel (Figure 3.5D and Figure 3.7). Indeed, the *in situ* self-assembly resulted in entrapment of the model protein, mCherry, in the ECM hydrogel by the self-assembly process. The low diffusivity of the self-assembled mCherry–Z_E/Z_R–ELP particles is based on the hydrodynamic and steric interactions of the particles with the ECM,[86] and their insignificant electrostatic interactions with the matrix (zeta potential, $\zeta \approx -2.6$ mV)[84] allow the protein particles to be locally dynamic at a reduced mobility rather than immobilized on the matrix.

3.4.2 Self-assembled Particle Layer

Estimated using a mathematical model,[81] the coacervation by inverse phase transition of Z_R–ELP has a rate constant, $k_c \approx 0.7$ min^{-1} (Figure 3.2A). The characteristic time for coacervation, τ_c ($\approx 1/k_c$) is ≈ 90 s. The characteristic length for the system L ($\approx (D/k_c)^{-0.5}$) is approximated as 100 μm if τ_c is on the same order with the characteristic time for the diffusion of dispersed Z_R–ELP, τ_d ($\approx L^2/D$). Thus, the scaling analysis accounts for the simultaneous diffusion and temperature-responsive coacervation of Z_R-ELP in the ECM. This is a reaction-diffusion system, which allows formation of self-assembled particles in a layer of thickness, L. The coacervated Z_R–ELP particles accumulated in the layer and mCherry–Z_E rapidly bound to the particles during the second step of self-assembly. We observed formation of a fluorescent layer near the ECM hydrogel-solution interface in Figure 3.8, and the initial concentration of Z_R–ELP controlled the amount of particles in the layer, as indicated in the fluorescence images (Figure 3.8B). The diffusion, coacervation, and affinity-binding of the protein building blocks in the ECM hydrogel were modeled by a one dimensional reaction-diffusion equation (Equation 3.10),

$$\frac{\partial C_i}{\partial t} = D_i \frac{\partial^2 C_i}{\partial x^2} + R_i \qquad (3.10)$$

where x is distance from the solution-hydrogel interface, C_i is concentration, D_i is diffusivity, and R_i is the reaction term for a protein or particle component i. In our model, coacervation of Z_R–ELP from soluble proteins to particles was included in the reaction term, and the diffusivity of the particles was assumed to be constant since their size does not change significantly once they form. The modeling results were consistent with the experimental results (Figure 3.8C), supporting the theoretical argument of *in situ* self-assembly in the ECM hydrogel. Although the model does not duplicate the experimental mCherry fluorescence profile exactly, it demonstrates the ability to control the amount of mCherry–Z_E in the ECM hydrogel.

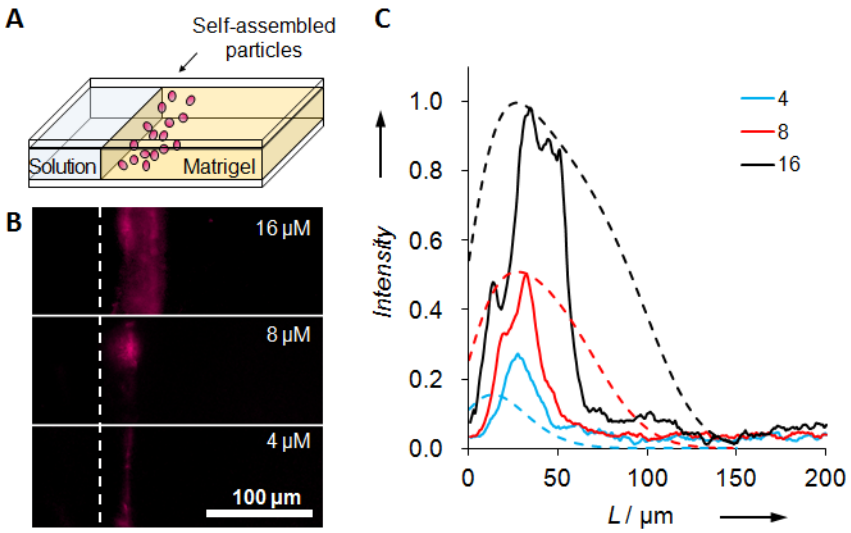

Figure 3.8 The layer of self-assembled particles in ECM hydrogel. (A) Schematic illustration of the model system. (B) Fluorescence micrographs of the layer where particles are located. (C) The corresponding profiles of fluorescence intensity at distance (L) from Matrigel-solution interface: the experimental results of averaged profiles (solid) were compared with the profiles from modelling (dashed). The initial concentration of Z_R–ELP was varied (4, 8, 16 μM), and the computational modelling was performed based on reaction-diffusion equations.

3.4.3 Dissociation of Self-Assembled Particles

The self-assembled mCherry–Z_E/Z_R–ELP particles in the ECM hydrogel are metastable, and Z_R–ELP dissociates from the particles when the local concentration of Z_R–ELP drops below the minimum phase transition concentration (~ 1.9 μM at 37°C). As a result, the *in situ* self-assembled particles shrank over time in the ECM hydrogel. The average diameter (*d*) decreased from 828 ± 354 nm to 542 ± 158 nm during the first 24 hours (Figure 3.9A). The size distribution of the particles also narrowed, indicating that the particles larger than 1 μm shrank more rapidly. The surface erosion from larger

particles (d > ~ 1 μm) is faster than smaller particles due to the ouzo effect that smaller particles are thermodynamically favored when the concentration of Z_R–ELP decreases.[87] Concurrently, the fluorescence intensity of the particles was reduced by half after 12 hours of dissociation proceeded, and there was further reduction in fluorescence to 37.8% of the initial value after 24 hours (Figure 3.9B). The initial drop in intensity is attributed to the rapid shrinking of the large particles (d > 1 μm), when the rate of decrease in intensity is proportional to the shrinking rate of the particles. While the average size of particles gradually decreased, the approximate concentration of mCherry on the particles remains approximately constant after an initial decrease of 40.6% in the first 12 hours (calculated from the fluorescence intensity per unit area of particles). It indicates that dissociation of Z_R–ELP from the particles seems to also induce release of mCherry–Z_E/Z_R–ELP.

As suggested by the dissociation kinetics of particles, self-assembly resulted in an enhanced retention of proteins in the ECM hydrogel (Figure 3.9C). The *in situ* assembled protein building blocks in the ECM hydrogel were exposed to a reservoir of 37 °C PBS to simulate the ECM environment *in vivo* and generate a concentration sink to induce disassembly and diffusion. The overall retention of mCherry–Z_E with Z_R–ELP was enhanced by 100% compared to monomeric mCherry–Z_E, of which less than 30% remained in the ECM hydrogel after 24 hours. Consistent with the observed dissociation kinetics in Figure 3.9B, dissociation of mCherry–Z_E from the self-assembled particles led to an initial clearance of mCherry–Z_E (~ 36 % loss over 12 hours), which was much slower than soluble mCherry–Z_E (~ 58 % loss). Considering the drastic difference in diffusivities of soluble proteins and particles (~ 500 folds), the controlled release of mCherry–Z_E in the ECM hydrogel should have resulted from dissociation of mCherry–Z_E from the particles. Furthermore, when mCherry without the Z_E domain, was added together with Z_R–ELP in the ECM hydrogel, the release profile of mCherry/Z_R–ELP was very close to that of mCherry–Z_E alone. This result indicates that mCherry does not have

specific interactions with Z_R–ELP and that the coacervates do not alter the release without the specific Z_E-Z_R interaction.

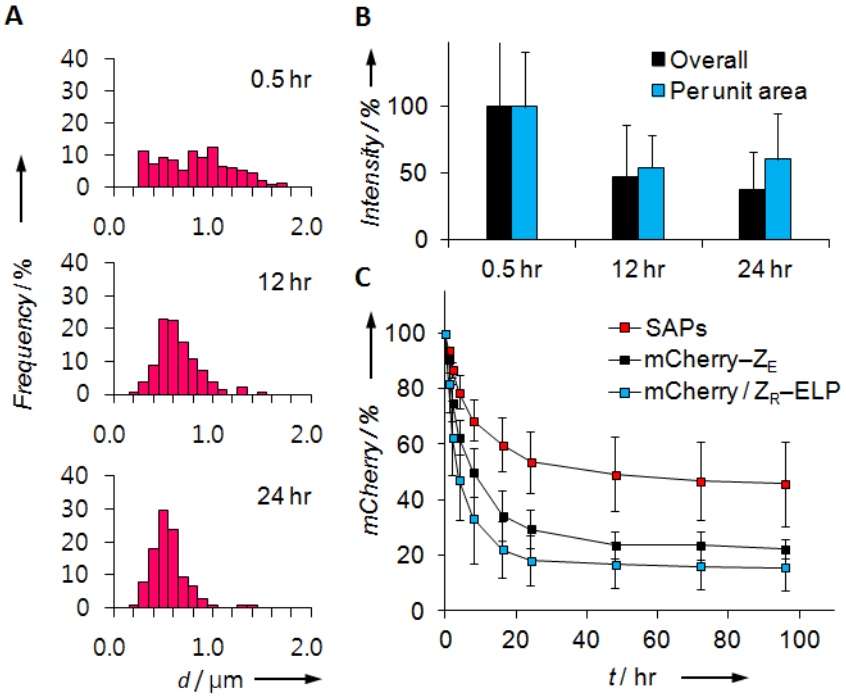

Figure 3.9 Dissociation of mCherry–Z_E/Z_R–ELP particles. (A) Particle size distribution changes with time: the frequency of particles is indicated for corresponding diameter, d. (B) Fluorescence intensity changes upon particle dissociation: the overall average intensity (black) and the intensity per unit area of the particles (blue). (C) The release of mCherry- Z_E imbedded in Matrigel as a soluble protein (black, mCherry–Z_E) or self-assembled particles (red, SAPs), and of mCherry in the presence of Z_R–ELP (blue, mCherry/Z_R–ELP).

3.5 Discussion

Compared to the conventional recombinant conjugation of therapeutic protein directly to ELP, the two-component system based on the leucine zippers (Z_R/Z_E) shows new features in the inverse phase transition behavior of ELP. ELP–peptide or ELP–protein conjugates have been engineered to self-assemble into nanoparticles upon the inverse phase transition,[88-90] which has led to remarkable progress in delivery of chemo-[38,91] and protein therapeutics.[92,93] While ELPs of more than 60 repeats of the pentapeptide exhibit less concentration dependence, Z_R–ELP (25 repeats) undergoes inverse phase transition at relatively low temperatures (40 to 20°C) with a strong concentration dependence (1 to 100 μM). This allows self-assembly and disassembly due to concentration gradients at 37°C. Also, the ratio of functional protein to ELP is very flexible as they can be conjugated at different molar ratios after coacervation.

Our system is widely applicable for local delivery of protein therapeutics to diseased sites, where proteins could be topically applied or injected, and upon contact will warm to body temperature and start the assembly process. We note that this system has several advantages as a new strategy for protein delivery. First, carrier-free delivery based on protein self-assembly does not involve use of excessive synthetic or biological materials with potential biocompatibility or toxicity issues.[40,41,72,73] The self-assembling motifs, ELP and Z_R/Z_E, are derived from extra-[94] and intracellular[49] human proteins, and toxicity potential is decreased.[94,95] Furthermore, ELP has been reported to stimulate granulation in wounds,[39] which could have synergetic effects for protein delivery specifically in wound healing applications. Second, 100% of dosed protein is spatially distributed in the ECM, and the temporal concentration gradient resulted by the dissociation of particles could yield optimal responses in applications with therapeutic proteins.[96]

3.6 Conclusion

In summary, we have described a protein self-assembly system where the protein components self-assemble in the ECM and become entrapped as particles, demonstrating potential as a new type of "carrier-free" protein delivery approach. Our analysis shows spontaneous diffusion-coacervation and high-affinity binding processes that mediate *in situ* formation of self-assembled particles that shrink and release protein in the ECM. Though demonstrated with a model fluorescent protein, this new concept is widely applicable for a variety of protein therapeutics, including growth factors and cytokines.

CHAPTER 4

THERMALLY TRIGGERED SELF-ASSEMBLY OF FOLDED PROTEINS INTO VESICLES[2]

4.1 Introduction

Vesicles are enclosed compartments created by self-assembled membranes of amphiphiles. While biological vesicles made from amphiphilic small molecules, predominantly phospholipids, are abundant in nature, their macromolecular analogues have been developed primarily using synthetic block copolymers.[97] Polymeric vesicles exhibit enhanced stability and mechanical properties,[98] and their permeability,[99] size,[100] and shape[101] can be tuned. Besides synthetic block copolymers, biological copolymers such as polypeptides[102,103] and recombinant proteins[104] have also been developed to self-assemble into vesicles. They are biocompatible and biodegradable and can offer biofunctionality through incorporation of peptide sequences or folded proteins. Self-assembly of folded proteins, in many examples, provides a versatile method to fabricate functional biomaterials for a range of applications.[22,105] However, direct incorporation of folded and biologically relevant moieties into protein amphiphiles can prevent conformational arrangement of chains during vesicle formation, and their molecular weight might be limited. Furthermore, organic solvents, which are typically added to dissolve amphiphilic proteins or polypeptides,[102,104] can hamper biological activity of incorporated folded proteins. For these reasons, vesicles of folded recombinant proteins are underdeveloped.[104] In fact, folded, globular proteins have been incorporated into

[2] Reproduced with permission from Park, W. M. and Champion, J. A. *J. Am. Chem. Soc.* **2014**, 136, 17906–17909. Copyright 2014 American Chemical Society."

vesicles only as hybrid forms of protein-synthetic polymers.[106] Herein, we report self-assembly of vesicles from recombinant protein amphiphiles that contain folded globular proteins. In aqueous solution, formation of hollow vesicles with globular proteins results from temperature-responsive phase transition. Depending on the conditions, vesicles can encapsulate protein coacervates formed simultaneously. In addition, small molecules and nanoparticles can preferentially be encapsulated in the vesicles.

An elastin-like polypeptide (ELP) motif serves as the hydrophobic block. It is a penta-repeat polypeptide derived from tropoelastin that undergoes an inverse phase transition, from soluble to insoluble, in aqueous solution as temperature increases above the transition temperature.[54] It is an attractive process to construct various nanostructures via thermally triggered self-assembly. When combined with hydrophilic domains, amphiphilic diblocks containing ELP motifs have led to formation of spherical[89,90] and cylindrical micelles[88] and vesicles.[107] While random coil peptides were used as hydrophilic blocks in most examples, rigid, rod-shaped leucine zipper coiled coils and globular proteins are used here. Combined with an ELP, the folded proteins are incorporated into self-assembled vesicles as part of the building blocks.

4.2 Experimental Details

4.2.1 Materials

Fluorescent polystyrene nanoparticles (Fluoresbrite® YG Carboxylate Microspheres 0.50 μm) were purchased from Polysciences.

4.2.2 Self-Assembly of Vesicles and Encapsulation

Solutions of the purified recombinant proteins, Z_R−ELP, mCherry−Z_E, and EGFP−Z_E were mixed on ice. The final protein and salt concentration was adjusted by adding deionized water and diluting concentrated buffer (100 mM Na_2HPO_4, 18 mM KH_2PO_4, 27 mM KCl, and 1.37 M NaCl, pH 7.4). The protein mixture solutions were left on ice for 15 min. Next, the solutions were placed at room temperature (25 °C) for 1 hour to form vesicles. Encapsulation was performed following the same procedure as vesicle self-assembly, except that 50 μg/mL of fluorescein or 125 μg/mL of fluorescent polystyrene nanoparticles (1.8 X 10^9 particles/mL) were added to protein mixture solutions on ice before room temperature incubation.

4.2.3 Confocal Microscopy

Confocal micrographs were obtained with a Zeiss LSM 510Vis (Carl Zeiss). A droplet of vesicle samples (5 μL) was placed on a rectangular glass (24 x 60 mm), which was covered with a square cover glass (18 x 18 mm) in the presence of spacers with thickness of 0.15 mm. All vesicle samples were imaged using a 100X oil immersion objective. Laser wavelengths of 488 nm and 543 nm were used with high pass (LP 505) and band pass (BP 565−615) emission filters.

4.2.4 Scanning Electron Microscopy

A cross-section of freeze-dried fractured vesicles was imaged with a Zeiss Ultra60 FE-SEM (Carl Zeiss). A vesicle sample was placed on a glass substrate and fixed with glutaraldehyde (1.0 %) for 1 hour. After washing twice with deionized water, the samples were freeze-dried and fractured. The vesicles were transferred to a carbon tape and sputter-coated with gold before imaging at 5 kV. Non-fractured vesicles were also

imaged as a control. The thickness of vesicle membrane was measured from a close-up image of a fractured vesicle.

4.2.5 Dynamic Light Scattering

Hydrodynamic diameters of vesicles were measured with a Zetasizer Nano ZS (Malvern Instrument). A 4 mW He-Ne laser operating at a wavelength of 633 nm was equipped and operated at a detection angle of 173°. Vesicle solution samples (100 μL) were prepared in a cuvette, and measurements were performed at 25 °C. The raw correlation data were processed to size distribution by using Dispersion Technology Software.

4.2.6 Circular Dichroism Spectroscopy

The CD spectra of protein complexes were recorded on a Jasco J-810 spectropolarimeter (JASCO). Protein solution samples were prepared in PBS (pH 7.4), and measurements were performed in a 0.2-cm-length cuvette. The spectra were obtained in 1 nm increments within a wavelength range of 200 − 300 nm. Mean residue ellipticity was converted from accumulated spectra of five measurements for each sample.

4.2.7 Turbidity Measurement

The turbidity of protein solutions was measured from the optical density of transmitted light at 400 nm, using a microplate reader (Synergy HT Multi-Mode, BioTeck). Absorption by the proteins is negligible at this wavelength. The protein solutions (100 μL) were prepared in a 96-well microplate at 4 °C and placed in the instrument at 25 °C. Then, the changes of turbidity were monitored by recording the optical density of protein solutions every minute for 100 min.

4.3 Results and Discussion

4.3.1 Self-Assembly of Protein Vesicles

In the present study, protein vesicles were created by combinations of three different diblock recombinant proteins: Z_R–ELP, mCherry–Z_E, and EGFP–Z_E (Figure 4.1A). An ELP motif was conjugated with a coiled coil domain (Z_R) as a fusion protein Z_R–ELP.[51] The arginine-rich leucine zipper motif (Z_R) forms coiled coil complexes with its counterpart Z_E.[49] The glutamic acid-rich leucine zipper motif (Z_E) was fused with two different fluorescent proteins, mCherry and EGFP. As illustrated in Figure 4.1B, the leucine zipper coiled coil (Z_E/Z_R) incorporates the globular domains into a "globule-rod–coil" protein complex (mCherry–Z_E/Z_R–ELP or EGFP–Z_E/Z_R–ELP) via their high affinity interaction with extremely low dissociation constant ($K_d \approx 10^{-15}$ M).[49] Because of the weaker affinity between Z_R motifs ($K_d \approx 10^{-7}$ M),[49] Z_R–ELP forms homodimers and was used as a temperature-responsive "rod–coil" protein amphiphile. The "globule-rod–coil" and "rod–coil" protein complex amphiphiles are made first by mixing (Figure 4.1B), where the globular and rod-shaped proteins serve as hydrophilic blocks. Circular dichroism spectroscopy confirms that each protein complex contains the α-helical coiled coil motifs (Figure 4.2).

By incubating the protein mixture at room temperature, ELP separates into a hydrophobic phase and the protein complexes self-assemble into vesicles in aqueous solution (Figure 4.1B). The protein mixture solution, prepared at 4 °C, was placed at room temperature for an hour and became turbid as a result of vesicle formation (Figure 4.3). Figures 4.4A and 4.4B show protein vesicles self-assembled from Z_R-ELP mixed with either mCherry–Z_E or EGFP–Z_E. According to dynamic light scattering (DLS)

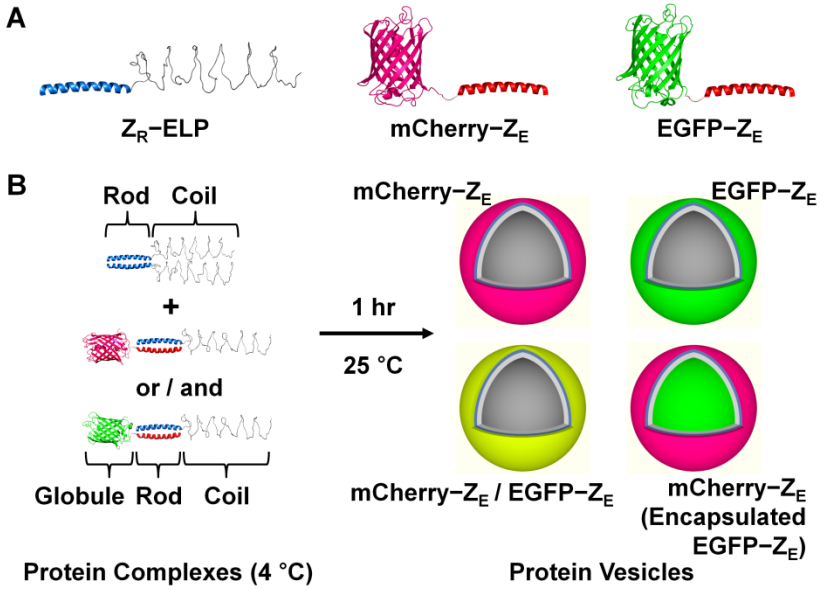

Figure 4.1 Recombinant protein amphiphiles and their self-assembly into vesicles. (A) Recombinant diblock copolypeptides: Z_R–ELP, mCherry–Z_E, and EGFP–Z_E (PDB ID: 2H5Q for mCherry and 1EMK for EGFP). (B) The rod–coil (Z_R-ELP homodimer) and 'globule-rod-coil' (mCherry–Z_E/Z_R–ELP and EGFP–Z_E/Z_R–ELP) protein complexes prepared in solution at 4 °C self-assemble into hollow vesicles employing mCherry, EGFP, or both globular domains. Depending on conditions, EGFP–Z_E can form a coacervate phase encapsulated by mCherry–Z_E vesicles.

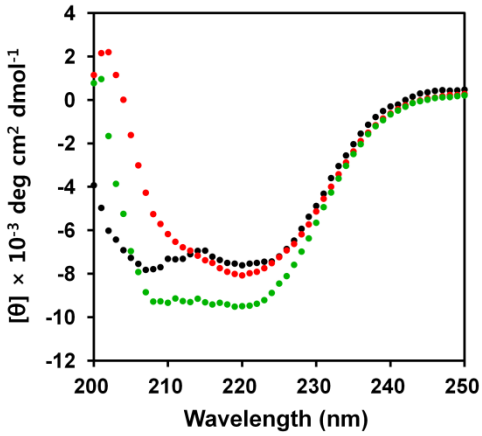

Figure 4.2 CD spectra of protein complexes Z_R−ELP (black), mCherry−Z_E/Z_R−ELP (red), and EGFP−Z_E/Z_R−ELP (green). Mean residue ellipticity was measured from protein solutions containing 5 μM of protein complexes at 4 °C.

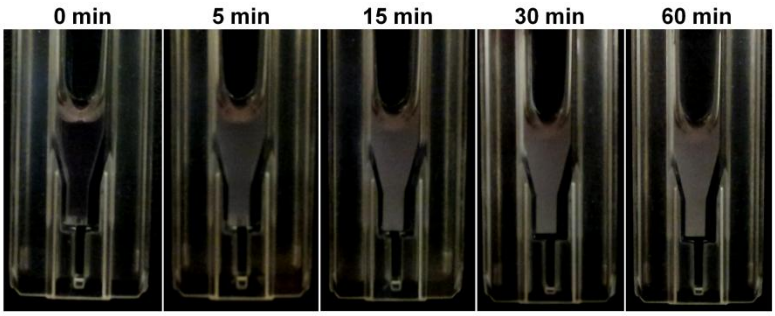

Figure 4.3 Photographs of a protein solution during inverse phase separation. A protein solution (300 μL) containing mCherry−Z_E (1.5 μM) and Z_R−ELP (30 μM) was prepared in a cuvette at 4 °C, and the photographs were taken at 0, 5, 15, 30, 60 min after placing at room temperature (25 °C). The salt concentration was 0.3 M.

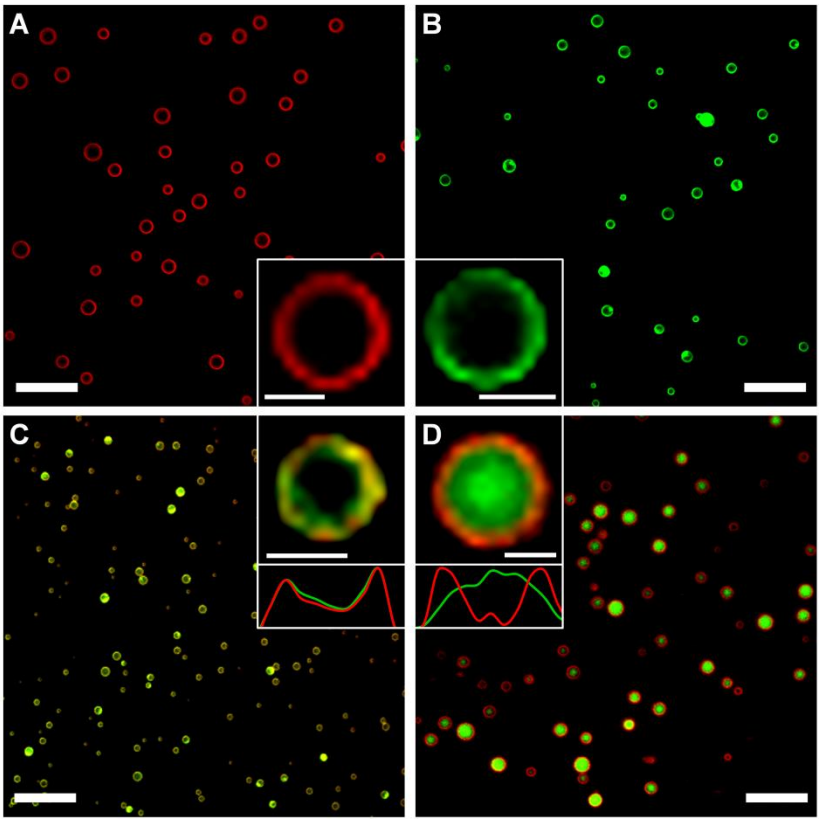

Figure 4.4 Self-assembled protein vesicles. Confocal micrographs of vesicles prepared from solutions containing different concentrations of the recombinant protein components: (A) 1.5 μM of mCherry–Z_E and 30 μM of Z_R–ELP; (B) 0.6 μM of EGFP–Z_E and 30 μM of Z_R–ELP; (C) 0.3 μM of mCherry–Z_E, 0.3 μM of EGFP–Z_E, and 30 μM of Z_R–ELP; (D) 1.5 μM of mCherry–Z_E, 0.6 μM of EGFP–Z_E, and 30 μM of Z_R–ELP. Salt concentrations of the solutions were (A) 0.30 M, (B, C) 0.91 M, and (D) 0.45 M. Fluorescence from the vesicles was visualized using different colors, red (mCherry–Z_E) and green (EGFP–Z_E), which colocalize to yellow in (C). The insets are close-up images and the curves in (C) and (D) are fluorescence intensity profiles corresponding to the inset images. Scales bars are 10 and 1 μm (inset), respectively.

measurements (Figure 4.10A), the average diameters were 1.26 μm and 1.82 μm for vesicles incorporating mCherry and EGFP domains, respectively, with a narrow size distribution (polydispersity index < 0.03). The red and green fluorescence indicates homogenous incorporation of mCherry–Z_E and EGFP–Z_E in each vesicle membrane. Since the inverse phase transition of ELP does not involve use of any organic solvents and thus provides a biocompatible environment, no loss of fluorescence by denaturation of mCherry or EGFP was seen. Upon dilution of the vesicle solution, no significant change in fluorescence intensity was observed (Figure 4.5), indicating that mCherry–Z_E is not exchanged between vesicles and solution due to the extremely low dissociation constant of Z_E and Z_R coiled coils. To confirm that the vesicles are hollow, we imaged cross-sections of fractured, freeze-dried vesicles. Scanning electron microscopy (SEM) images clearly show the empty inner space of a vesicle (Figure 4.6). Thickness of the vesicle membrane, measured from SEM images, was about 20 nm.

We found salt concentration to be a critical factor for vesicle formation. We tested the inverse phase transition of protein mixture solutions at different salt concentrations (0.15 M – 1.21 M) with a fixed concentration of Z_R–ELP (30 μM). Vesicle formation was only observed above critical values of salt concentration, which are estimated to be approximately 0.30 and 0.91 M for vesicles incorporating mCherry–Z_E and EGFP–Z_E, respectively. Below these concentrations, we only observed formation of coacervate particles, droplets of protein-rich phases (Figure 4.7). They are the typical result of ELP inverse phase transition.[108,109]

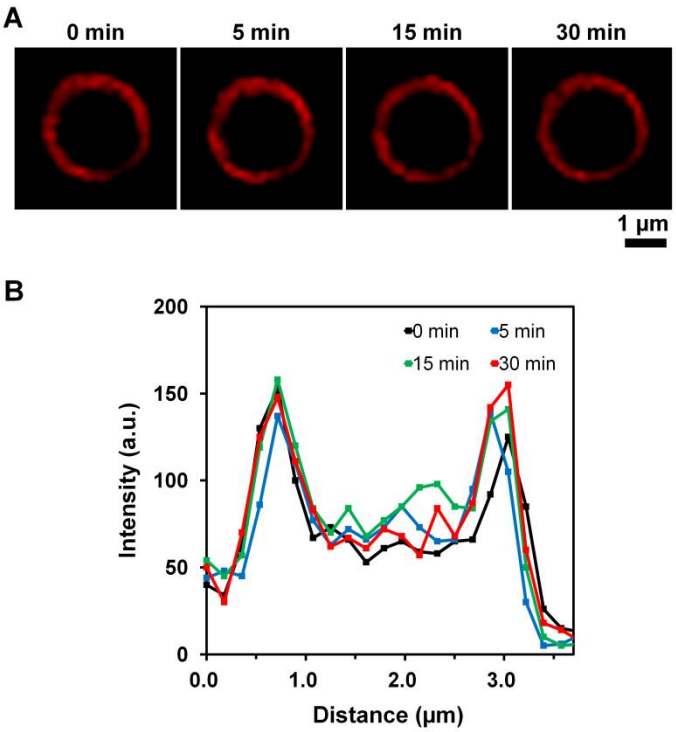

Figure 4.5 Fluorescence intensity of vesicles after dilution. Vesicles of mCherry−Z_E (1.5 μM) and Z_R−ELP (30 μM) were prepared on a glass substrate and diluted 10 times with PBS (0.45 M). After dilution, fluorescence from mCherry−Z_E in a vesicle was monitored by imaging it at 0 min, 5 min, 15 min, and 30 min (A). The change in intensity was quantified by collecting fluorescence profiles (B) from the images in (A).

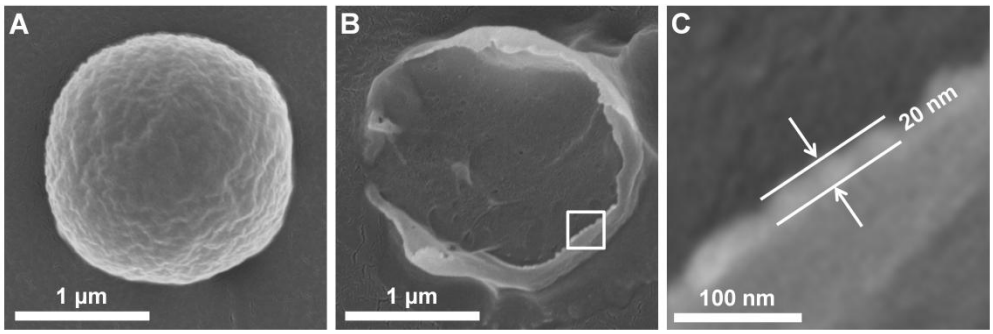

Figure 4.6 SEM images of protein vesicles. A vesicle sample of mCherry−Z_E (1.5 μM) and Z_R−ELP (30 μM) was fixed with glutaraldehyde for 1 h, and freeze-dried. Surface and cross-section were imaged from a non-fractured vesicle (A) and a fractured vesicle (B), respectively. A close-up image from a part of the vesicle in (B) was used to measure thickness of vesicle membrane (C).

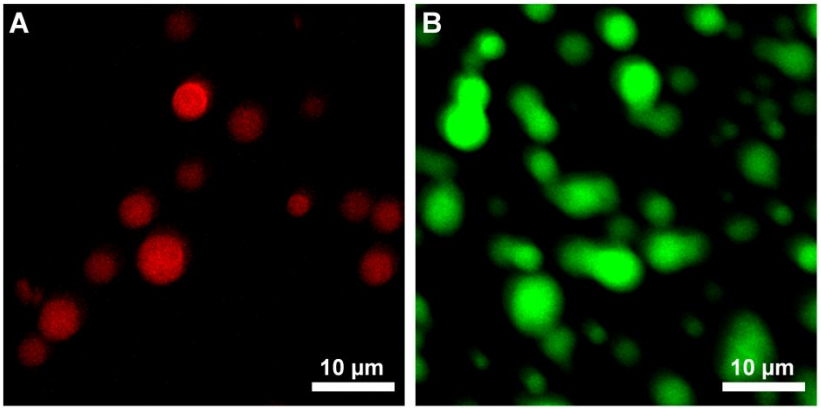

Figure 4.7 Confocal micrographs of protein coacervate. Formation of coacervate was observed from protein mixtures containing different concentrations of the recombinant protein components: (A) 1.5 μM of mCherry−Z_E and 30 μM of Z_R−ELP; (B) 0.6 μM of EGFP−Z_E and 30 μM of Z_R−ELP. The protein mixtures were prepared 4 °C with salt concentration of 0.15 M, and incubated at room temperature for an hour. Fluorescence from either mCherry−Z_E (A) or EGFP−Z_E (B) is visualized by red and green, respectively.

4.3.2 Molecular Packing

As probed by turbidity profiles, molecular packing of vesicles is distinct from that of coacervate particles (Figure 4.8). After an initial rapid increase, saturation of turbidity was observed at the salt concentrations for vesicle formation. It indicates that the surface of vesicles is hydrophilic and stable, which can be achieved via packing of the rod and globule-rod protein blocks. However, there was a slow decrease in turbidity when formation of coacervate particles was favored, either at lower salt concentrations or in the absence mCherry–Z_E or EGFP–Z_E. This decrease is caused by coalescence of protein coacervate particles,[108] which indicates that they have hydrophobic surfaces where ELP motifs are exposed to water.

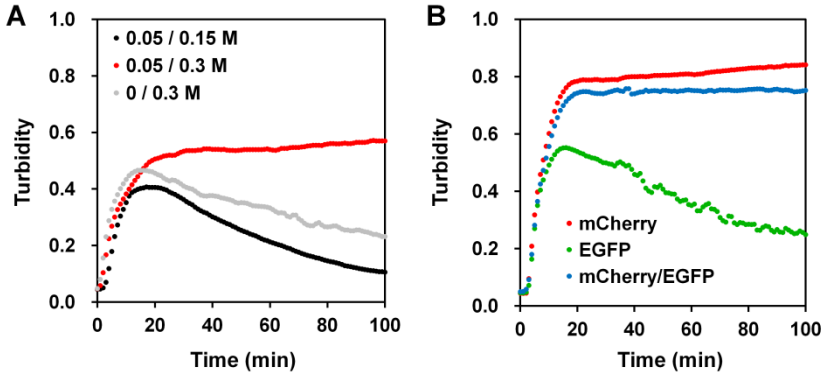

Figure 4.8 Turbidity profiles of protein solutions during inverse phase transition. The optical density at 400 nm was monitored at 25 °C from the solutions prepared at 4 °C. (A) Molar ratio of mCherry–Z_E to Z_R–ELP (χ) was 0.05 and 0 at different salt concentrations (0.15 and 0.30 M). (B) Protein solutions contain 1.5 μM of mCherry–Z_E (red), 0.6 μM of EGFP–Z_E (green), and both (blue) at salt concentration of 0.45 M. All protein solutions contain 30 μM of Z_R–ELP.

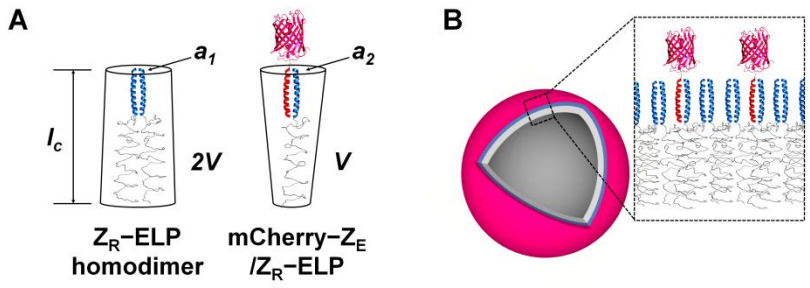

Figure 4.9 Molecular packing of protein complex amphiphiles. (A) Truncated cone models for Z_R–ELP homodimer and mCherry–Z_E/Z_R–ELP to explain the packing parameter *P*. (B) A proposed model of single-layer vesicular membrane.

The effect of salt concentration can be further rationalized using the packing parameter, $P = V/(a_0 l_c)$.[110] *V* is the volume of the hydrophobic (ELP) block, a_0 is the average head area of the hydrophilic block, and l_c is the critical length (Figure 4.9A). The hydrophilic part is composed of the globular domain (mCherry or EGFP) and the rod-shaped coiled coils (mixtures of Z_R/Z_R homodimers or Z_E/Z_R heterodimers). When mCherry–Z_E (or EGFP–Z_E) is mixed with Z_R–ELP, the average head area per single strand of ELP (a_0) is expressed as $a_0 = (1 - \chi)a_1/2 + \chi a_2$, where χ is the molar ratio of mCherry–Z_E (or EGFP–Z_E) to Z_R–ELP, and a_1 and a_2 are the head areas of Z_R/Z_R and mCherry(EGFP)–Z_E/Z_R, respectively (Figure 4.9A). Because of fixed secondary structure and surface properties of the globule and rod blocks, a_0 should not strongly depend on salt concentration. In contrast, *V* is significantly influenced by ionic strength. According to conformational mechanics of ELPs,[111] ELP molecules are more collapsed with increasing salt concentration. Therefore, increased ionic strength reduces *V* and decreases the packing parameter *P*. In this sense, the protein amphiphiles have an inverted cone shape that forms coacervate particles when $P > 1$, below the critical values of salt concentration. Above the critical values, *V* is reduced, and vesicle formation is favored at

$1/2 < P < 1$. Therefore, conformational dependency of ELP on ionic strength seems strongly related to morphologies of the aggregates made from the protein amphiphiles.

Moreover, our argument based on the packing parameter clearly explains why the critical salt concentration is dependent on the type of globular domains. As demonstrated, P is also dependent on the average head area a_0 that changes as a function of the molar ratio χ and a_2. Importantly, the head area a_2 is decided by the nature of globular domains, as they are covalently linked to Z_E/Z_R coiled coils (Figure 4.9A). For example, mCherry is a monomeric and highly soluble globular protein,[112] and a_2 becomes larger than the head area resulted only from a coiled coil ($\sim a_1$) because of steric hindrance provided by the conjugated mCherry domain. In contrast, EGFP tends to dimerize at millimolar concentration[113] or even can aggregate as indicated by the bright spots observed in Figure 4.4B. The attraction between EGFP domains reduces a_2 corresponding to EGFP–Z_E/Z_R block. Thus, the salt concentration required for $1/2 < P < 1$ should be higher for EGFP than mCherry.

Our observation on the correlation between χ and the average hydrodynamic diameter of vesicles (d_H) strongly evidences the influence of globular domains on the packing parameter P. With increasing χ at a given salt concentration, d_H of mCherry–Z_E vesicles decreased while we observed an increase in d_H of EGFP–Z_E vesicles (Figure 4.10). The increased curvature of mCherry–Z_E vesicles at higher χ indicates $a_2 > a_1$, and $a_2 < a_1$ for EGFP-Z_E vesicles since their curvature decreases with increasing χ. Thus, mCherry provides a larger head area (a_2) than EGFP since a_1 is independent of the globular domains. These opposite trends, with equally increased fractions of Z_E/Z_R coiled coils in both systems, indicate that influence from the globular domains seems to be dominant over interactions between Z_R/Z_R and Z_E/Z_R coiled coil domains. Nonetheless, various interactions between the protein domains may exist and contribute to self-assembly.

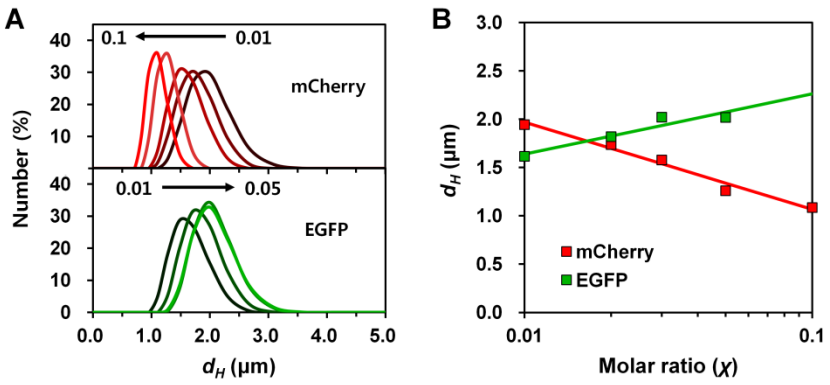

Figure 4.10 Hydrodynamic diameter (d_H) of vesicles with different molar ratios (χ). (A) Size distribution obtained from DLS measurement. Molar ratio of mCherry–Z_E to Z_R–ELP (top), 0.01, 0.02, 0.03, 0.05, 0.1; EGFP–Z_E to Z_R–ELP (bottom), 0.01, 0.02, 0.03, 0.05. Concentration of Z_R–ELP was fixed at 30 μM for all samples at different salt concentrations: 0.30 M (mCherry–Z_E vesicles) and 0.91 M (EGFP–Z_E vesicles). (B) The corresponding correlation between χ and d_H of vesicles containing mCherry–Z_E (red) and EGFP-Z_E (green).

4.3.3 Encapsulation

When vesicle formation conditions are favorable for both globular domains, we found that both mCherry–Z_E and EGFP–Z_E were incorporated into membrane of hollow vesicles (Figure 4.4C). Surprisingly, at a condition where only formation of mCherry–Z_E vesicles is favored, the two globular domains separated into different micro-phases within a vesicle (Figure 4.4D). The confocal micrograph indicates that mCherry–Z_E and Z_R–ELP self-assembled into vesicles whose interior is filled with EGFP–Z_E and Z_R–ELP. Different from the hollow vesicles incorporating both globular domains in the membrane, this condition resulted in vesicles with "core-shell" morphology. According to the observed morphological dependence on salt concentration, the vesicular layer composed

of mCherry–Z_E and Z_R–ELP encapsulates the coacervate phase of EGFP–Z_E and Z_R–ELP, which was simultaneously formed during the inverse phase transition. Again, as probed by turbidity profiles, the saturation in turbidity after phase transition indicates that the "shell" is a stable vesicular membrane of tightly packed protein amphiphiles (Figure 4.8B). At the same salt concentration, however, the turbidity profile for the mixture of only EGFP–Z_E and Z_R–ELP showed a gradual decrease, which indicates formation of typical coacervate particles. This demonstrates that vesicles incorporating multiple types of globular domains in either the membrane or interior compartment can self-assemble by adjusting salt concentration.

Preferential encapsulation of the coacervate phase could be explained by a hypothetical model of vesicles composed of a self-assembled "single-layer" membrane. It is distinguished from "bilayer" membranes of typical block copolymer vesicles. In a bilayer, hydrophilic chains are both inside and outside of vesicles. In our proposed model, the hydrophobic ELP blocks are facing the interior (Figure 4.9B) and the inner surface could stabilize the encapsulated protein coacervate phase. An example of synthetic rod-coil block copolymers demonstrates that they form hollow aggregates where a hydrophobic inner shell encapsulates hydrophobic cargo.[114] Despite the globular domains included in our system, this example shares the same characteristic of rod-shaped blocks directly interfaced with hydrophobic coil blocks. We hypothesize that the rigid, rod-shaped conformations could maintain a low interfacial curvature between the coiled coils and ELP, and may prevent collapse of hollow structure even in the absence of encapsulated coacervate phase.[102] Moreover, our observation of correlation between packing parameter and curvature of vesicles (Figure 4.10) is similar to a characteristic of single-layer superstructures assembled from mesoscopic metal-polymer amphiphiles.[115]

In addition to protein coacervate, encapsulation of small molecules can be simply achieved by mixing with the protein amphiphiles, followed by inverse phase transition. As a model molecule, fluorescein was mixed with mCherry–Z_E and Z_R–ELP at 4 °C and

warmed to room temperature. As a result, the inner space of resulting vesicles was filled with fluorescein, as shown in the confocal micrograph (Figure 4.11A). The level of fluorescein was maintained, indicating low permeability through the vesicle membrane.

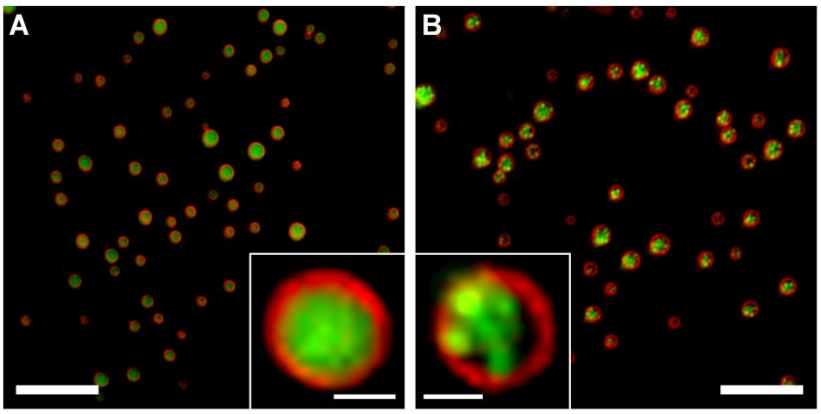

Figure 4.11 Encapsulation of cargo by protein vesicles. Confocal micrographs of vesicles encapsulating (A) fluorescein and (B) polystyrene nanoparticles. Vesicles of mCherry–Z_E (1.5 μM) and Z_R-ELP (30 μM) were self-assembled in the presence of fluorescein (50 μg/mL) or fluorescent polystyrene nanoparticles with diameters of 500 nm (125 μg/mL). Salt concentration was 0.45 M. The green color indicates fluorescence from (A) fluorescein and (B) polystyrene nanoparticles while fluorescence from mCherry–Z_E is visualized by red. The insets are close-up images. Scales bars are 10 and 1 μm (inset), respectively.

Importantly, when mCherry–Z_E vesicles were assembled in the presence of carboxylated fluorescent polystyrene nanoparticles (diameter ~ 500 nm), we observed the nanoparticles located inside the resulting vesicles (Figure 4.11B). The confocal micrograph shows the green fluorescent particles surrounded by the red fluorescent

vesicular membrane. This result could be explained if the vesicle membrane provides a hydrophobic inner wall. Considering the low number density and length scale of the nanoparticles relative to vesicles, encapsulation should be driven by attractive interactions between the hydrophobic nanoparticles and inner wall of the membrane. Indeed, the protein vesicles can encapsulate cargo with multiple length scales: small molecules (~ 10^0 nm), proteins (~ 10^1 nm), and nanoparticles (~ 10^2 nm).

4.4 Conclusion

In conclusion, we describe the aqueous self-assembly of protein vesicles that incorporate globular domains as building blocks via temperature-responsive inverse phase transition. It provides a versatile method to fabricate protein vesicles in biocompatible environments. Thus, folded and biologically functional proteins, such as enzymes or receptor ligands, could be incorporated into vesicle membranes for practical applications. Importantly, the simple and efficient encapsulation of various types of cargo will provide an opportunity for many applications in drug delivery.

CHAPTER 5

SELF-ASSEMBLY OF PROTEIN NANOSHEETS

5.1 Introduction

Sequence-defined biopolymers such as peptides or proteins offer opportunities for programmed self-assembly. Supramolecular interactions dictated by the sequence of biopolymers direct formation of structures with defined geometries that include spheres,[90] cylinders,[88] and fibers.[33] Furthermore, two-dimensional (2D) structures can be assembled from peptides. Recently, self-assembly of 2D nanosheets has been demonstrated using short peptide amphiphiles[116] or collagen-mimetic peptides.[117,118] Self-assembly of those synthetic peptides is driven by amphiphilic properties or charge complementarity between triple helices, respectively. Also, peptoids, poly-N-substituted glycines, have been used to fabricate self-assembled nanosheets.[119,120] Control over the sequence of periodic amphiphilic peptoids allowed electrostatic recognition and aromatic interactions to direct 2D self-assembly.

Recombinant proteins may offer more opportunities in design of self-assembling building blocks. In contrast to short peptides or peptoids, domains with specific secondary structures can be incorporated, which can diversify programmed supramolecular interactions. Formation of various 3D suprastructures including fibers, sheets, and vesicles, was demonstrated in self-assembly of oleosin-based recombinant proteins.[104] However, suprastructures with well-defined 2D geometry have not been achieved yet, although, in nature, such 2D assemblies have been observed in crystalline S-layers.[121]

Here, we describe self-assembly of 2D nanosheets from recombinant proteins. A recombinant protein building block containing two identical rod-shaped leucine zipper coiled coils was designed, and its assembly into 2D nanosheets was directed under

controlled processes. In addition, the self-assembled nanosheets can incorporate folded globular proteins through high-affinity binding of leucine zipper motifs, which is beneficial for further applications.

5.2 Experimental Details

5.2.1 Materials

Ruthenium tetroxide (RuO_4) was purchased from Sigma-Aldrich. PBS (1X, pH 7.4) containing NaCl (137 mM), KCl (2.7 mM), Na_2HPO_4 (10 mM), KH_2PO_4 (1.8 mM) was prepared in the lab.

5.2.2 Self-Assembly of Protein Nanosheets

The first method is stirring-induced self-assembly. After 100 µL of mCherry−Z_E or EGFP−Z_E solution (10 µM) was added to 900 µL of Z_R−C_{10}−Z_R solution (11.1 µM) prepared in PBS (pH 7.4), the protein mixture solution was stirred at 600 rpm for 24 hr at 4°C.

The second method is based on drying of proteins on glass substrates. A solution of Z_R−C_{10}−Z_R (1 mg/ml) was prepared in PBS (pH 7.4), and 10 µL droplets were placed on glass substrates. After drying overnight at ambient conditions, salt crystals formed on the glass substrates were carefully rinsed with PBS. Next, 10 µL of mCherry−Z_E or EGFP−Z_E (1 µM) was applied to the nanosheets on the glass, and incubated for 1 hr. After washing with PBS, the samples were characterized using fluorescence microscopy.

5.2.3 Characterization of Protein Nanosheets

<u>Fluorescence Microscopy</u>

Fluorescence micrographs were obtained with a Axio Observer.Z1 (Carl Zeiss). Samples were placed on glass substrates, fluorescence from mCherry (excitation: 565/30 nm, emission: 620/60 nm) and EGFP (excitation: 474/40 nm, emission: 525/50 nm) was visualized using 10X, 40X, and 100X (oil immersion) objectives.

Scanning Electron Microscopy (SEM)

SEM images were collected on a Hitachi SU8230. After washing with deionized water, 100 μL of sample solution was freeze-dried and mounted on a stub using carbon tape. After sputter coating with gold, the samples were imaged at 12 kV.

Transmission Electron Microscopy (TEM)

TEM images were collected on a JEOL electron microscope (JEOL 100CX) at an acceleration voltage of 100 kV. For TEM imaging, 5μL of protein nanosheets solutions were sampled by dropping on the TEM grids. Samples were stained by an exposure to 0.5% RuO_4 vapor for 20 min.

Fourier Transform Infrared (FT-IR)

FT-IR spectra of protein nanosheets were obtained with a Nicolet iS50 FT-IR spectrometer (Thermo Scientific) in attenuated total reflection (ATR) mode. The spectra were recorded for wavenumbers ranging from 400 to 4,000 cm^{-1}. Samples were prepared on a glass substrate, and transferred onto the ATR crystal.

5.2.4 Circular Dichroism Spectroscopy

A solution of $Z_R{-}C_{10}{-}Z_R$ (10 μM) was prepared in PBS (pH 7.4) and placed in a 0.2-cm-length cuvette. Using a Jasco J-810 spectropolarimeter (JASCO), a CD spectrum was obtained in 1 nm increments within a wavelength range of 200 − 300 nm. Five measurements were accumulated, and converted to mean residue ellipticity.

5.3 Results and Discussion

5.3.1 Free-Floating Colloidal Protein Nanosheets

In Chapter 4, we investigated the ability of the packing parameter to dictate morphology of self-assembled protein structures. Based on our findings, we hypothesized that protein building blocks with cylindrical geometry may self-assemble into sheet-like morphologies. The tri-block copolypeptide $Z_R{-}C_{10}{-}Z_R$ contains two leucine zipper motifs that are connected by a flexible linker. Since the weaker affinity between Z_R motifs ($K_d \approx 10^{-7}$ M) induces formation of a parallel Z_R/Z_R coiled coils,[49] homodimers of $Z_R{-}C_{10}{-}Z_R$ are favored to form in aqueous solution (Figure 5.1A and Figure 2.3). In the dimeric protein complexes, two pairs of the rod-shaped coiled coils (Z_R/Z_R), which are located at both N and C termini, are hypothesized to result in cylindrical geometry, together with the flexible random coil mid-part, C_{10}. In the CD spectrum of $Z_R{-}C_{10}{-}Z_R$ (Figure 5.1B), the peaks at 222 nm indicates presence of α-helical coiled coils. Also, the peak at 206 nm is a characteristic of random coils.[122]

Incubation of protein solutions without agitation did not result in formation of any particles, because Z_R/Z_R coiled coils can only dimerize[49] and C_{10} does not possess spontaneous self-assembling properties.[58] However, when protein mixture solutions were stirred for 24 hr at 4°C, the solution became turbid and formation of fluorescent particles was observed (Figure 5.2A and 5.2B). Fluorescence from the particles indicates that either mCherry$-Z_E$ or EGFP$-Z_E$ was incorporated. Although morphology of the particles was not clear in the fluorescence micrographs, we observed particles that look like rolled sheets in SEM images (Figure 5.2C). Furthermore, a TEM image shows formation of thin, sheet-like particles (Figure 5.2D). The folded area of the sheets (inset image) indicates a thickness of 13.7 nm. Indeed, recombinant protein building blocks self-assembled into nanosheets while globular domains were incorporated.

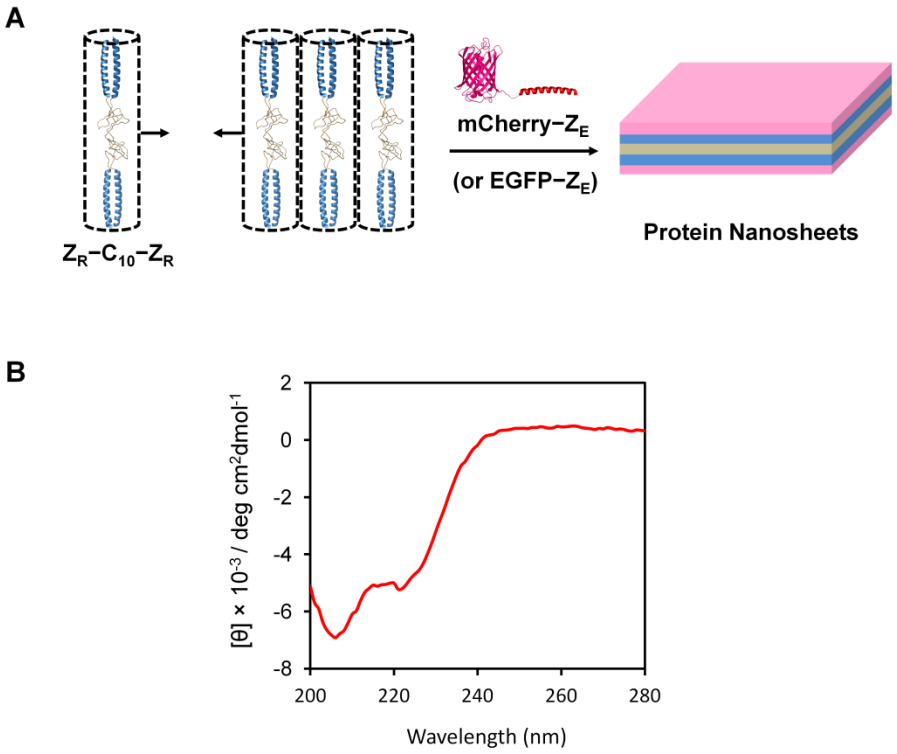

Figure 5.1 Recombinant protein building blocks and proposed lateral self-assembly into nanosheets. (A) Cylindrical protein complexes (homodimers of Z_R–C_{10}–Z_R) self-assemble into nanosheets and mCherry–Z_E (or EGFP–Z_E) is incorporated. (B) The CD spectrum confirms presence of coiled coils which can contribute to the cylindrical geometry.

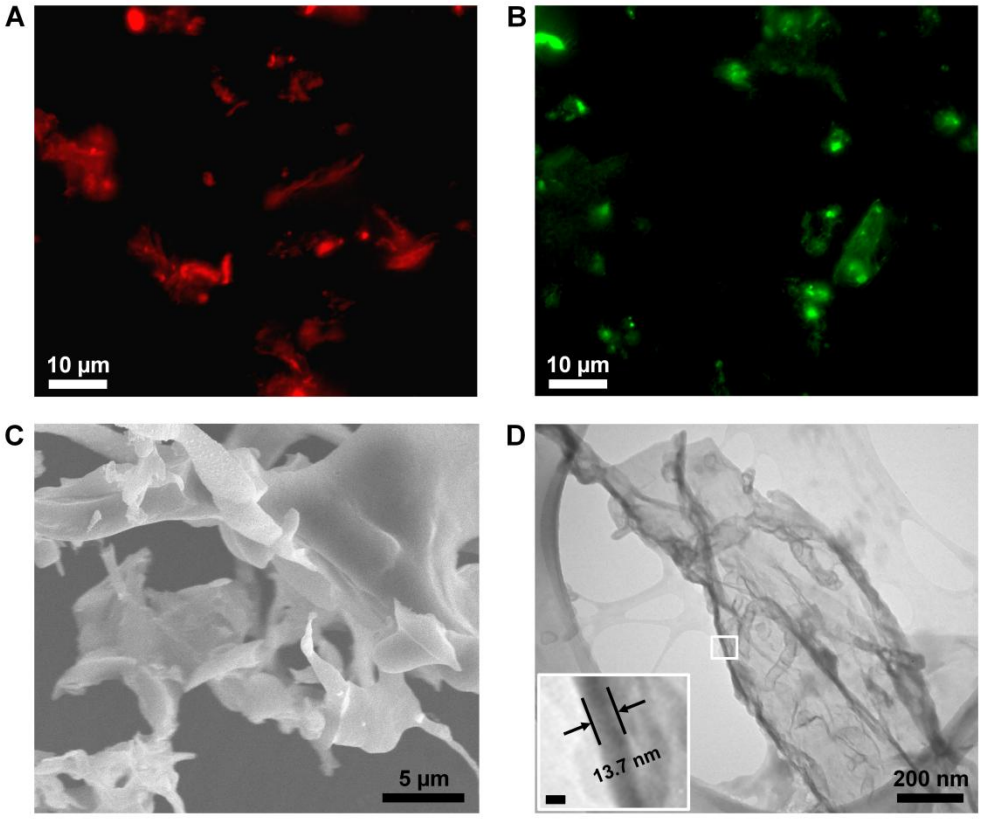

Figure 5.2 Free-floating colloidal protein nanosheets. (A, B) Fluorescence micrographs of protein nanosheets from stirred mixtures: (A) $Z_R{-}C_{10}{-}Z_R$ (10 µM) and mCherry$-Z_E$ (1 µM); (B) $Z_R{-}C_{10}{-}Z_R$ (10 µM) and EGFP$-Z_E$ (1 µM). (C) SEM image of freeze-dried nanosheets prepared in (A). (D) TEM image of RuO_4 stained nanosheets prepared in (A).

5.3.2 Large-Area Protein Nanosheets

Although the stirring-induced self-assembly resulted in formation of particulates with sheet-like morphologies, we further developed processes that can direct self-assembly of large-area nanosheets with a well-defined geometry. Zuckermann *et al.* demonstrated that compression at the air-water interface catalyzes self-assembly of peptoids.[120] Similarly, we hypothesized that flat solid surfaces may serve as a template that can assist in alignment of the cylindrical building blocks. In this process, $Z_R{-}C_{10}{-}Z_R$ was dried on glass substrates, followed by incubation with solutions containing mCherry$-Z_E$ or EGFP$-Z_E$. As a result, large-area fluorescent sheets were formed on the substrates (Figure 5.3). Widths of the sheets were around 180 μm for the volume of solution used, and the fluorescence indicates incorporation of mCherry$-Z_E$ or EGFP$-Z_E$. Also, the sheets were able to be resuspended in solution, although they were significantly folded (Figure 5.3C). We observed formation of wrinkles, which is also a characteristic of sheet-like morphologies (Figure 5.3A and 5.3B).[119,120]

Lateral assembly of cylindrical protein building blocks is our proposed model for molecular packing in nanosheets (Figure 5.1A). Although direct characterization such as high-resolution TEM is required, our observations in FT-IR spectra can be explained by the hypothetical model. The amide I bands for soluble (1645 cm^{-1}) and assembled $Z_R{-}C_{10}{-}Z_R$ (1646 cm^{-1}) were almost identical, indicating $Z_R{-}C_{10}{-}Z_R$ did not undergo conformational transition during self-assembly, for example, from α-helix to β-sheet (Figure 5.4). The result confirms that nanosheets contain α-helical coiled coils. Also, we observed that the peak at 1391 cm^{-1} was significantly reduced when nanosheets were assembled. This peak is assigned for symmetric bending vibration of CH_3 groups,[123] which are dominantly present in alanine-rich C_{10}. With normalization of the amide I bands, such a decrease in intensity of the peak can be indicative of changes in interactions between and the CH_3 groups and surroundings. Thus, we hypothesize that the hydrophobic side chains of C_{10} might contribute to attraction between building blocks.

Under these observations, lateral assembly of cylindrical building blocks is a plausible scenario.

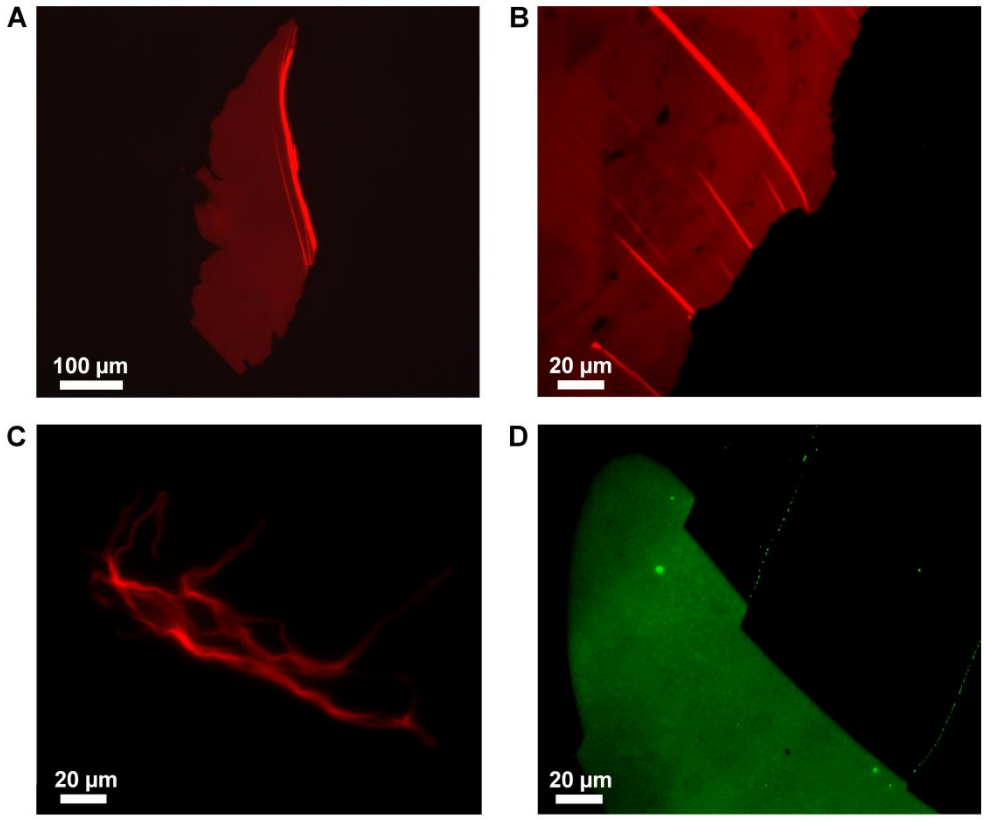

Figure 5.3 Large-area protein nanosheets. (A-C) Fluorescence micrographs of protein nanosheets from drying of $Z_R{-}C_{10}{-}Z_R$ followed by incubation with mCherry$-Z_E$ (1 µM) (A, B). The nanosheets are resuspended in PBS (C). (D) Nanosheets of $Z_R{-}C_{10}{-}Z_R$ incubated with EGFP$-Z_E$ (1 µM).

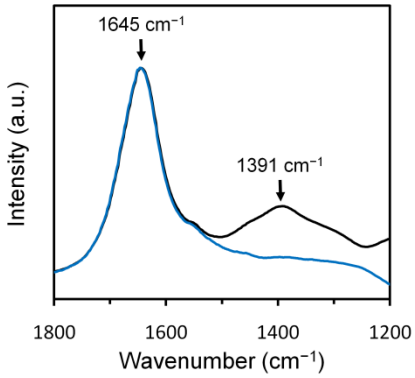

Figure 5.4 FT-IR spectra of soluble (black) and assembled Z_R–C_{10}–Z_R (blue).

The underlying mechanism for drying-induced self-assembly needs to be elucidated. Although we hypothesized that a substrate surface may serve as template, it is also possible that the air-water interface of droplets might direct self-assembly. Real-time observation of the self-assembly process may be a route to gain more mechanistic information, for example, by using dye-conjugated Z_R–C_{10}–Z_R protein building blocks and time-lapse fluorescence microscopy. For example, nucleation and growth behaviors might be visualized.[124] Acquisition of such information will also allow improved control in protein self-assembly processes for fabrication of larger or more uniform sheets or other morphologies.

5.4 Conclusion

We described self-assembly of nanosheets from recombinant proteins, which was induced by stirring or drying. The drying-induced self-assembly resulted in formation of large protein sheets (>180 μm in width), and folded protein domains such as mCherry or EGFP were incorporated into nanosheets. We propose a model that cylindrical building

blocks laterally self-assemble into nanosheets. Our strategy can allow scaled-up production of large-area protein nanosheets. The unique morphology with incorporated folded proteins will offer opportunities for applications such as protein delivery, wound repair, or biosensors.

CHAPTER 6

HIERARCHICALLY STRUCTURED POROUS PROTEIN-INORGANIC HYBRID SUPRAPARTICLES

6.1 Introduction

Structural features of biominerals, the natural composite materials, include complexity in morphology and hierarchy at multiple length scales. In nature, diverse biominerals share the common feature of hierarchy in their structures.[125] Bones,[126] teeth,[7] and hard components from many organisms[127] are composed of highly organized inorganic nanocrystals and biomolecules, and the complex hybrid structures are produced through biomineralization.[126] During the natural process, biomolecules interacting with mineral phases regulate formation of biominerals, which is followed by arrangement of hybrid nanostructures into higher-order structures at the microscale.[7,126] There have been attempts to mimic nature's strategy to fabricate composite materials by biomineralization. In artificial approaches, various macromolecules including proteins,[128,129] peptides,[130] and synthetic polymers[131,132] have been used as biotemplates. However, arrangement of biominerals beyond their growth on the templates was not achieved. Rational design of biomimetic strategies to create complex structures has been challenging because the fundamental growth mechanism for biominerals remains largely hypothetical.[130] Recent studies have demonstrated strategies to fabricate more complex hierarchical structures in which biominerals nanocrystals were aligned.[133,134] Nonetheless, arrangement of inorganic nanocrystals and organic phases into hierarchically ordered structures in three-dimensions is a long-sought goal in the design of artificial biominerals. Also, simplicity and reproducibility of fabrication methods are critical for practical application of nanocomposite materials.

Here, we report a simple strategy to fabricate hierarchically structured protein-inorganic hybrid supraparticles. Recently, synthesis of artificial protein-inorganic hybrids with flower-like shapes has been reported.[135,136] The hybrid particles are composed of petal-like plates, which are interconnected into the flower shapes. Motivated by this shape, we used flower-shaped particles as building blocks that can self-assemble into higher-order architectures. In our system, we created flower-shaped protein-calcium phosphate hybrid nanoparticles which assemble into chain-like clusters. The pores and petals of nanoparticles provide "interlocking" interactions by their self-complementary geometry. By controlling assembly behavior, the building blocks were arranged into supraparticles with pores at both the nano- and microscales.

In addition to hierarchical structure, the hybrid supraparticles provide high-affinity binding sites for robust protein immobilization. Proteins can be stabilized through immobilization on solid supports,[137] which are beneficial for applications such as biocatalysis and biosensors. One strategy is to create fusion proteins that have a binding affinity to supports. The supraparticles incorporate leucine zipper motifs, to which fusion proteins that carry the pairing zipper motifs can specifically bind with femtomolar affinity. Our approach enables immobilization of various types of proteins as it is based on specific binding affinity between leucine zipper motifs, not protein-specific interactions such as binding interactions between allosteric sites of enzymes and calcium ions.[136]

6.2 Experimental Details

6.2.1 Materials

Calcium chloride dihydrate ($CaCl_2 \cdot 2H_2O$) was purchased from Fisher Chemical. Concentrated PBS (10X, pH 7.4) containing NaCl (1.37 M), KCl (27 mM), Na_2HPO_4

(100 mM), KH_2PO_4 (18 mM) was prepared in the lab and used to dissolve proteins and adjust salt concentration in aqueous solution.

6.2.2 Synthesis and Characterization of Hybrid Nanoparticles

Lyophilized recombinant fusion protein $Z_R{-}C_{10}{-}Z_R$ was dissolved in deionized water at a concentration of 1 mg/ mL, and diluted into 0.1 mg/mL in 1X PBS (pH 7.4). An aqueous solution of $CaCl_2$ (160 mM) was prepared, and 10 µL was added to 1 mL of $Z_R{-}C_{10}{-}Z_R$ solution (0.1 mg/ mL). The mixture solution was left undisturbed for 1 day at room temperature. The hybrid nanoparticles formed in solution were characterized with optical microscopy (Axio Observer.Z1, Carl Zeiss). On a glass substrate, 5 µL of sample was placed and imaged using a 100X oil immersion objective. Also, the nanoparticles were washed by centrifugation and resuspended in deionized water. Then, 5 µL of the washed nanoparticles were dried on aluminum substrates overnight at room temperature for SEM characterization using Zeiss Ultra60 FE-SEM (Carl Zeiss). The samples were sputter-coated with gold and imaged at 5 kV. As a control, 10 µL of $CaCl_2$ was added to 1 mL PBS without any proteins, and the resulting precipitates were collected, washed, and imaged with SEM following the same procedures.

6.2.3 Colloidal Assembly and Characterization of Supraparticles

After addition of 10 µL of $CaCl_2$ (160 mM) into 1 mL of $Z_R{-}C_{10}{-}Z_R$ solution (0.1 mg/ml), a microtube (volume: 2 mL) containing the mixture solution was immediately placed in a rotator (Thermo Scientific). Rotation (8 rpm) was continued for 2 days at room temperature. Next, the resulting solution was collected and mixed with 14 mL of deionized water. After sitting undisturbed overnight at room temperature, 14 mL of supernatant was carefully removed. Again, 14 mL of deionized water was added, and

supernatant was removed after 1 hr incubation. The resulting supraparticles in solution were characterized using optical microscopy (10X or 40X objectives). Dried samples were characterized using SEM, following the same procedures of sample preparation mentioned above. For characterization of cross-sections, dried supraparticles on the substrate were fractured by rubbing with tweezers. To monitor the assembly process, samples were taken at 30 min, 2 hr, 8 hr, and 24 hr during rotation, and imaged using optical microscopy (10X objective).

6.2.4 Protein Immobilization

Solutions containing 5 μM of mCherry−Z_E or EGFP−Z_E were prepared in 1X PBS (pH 7.4). Then, 20 μL of the solution of mCherry−Z_E was added into 80 μL of the supraparticle solutions, which was incubated for 1 hr at room temperature. For immobilization of multiple proteins, 20 μL of mCherry−Z_E solution (5 μM) was added into 60 μL of the supraparticle solutions and incubated for 10 min, followed by addition of 20 μL of EGFP−Z_E solution (5 μM). The mixture solution containing supraparticles, mCherry−Z_E, and EGFP−Z_E were incubated for 1 hr at room temperature. For characterization of protein immobilization, 5 μL of samples were taken and placed on a glass substrate. Using a confocal microscope (Zeiss LSM 510 Vis, Carl Zeiss), fluorescence from the fusion proteins immobilized on the supraparticles was visualized and intensity profiles were quantified from the fluorescence images. All supraparticle samples were imaged using a 40X objective. The images with EGFP fluorescence was acquired using a 488 nm Argon laser line with high pass (LP 505) emission filter, and mCherry fluorescence were imaged using a 543 nm He-Ne laser line with band pass (BP 565−615) emission filters.

6.3 Results and Discussion

6.3.1 Flower-Shaped Hybrid Nanoparticles

We first prepared a recombinant fusion protein that can form a hybrid with calcium phosphate. In calcium-binding protein domains, oxygen atoms of the carboxyl groups in aspartic acids or glutamic acids, and backbone chains have coordination with calcium ions.[138,139] We hypothesized that the artificial random coil C_{10} can coordinate with calcium ions. A single chain of C_{10} contains ten glutamic acid residues. Also, it is flexible in conformation,[59] which may allow oxygen atoms in the backbone chain to have coordination with calcium ions. Similarly, in the synthesis of protein-copper phosphate hybrid nanoflowers, it was proposed that nitrogen atoms accessible to the ions in solvent have coordinated interactions with copper ions.[135] From a practical aspect, C_{10} was combined with a high-affinity protein motif (Z_R) into a tri-block copolypeptide $Z_R{-}C_{10}{-}Z_R$ (Figure 6.1). That way, the hybrid of calcium phosphate and $Z_R{-}C_{10}{-}Z_R$ can provide affinity-binding sites to recombinant proteins carrying Z_E via robust binding with femtomolar affinity.[49] This property is considered to be beneficial for protein immobilization. Since Z_R is α-helical and contains only few glutamic acid residues, it is hypothesized that C_{10} would dominantly interact with calcium ions. As described in Chapter 2, $Z_R{-}C_{10}{-}Z_R$ was produced from an *E. coli* expression system.

Next, the protein-calcium phosphate hybrid particles were synthesized by co-precipitation of calcium and phosphate ions in the presence of $Z_R{-}C_{10}{-}Z_R$ (Figure 6.1). Upon addition of calcium chloride into solution of $Z_R{-}C_{10}{-}Z_R$ prepared in PBS, immediate precipitation of calcium phosphate was observed. As shown in Figure 6.1, formation of flower-shaped particles was confirmed from SEM images. The flower-like shape is composed of petal-like plates with an average thickness of 15 nm, and the diameter of a whole particle ranged between 445 and 584 nm. In contrast, calcium phosphate precipitated in the absence of $Z_R{-}C_{10}{-}Z_R$ had only plate-like morphology

(Figure 6.1). It evidences our hypothesis that Z_R–C_{10}–Z_R has coordinated interaction with calcium ions, which might be involved in nucleation of calcium phosphate and subsequent growth into the flower-like morphology.

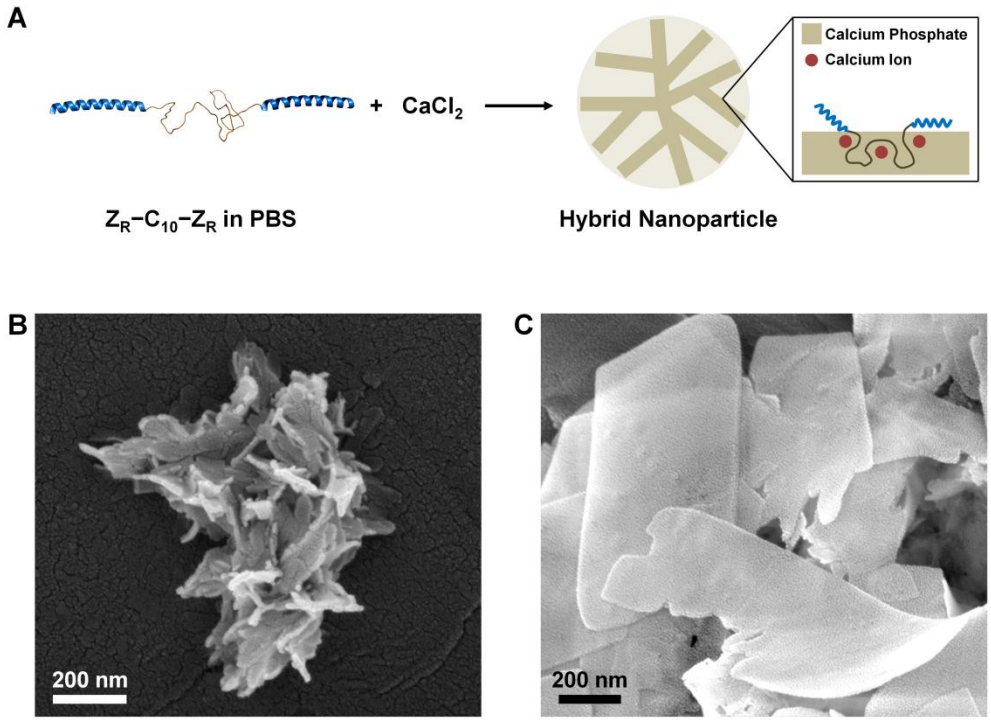

Figure 6.1 Synthesis of flower-shaped hybrid nanoparticles. (A) Scheme of co-precipitation of calcium phosphate and Z_R–C_{10}–Z_R. (B) SEM image of a hybrid nanoparticle. (C) Calcium phosphate plates precipitated in the absence of Z_R–C_{10}–Z_R.

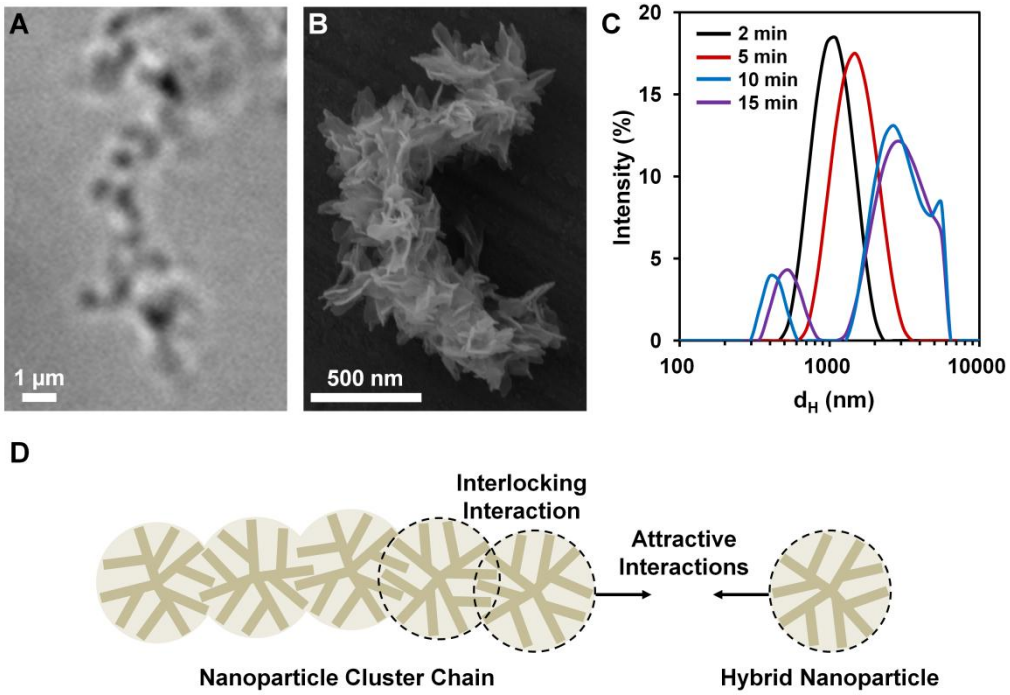

Figure 6.2 Clusters of the flower-shaped nanoparticles. (A) A bright field image of self-assembled cluster chains in aqueous solution. (B) SEM image of a cluster chain. (C) DLS measurement of the cluster chains in aqueous solution: the size distribution curves were obtained at 2 min, 5 min, 10 min, and 15 min after formation of the hybrid nanoparticles was initiated. (D) Schematic illustration of colloidal assembly of nanoparticles clusters.

Surprisingly, the flower-shaped hybrid nanoparticles started to assemble into chain-like clusters immediately after their synthesis. In aqueous solution, formation of colloidal clusters was observed, and they were also imaged by SEM after drying in ambient conditions (Figure 6.2A,B). In the chain-like clusters, the edges of petals were placed in the space between petals of other particles, resulting in overlapping of the boundaries of particles. DLS measurement indicates that hydrodynamic diameter of the particles was 1084 nm at 2 min after the co-precipitation, and it increased up to 2964 nm

at 15 min as a result of the subsequent colloidal assembly (Figure 6.2C). The size of the clusters increased over the limit of DLS measurement and settled at the bottom of the cuvette after 30 min.

As illustrated in Figure 6.2D, the anisotropic assembly of the hybrid nanoparticles can be explained by considering attractive forces, interlocking interactions, and steric hindrance of the side of chains. The petals of calcium phosphate are nanoscale, and such nanocrystals of calcium phosphate are prone to agglomerate due to van der Waals forces.[140] In a flower-shaped particle, several petals form a fixed configuration where the edge of petals and the pores between petals can have complementary geometry for a "interlocking" interaction.[141] When petals are located inside the pores, attraction due to van der Waals forces can be increased. Thus, the free energy of the system would reach a local minimum as a result of assembly. The interlocking interaction at this "self-complementary" geometry is distinguished from the "lock-and-key" interaction,[142] which is driven by excluded volume effect.[142] While mediated by depletion interactions, the free energy of the system is reduced by an increase of the entropy of depletant in the exclusion volume. In our system, assembly is assumed to be driven by van der Waals forces, and is irreversible. Additionally, assembly of a nanoparticle to the side of cluster chains is sterically hindered. On the side, the petals that are not involved in the interlocking interaction can prevent access of additional particles. Thus, addition of a particle would be favored at the end of clusters. Similarly, anisotropic assembly was also observed in the example of branched colloidal nanocrystals.[141]

6.3.2 Supraparticles Assembled from the Hybrid Nanoparticles

Although the chain-like clusters of the hybrid nanoparticles is an interesting morphology, they are varied in length and susceptible to shear-induced deformation. Instead, we were motivated to exploit the clustering behavior to build hierarchically

structured and porous hybrid supraparticles. Still, there are challenges for controlled assembly of the nanoparticles. First, the steric hindrance between the sides of cluster chains can prevent their assembly into higher-order structures. Second, as the hybrid nanoparticles grow into micrometer-sized clusters, they tend to settle to the bottom of a container, significantly reducing collision frequency between long and short chains.

We hypothesized that rotation of nanoparticles solutions can solve these problems and may control the colloidal assembly. Continuous expansion and contraction of the air-water interface by rotation can induce compression of objects adsorbed at the interface,[120] which might allow alignment of the cluster chains of nanoparticles. Upon precipitation, the solution was placed in a rotator and the solution was continuously rotated for 2 days at room temperature. As a result, we observed formation of spherical microparticles with an average diameter of 29.7 ± 10.5 μm (Figure 6.3B). Close-up optical microscopy images (Figure 6.3C) also show the internal structures of the resulting supraparticles. We further characterized the supraparticles using SEM. Although they shrink slightly during drying process, the dried supraparticles show hierarchical pore structures on the surfaces (Figure 6.3D,E).

Surface morphology of the supraparticles evidences that they are assembled from the flower-shaped hybrid nanoparticles. Groups of petals form porous structures at the nanoscale while the nanoparticles cluster to result in pores at the microscale (Figure 6.4A,B). Although the petals on the surface look a little compressed, the overall surface morphology of the supraparticles indicates that they are formed through an assembly of the clusters. Indeed, the flower-like structural characteristics of individual nanoparticles were translated into the hierarchical morphology of the self-assembled supraparticles.

Interestingly, we observed a spatial difference in density of nanostructures throughout the supraparticles. As shown in the SEM image of the cross-section (Figure 6.4C-E), relatively sparser packing of nanostructures was observed in the middle of the

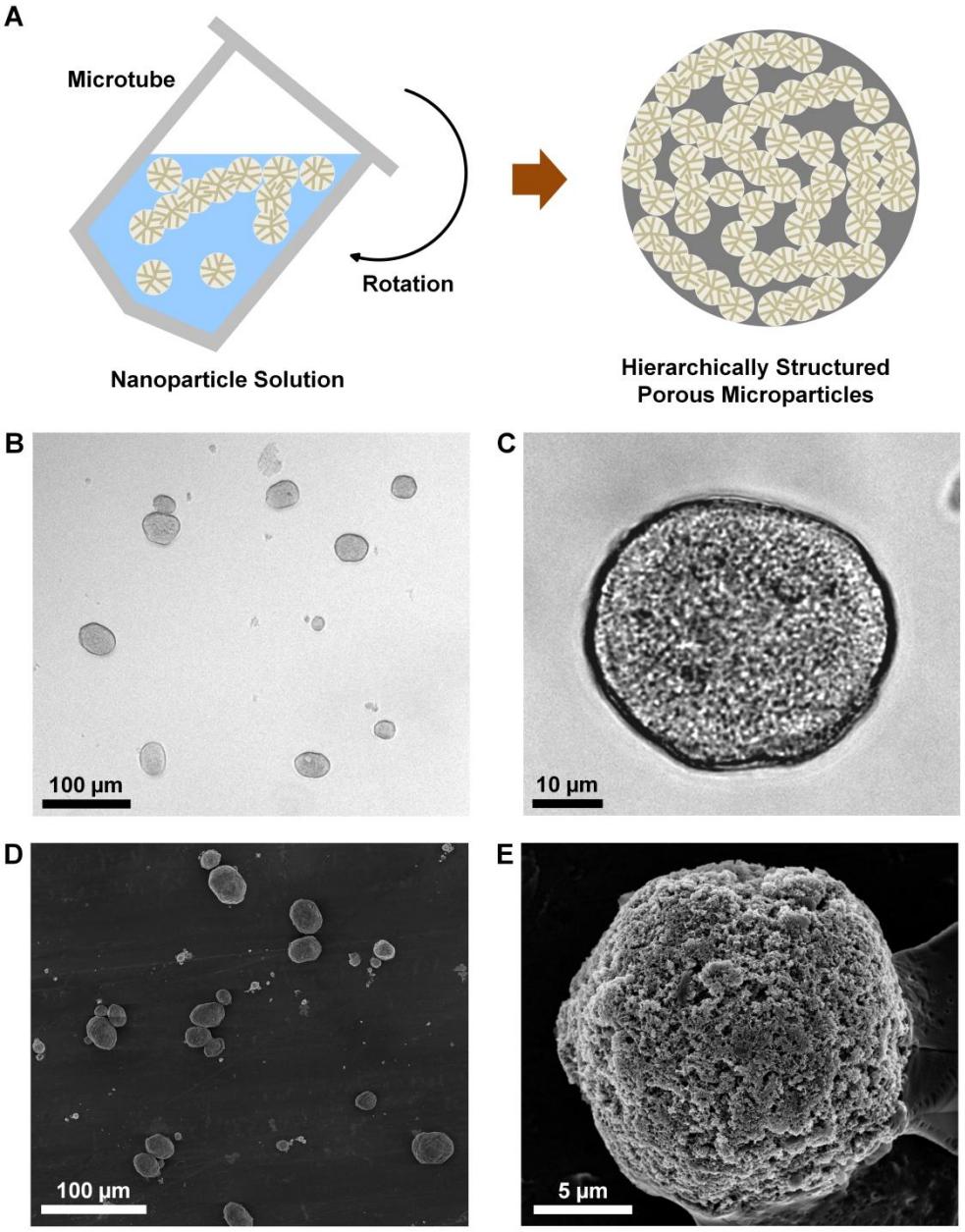

Figure 6.3 Colloidal assembly of flower-shaped hybrid nanoparticles into hierarchically structured porous supraparticles. (A) Scheme of the rotation method that drives colloidal assembly. (B, C) Bright field images of supraparticles in aqueous solution. (D, E) SEM images of the supraparticles dried on substrates.

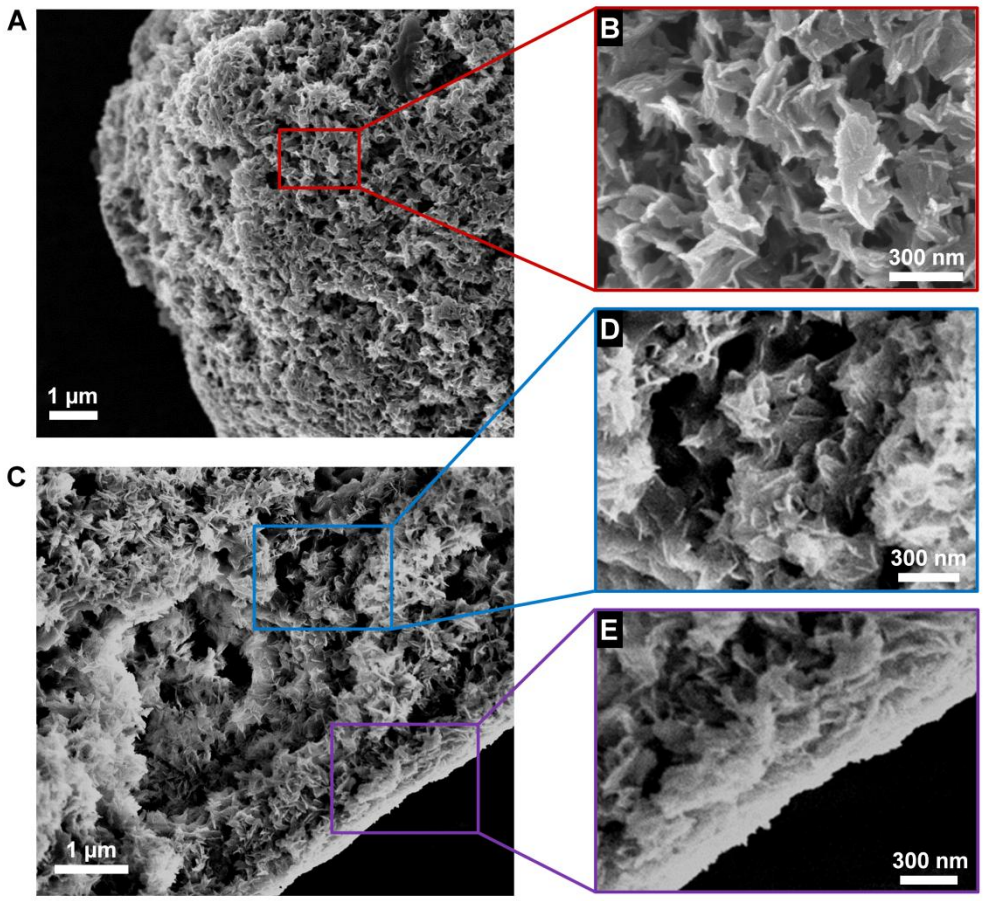

Figure 6.4 Morphology of self-assembled supraparticles. (A, B) SEM images showing surface morphology of a supraparticle. (C) Cross-section image of a fractured supraparticle: the core and rim regions in the cross-section are imaged in (D) and (E), respectively.

supraparticles whereas there was a dense packing in the rim. According to the morphologies, it is speculated that packing of cluster chains might have first occurred to form the core, followed by assembly of additional clusters to surface of the core. In this scenario, stacking of shorter cluster chains on the core seems to lead to higher structural density in the rim.

This scenario should be strongly related to the growth mechanism of the supraparticles. In order to investigate the mechanism, we monitored formation of supraparticles as a function of time during rotation of solutions (Figure 6.5). At the early stage (30 min), spherical agglomerates (arrowed, red) were formed while the majority of flower-shaped nanoparticles remained as giant networks of cluster chains. Interestingly, we could also observe rod-shaped particles (arrowed, blue) in this early stage. At 2 hr, formation of spherical agglomerates (arrowed, red) was also observed whereas the size of giant networks of cluster chains was much reduced. As assembly proceeded for 8 hr, more spherical supraparticles with higher contrast were observed, which indicates that structural density of the supraparticles was increased. After 24 hr, larger supraparticles with clear rims were observed while the size and number of cluster chains were reduced. According to the observations, our hypothesis for growth mechanism is that spherical agglomerates are first formed in the early stage and they serve as “seeds” on to which more clusters are assembled in the following stages. Both increased contrast and clear rims of supraparticles indicates formation of denser packing on the seeds. Thus, our hypothetical growth mechanism is consistent with the observed spatial difference in structural density inside supraparticles.

Formation of rod-shaped supraparticles in the early stage indicates that rotation method enabled lateral assembly of linear cluster chains. It is consistent with our design rational that compression at the air-water interface might allow alignment of the cluster chains. Since linear clustering of the flower-shaped nanoparticles up to several micrometers might not be dominant, we believe that only a fraction of rod-shaped

supraparticles forms while bent chains assemble into the spherical seed particles. In a control experiment, we left a nanoparticle solution stagnant for 24 hr while exposed to the air-water interface. In another control experiment, a microtube was filled up with a nanoparticle solution and no air was allowed in the tube, followed by rotation for 24 hr. We only observed networks of cluster chains, no spherical supraparticles, in the solutions from each control experiment (Figure 6.6). The result evidences that both rotation and the air-water interface are critical for formation of supraparticles. Thus, we can conclude that the rotation method successfully induced compression of the nanoparticle clusters at the air-water interface.

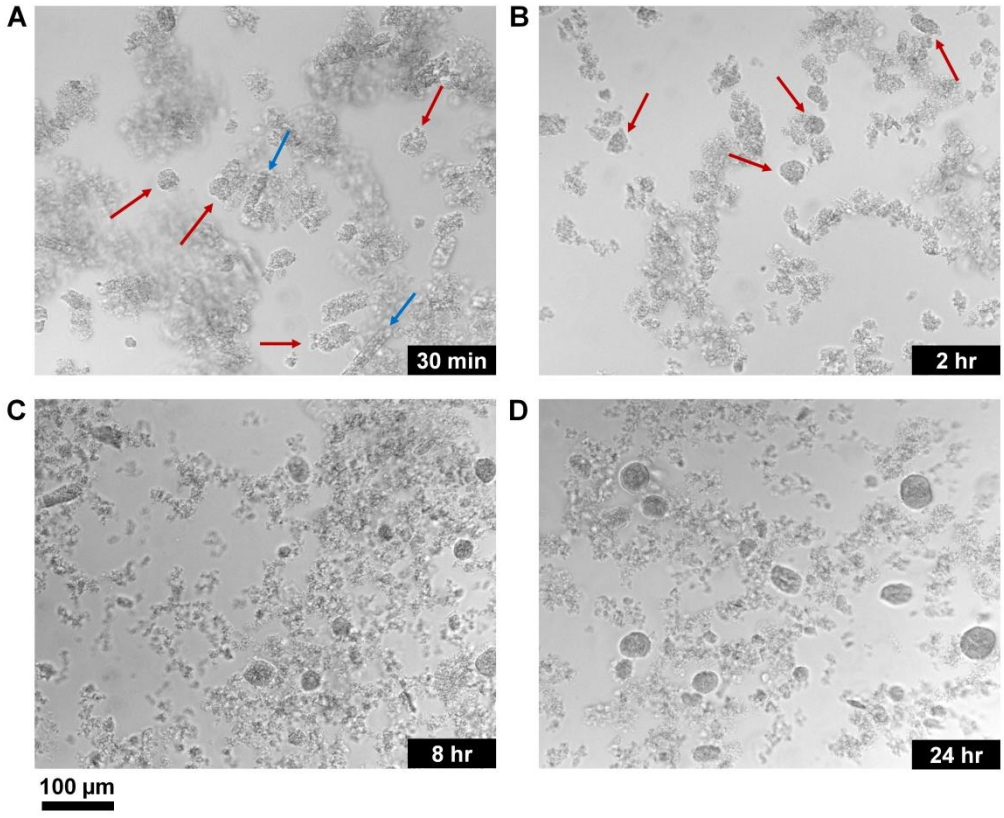

Figure 6.5 Growth of self-assembled supraparticles. (A-D) Bright field images of samples from rotating solution at 30 min (A), 2 h (B), 8 h (C), and 24 h (D). The arrows indicate the spherical (red) and rod-shaped (blue) seed particles formed in the early stages.

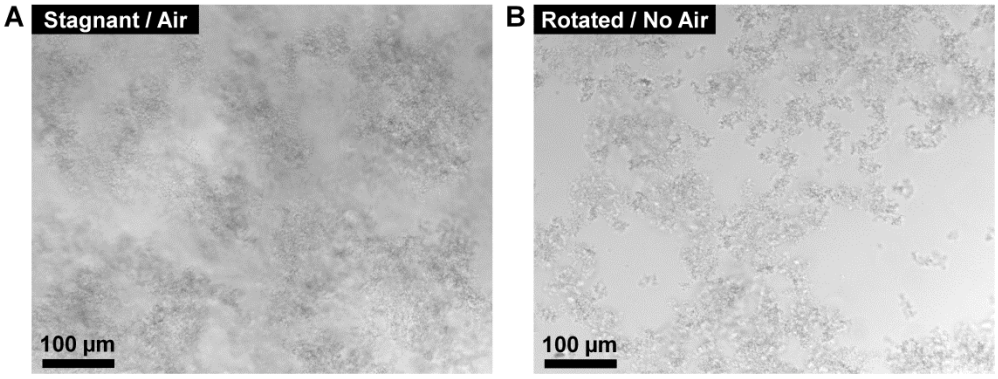

Figure 6.6 Control experiments of colloidal assembly. (A, B) Bright field images of nanoparticles clusters from a solution left stagnant for 24 hr (A) and from a solution rotated for 24 hr without exposure to the air-water interface.

The proposed growth mechanism is analogous to "Ostwald ripening" which has been applied to explain growth of crystals.[143] The spherical seeds formed in the early stage might have lower free energy whereas networks of cluster chains might be relatively unstable. Thus, we hypothesize that growth of seeds into larger particles by addition of small clusters is thermodynamically favored. Rotation continuously generates shear that can deform the giant networks of clusters into smaller pieces. Moreover, formation of seeds and subsequent growth seem to be catalyzed by compression at the air-water interface.

6.3.3 Immobilization of Fusion Proteins

An important feature of the protein-calcium phosphate hybrid supraparticles is to provide affinity binding sites for protein immobilization. Fusion proteins containing Z_E motifs can bind to the Z_R motifs of the incorporated $Z_R{-}C_{10}{-}Z_R$ through the femtomolar affinity between Z_E and Z_R.[49] We used fluorescent proteins as model proteins to

characterize protein immobilization. After incubation of mCherry−Z_E for 1 hr, we could measure red fluorescence of the supraparticles, which indicates immobilization of mCherry−Z_E (Figure 6.7). Furthermore, the fluorescence micrographs show that the supraparticles are composed of submicron clusters. Also, the highest fluorescence intensity was observed at the rim while the intensity in the core was much lower. It is consistent with the spatial difference in structural density (Figure 6.4). Considering the hydrodynamic diameter of mCherry−Z_E, the macroporous supraparticles would not result in mass transfer barriers that can cause the gradient of fluorescence intensity.

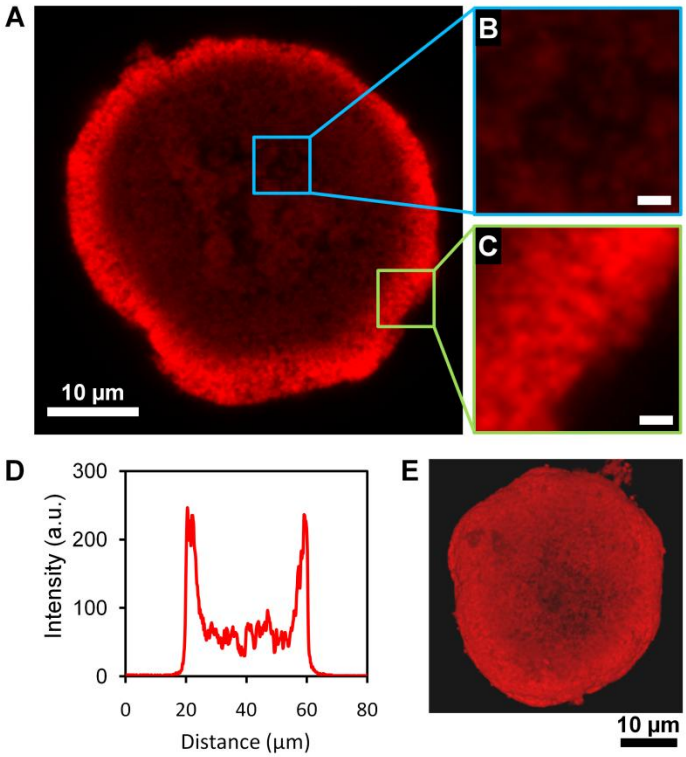

Figure 6.7 Immobilization of mCherry−Z_E. Confocal micrographs of supraparticle incubated with mCherry−Z_E: (A) A center confocal slice of a supraparticle. (B, C) Close-up images of the core and rim regions are in (B) and (C), respectively. (D) The fluorescence intensity profile from the image in (A). (E) Three-dimensional (3D) Z-stack image of the supraparticle images in (A). Scale bars in (B) and (C): 1 µm.

Furthermore, multiple proteins can be immobilized. When both mCherry−Z_E and EGFP−Z_E were incubated, both proteins were immobilized on the supraparticles. The red and green fluorescence of the supraparticle confirms their immobilization (Figure 6.8). Co-localization of multiple types of proteins in a porous support is attractive for applications that require a synergistic interplay between different proteins in proximity such as enzyme cascades.[144] Overall, our approach offers a simple method to immobilize proteins to supraparticles in aqueous phase, without involving complicated processes or use of organic solvents. Also, such immobilization through specific affinity can allow stabilization of enzymes with the control of their orientation.

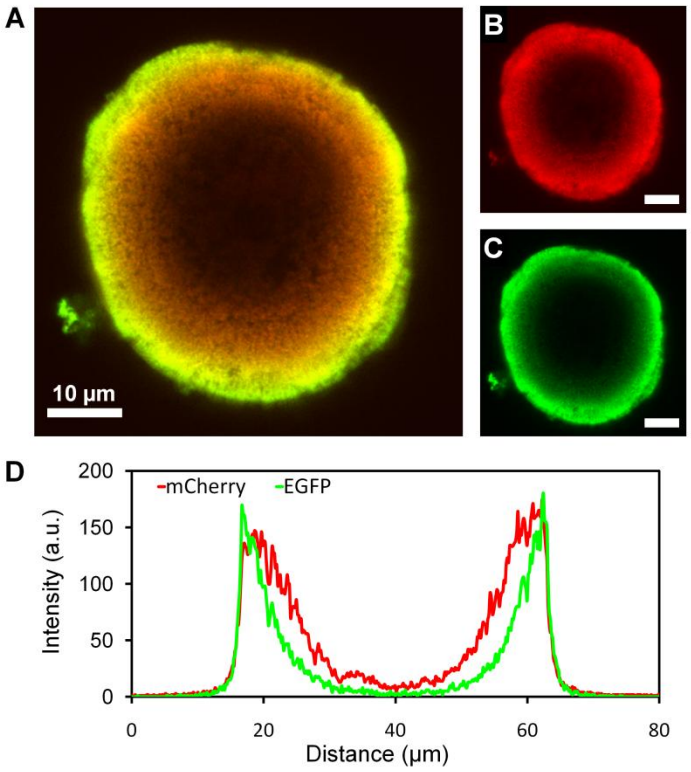

Figure 6.8 Immobilization of multiple proteins, mCherry−Z_E and EGFP−Z_E. (A-C) A center confocal slice of a supraparticle: an overlay (A), red (B), and green fluorescence (C). (D) The fluorescence intensity profiles from the overlay image (A). Scale bars in (B) and (C): 10 μm.

6.4 Conclusion

We have demonstrated fabrication of hierarchically structured porous protein-inorganic hybrid supraparticles. It is a simple method to build porous particles with complex morphologies, which is achieved by interfacial assembly of self-clustering flower-shaped nanoparticles. We also investigated the growth mechanism that resulted in a structural gradient inside particles. Moreover, the incorporated protein $Z_R{-}C_{10}{-}Z_R$ provided high-affinity binding sites for fusion proteins containing the assembling pair Z_E motifs. We anticipate enhancement of stability or biological activity of immobilized proteins such as enzymes, which could be beneficial for many applications.

CHAPTER 7

PROTEASE-IMMOBILIZED SUPRAPARTICLES FOR INACTIVATION OF TUMOR NECROSIS FACTOR-ALPHA

7.1 Introduction

Tumor necrosis factor-alpha (TNF-α), a pro-inflammatory cytokine, plays an important role in inflammation.[145] Because of its role in inflammatory environments, TNF-α has been a therapeutic target for treatments for autoimmune diseases such as rheumatoid arthritis.[146,147] Anti-TNF-α antagonists including soluble TNF receptors (TNFR) and anti-TNF-α antibodies have been developed and approved for human use.[148,149] For instance, Etanercept is the recombinant human TNFR2 coupled with Fc portion of human antibody, and Infliximab and Adalimumab are humanized mouse and human monoclonal anti-TNF-α antibodies. These antagonists are based on affinity binding toward TNF-α, which may be reversible and the anti-TNF-α antagonists may serve as a TNF-α reservoir.[150] Moreover, infection risks are present during systemic inhibition of both soluble and trans-membrane TNF-α.[151,152] Systemic administration of TNF antagonists can also chronically dampen physiologic functions of TNF-α.[153] Thus, a new type of TNF-α inhibitor and strategies for local delivery are required for reduced adverse effects in the treatment of diseases related to chronic inflammation.

Arginine-specific gingipains (Rgps) are pathogen-derived cysteine proteases, which can inactivate TNF-α by proteolytic degradation. They are secreted from *P. gingivalis*, and prevent inflammatory responses by degrading TNF-α during infection.[64,154] Since TNF-α is degraded, use of an Rgp as a TNF-α inhibitor does not cause risks of reversible activation of TNF-α. However, wild type Rgps are immunogenic and cause hemagglutination.[155] RgpA contains multiple adhesin domains including the hemagglutinin-adhesin domain. Moreover, cell-surface receptors, for example, the

fibronectin receptor (α5β1 integrin) and protease-activated receptors (PARs) are susceptible to degradation by wild type Rgps.[63,156] Especially, the complex of RgpA and lysine-specific gingipain (Kgp) binds to a variety of extracellular proteins and is involved in degradation of surface proteins on epithelial, fibroblast and endothelial cells. The monomeric Rgp (RgpB) is lack of adhesin domains, but the N-terminal sequence including catalytic domain is homologous to RgpA.[63] The catalytic domain is similar to caspases, and the S1 pocket at the active site accommodates arginine side chains.[157]

Our strategy is to exploit only the catalytic domain of RgpA and immobilize it to porous supraparticles. In this way, adhesin domains are removed and immobilization can allow proteolysis of only soluble targets. Also, the supraparticles may enable local delivery of the enzymes with enhanced stability. In this study, we engineered a recombinant Rgp fusion protein, and investigated its function for inactivation of TNF-α. The catalytic domain of RgpA was extracted and fused with a leucine zipper motif. The fusion protein was immobilized to porous supraparticles, which were described in Chapter 6, and both soluble and immobilized enzymes were studied.

7.2 Experimental Details

7.2.1 Materials

Human TNF-α recombinant protein was purchased from Thermo Scientific and R & D Systems. Fluorescein-5-isothiocyanate (FITC) and actinomycin D were purchased from Sigma-Aldrich. Murine fibroblast L929 cells, RPMI-1640 medium and fetal bovine serum (FBS) were purchased from ATCC. The 3-4,5-dimethylthiazol-2-yl-2,5-diphenyltetrazolium bromide (MTT) cell viability assay kit was purchased from Biotium. Dimethyl sulfoxide (DMSO) was purchased from Fisher Scientific. PBS (1X, pH 7.4)

containing NaCl (137 mM), KCl (2.7 mM), Na_2HPO_4 (10 mM), KH_2PO_4 (1.8 mM) was prepared in the lab.

7.2.2 Conjugation of FTIC to TNF-α

Lyophilized recombinant TNF-α was reconstituted in deionized water at 20 μg/mL. FITC was dissolved in sodium carbonate buffer (0.1 M, pH 9.0) at 1 mg/mL. Then, 0.1 mL of FITC solution was mixed with 0.1 mL of TNF-α solution, followed by incubation at room temperature for 2 hr. To this mixture, 0.3 mL of PBS (pH 7.4) was added, and the final solution was dialyzed in PBS to remove unreacted FITC, using a dialysis membrane with 6-8000 molecular weight cut-off. The dialyzed solution was applied to SDS-PAGE, and conjugation was confirmed by fluorescence imaging of SDS-PAGE gels using a fluorescence/phospho-imager (Typhoon, GE Healthcare Life Sciences). Concentration of FITC-TNF was calculated from dilution and volume changes during dialysis.

7.2.3 Enzymatic Activity Assay

FITC-conjugated TNF-α was incubated with the fusion protein $pRgpA_{CAT}–Z_E$, and recovery of quenched fluorescence of FITC was measured. In a 96-well plate, 60 μL of RPMI-1640 medium supplemented with 2% FBS was added and incubated for 30 min at room temperature. Next, 10 μL of FITC-conjugated TNF-α was added to the prepared medium in the 96-well plate. Upon addition of 10 μL of $pRgpA_{CAT}–Z_E$ solutions, fluorescence was immediately measured, using a microplate reader (Synergy HT Multi-Mode, BioTeck). After 30 min of incubation at 37 °C, measurement of fluorescence was repeated. Difference of the fluorescence intensities measured at 0 min and 30 min was calculated to assess the activity of $pRgpA_{CAT}–Z_E$. Concentration of TNF-α in all of the

measured samples was 29.4 nM while concentration of $pRgpA_{CAT}–Z_E$ was adjusted to 0, 2.94, and 29.4 nM.

7.2.4 Immobilization of $pRgpA_{CAT}–Z_E$ and TNF-α Digestion Reaction

The hybrid supraparticles was first prepared as described in Chapter 6. Then, 12 µL $pRgpA_{CAT}–Z_E$ (0.21 µM or 2.1 µM) was added to 8 µL of supraparticle solutions. After 1 hr incubation at room temperature, the supernatant was removed and supraparticles were washed with PBS and diluted in 100 µL of RPMI-1640 medium supplemented with 2% FBS. Solutions containing soluble $pRgpA_{CAT}–Z_E$ were also prepared at concentrations of 25 and 250 nM, by diluting a stock solution (550 µg/mL). Concentration of the stock solution was determined using absorbance at 280 nm (extinction coefficient: 70250 $cm^{-1}M^{-1}$). Next, 20 µL of solutions containing either soluble or immobilized $pRgpA_{CAT}–Z_E$ were added to 80 µL of TNF-α (62.5 nM) solutions prepared in the medium. For controls (0 nM enzyme), same volumes of PBS and a solution of supraparticles with no immobilized enzymes were incubated. The concentration of TNF-α in the reaction mixtures was 50 nM, and the final concentrations of both soluble and immobilized $pRgpA_{CAT}–Z_E$ were varied at 0, 5, and 50 nM. The reaction mixtures were incubated for 1 hr at 37°C and samples were taken, diluted in the medium, and transferred to the following TNF-α inactivation potency assay.

7.2.5 TNF-α Inactivation Potency Assay

Inactivation of TNF-α by both soluble and immobilized $pRgpA_{CAT}–Z_E$ was measured using L929 bioassay.[158,159] Murine L929 cells were cultured in RPMI-1640 medium supplemented with 10% FBS. After resuspending in medium supplemented with 2% FBS, the cells were seeded at 5 X 10^5 cells/well in a 96-well plate for 16 hrs.

Digested reaction mixtures (equivalent to 10 ng/mL of active TNF-α) and actinomycin D (1 μg/mL) were added to the cells (200 μL). After 24 hrs, 10 μL of MTT solutions were added to each well and incubated for 4 hrs at 37°C. From each well, 110 μL medium was carefully removed and 200 μL of DMSO was directly added. To dissolve formazan salt, the medium in each well was well-mixed using pipettes. Absorbance at 570 nm was measured using a microplate reader, and absorbance at 630 nm was also measured for background. To measure cytotoxicity of soluble $pRgpA_{CAT}–Z_E$, the enzymes (0, 2.5, 12.5 nM) and TNF-α (0 or 10 ng/mL) were dosed to L929 cells (5 X 10^5 cells/well). After incubation for 24 hrs, cell viability was measured using MTT assay.

7.3 Results and Discussion

7.3.1 Proteolysis of TNF-α

As described in Chapter 2, the catalytic domain of RgpA ($RgpA_{CAT}$), propeptide domain, and leucine zipper Z_E were combined into a fusion protein $pRgpA_{CAT}–Z_E$. To assess proteolytic activity toward TNF-α, we developed a bioassay based on homo-quenching of fluorescence.[160,161] Upon proteolytic cleavage of fluorescein-labeled substrates, quenched fluorescence is recovered by separation of the cleaved fragments. In this assay, we measured change of fluorescence intensity during proteolytic degradation of FITC-conjugated TNF-α. Recombinant TNF-α was covalently coupled to FITC to result in FITC-TNF-α (Figure 7.1A). Although degradation of TNF-α by wild type gingipains has been analyzed by immunoblotting,[64] the method can only show reduction in the level of TNF-α, which is not clear proof of degradation. In our method, an increase in the fluorescence from the substrate FITC-TNF-α can occur when the homo-quenching is reduced. Thus, such a recovery of quenched fluorescence can be a direct evidence of proteolytic degradation of TNF-α by $pRgpA_{CAT}–Z_E$. During incubation with

pRgpA$_{CAT}$–Z$_E$, FITC-TNF-α exhibited an increase of fluorescence, while the control sample incubated with no enzymes showed a slight decrease (Figure 7.1B). The increased fluorescence was dependent on the concentration of pRgpA$_{CAT}$–Z$_E$, indicating that the rate of proteolytic degradation of FITC-TNF-α was varied by concentration of the enzyme.

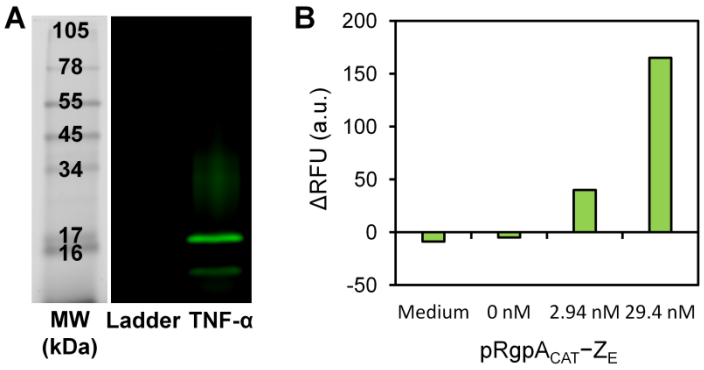

Figure 7.1 Proteolytic activity of pRgpA$_{CAT}$–Z$_E$ to TNF-α. (A) SDS-PAGE gel image of FITC-conjugated TNF-α. (B) Differences of fluorescence intensity measured at 0 min and 30 min (excitation: 495/9.0 nm, emission: 519/9.0 nm): FITC-TNF-α was incubated with no enzymes or 2.94 and 29.4 nM of soluble pRgpA$_{CAT}$–Z$_E$. A medium containing FITC-TNF-α was also tested as a control.

7.3.2 Inactivation of TNF-α

We investigated whether biological activity of TNF-α is reduced by proteolytic degradation, using the TNF-sensitive L929 cells.[158] In this step, we compared the results from both soluble and immobilized $pRgpA_{CAT}–Z_E$ to study effect of enzyme immobilization. The hybrid porous supraparticles can specifically conjugate $pRgpA_{CAT}–Z_E$ through the affinity between Z_E/Z_R coiled coils (Figure 7.2A). When the cells were treated with TNF-α that was digested with immobilized enzymes, 10 ~ 15% survival of L929 cells was observed (Figure 7.2B). In contrast, digestion of TNF-α with soluble enzymes only induced less than 2% of survival of the cells. We note that, when the amount of dosed TNF-α ranges from 0.1 to 10 ng/mL, 10% increase in viability of L929 cells corresponds to more than 90% reduction in the amount of TNF-α, according to the curve of TNF-α concentration and L929 cell viability (Figure 7.2C).

The higher inactivation of TNF-α by immobilized $pRgpA_{CAT}–Z_E$ is promising, but the factors that contributed to enhanced inactivation were not clear. Moreover, the low inactivation rate of soluble enzymes (< 2%) might contradict the results from proteolysis of FITC-TNF-α. To answer these questions, we tested cytotoxicity of $pRgpA_{CAT}–Z_E$, which could also affect the cell viability. Both in the absence and presence of TNF-α (10 ng/mL), incubation of L929 cells with soluble $pRgpA_{CAT}–Z_E$ resulted in concentration-dependent decreases in the viability up to 9 % (Figure 7.2D), and a similar trend was also observed in the presence of 1 ng/mL TNF-α. Thus, immobilization of $pRgpA_{CAT}–Z_E$ and reduced access to cells compared to soluble $pRgpA_{CAT}–Z_E$ might have reduced undesired influence on cells, such as cytotoxicity. Soluble $pRgpA_{CAT}–Z_E$ might be involved in proteolysis of cellular components, possibly cell-surface receptors.[156] Nonetheless, it is also possible that activity or stability of $pRgpA_{CAT}–Z_E$ might be improved by immobilization.

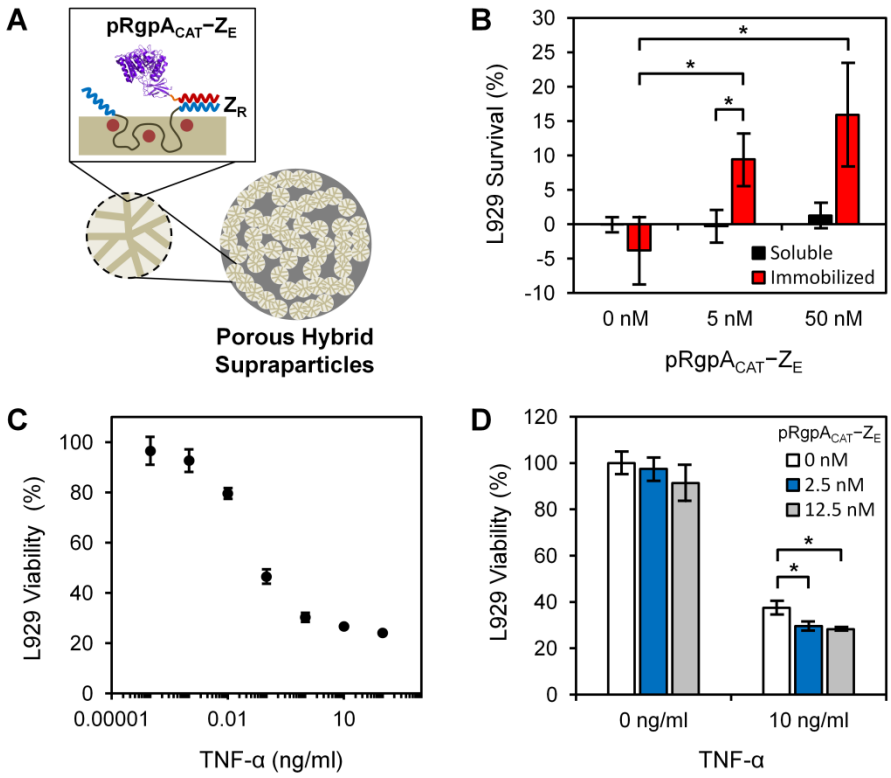

Figure 7.2 Inactivation of TNF-α by soluble and immobilized pRgpA$_{CAT}$–Z$_E$. (A) Scheme for immobilization pRgpA$_{CAT}$–Z$_E$ on the porous supraparticles: Z$_E$ motif from the fusion protein form coiled coils with Z$_R$ motifs incorporated in the particle. (B) Survival of L929 cells treated with TNF-α digestion reaction mixture: absorbance from treatments with 0 and 10 ng/mL of TNF-α was used as references for 100% and 0%, respectively. No soluble enzyme or supraparticles without immobilized enzyme were used as controls (0 nM). (C) A curve of L929 cell viability as a function of TNF-α concentration. (D) Cytotoxicity of soluble pRgpA$_{CAT}$–Z$_E$ in the absence or presence of TNF-α (10 ng/mL). *$P \leq 0.05$. Error bars represent the standard deviation ($n = 3$).

7.4 Conclusion

We demonstrated proteolysis and inactivation of TNF-α by pRgpA$_{CAT}$–Z$_E$. While soluble enzymes showed limited inactivation of TNF-α and a level of cytotoxicity to cells was observed, the enzymes immobilized on porous supraparticles showed enhanced inactivation of TNF-α. This suggests that immobilized pRgpA$_{CAT}$–Z$_E$ may be selective to soluble targets. Moreover, we believe that the supraparticles can be used as a carrier for local delivery of pRgpA$_{CAT}$–Z$_E$ to diseased sites.

CHAPTER 8

CONCLUSIONS AND FUTURE OUTLOOK

8.1 Conclusions and Recommendations

This dissertation describes self-assembly of protein-based suprastructures, which can incorporate folded functional proteins. Recombinant protein building blocks based on biomimetic motifs have been successfully produced, and self-assembled into colloidal suprastructures with various morphologies including spheres, vesicles, nanosheets, and porous particles. Manipulation of morphology was achieved by engineering of protein building blocks, controls in self-assembly processes, and combination of inorganic nanocrystals. The modular design that allows integration of diverse functional domains offers opportunities for practical applications. Moreover, we describe fundamentals involved in self-assembly, including supramolecular interactions, molecular packing, and interparticle interactions. We envision that they will establish a solid basis for further development of self-assembled protein-based biomaterials, contributing to broadening knowledge in this field.

8.1.1 Protein Self-Assembly in the ECM

Fabrication of spherical protein coacervates inside the ECM can be achieved via designed *in-situ* protein self-assembly. It is mediated by spontaneous diffusion–coacervation and high-affinity binding processes. As protein building blocks self-assemble into particles via thermally driven inverse phase transition in the ECM, they are entrapped, and subsequently shrink, and release protein. The main feature of this system is application of the reaction-diffusion principles for protein self-assembly. Molecular transport and simultaneous self-assembly are considered together. Furthermore, the

protein coacervates are kinetically stabilized rather than thermodynamically, while influenced by several competing factors such as the ouzo effect, hindrance by the matrix, and dissociation. For future study, dynamic control of protein self-assembly and their functionalities in different biological matrices can be investigated. As performed in this study, computational modeling can provide anticipation of their distribution in matrices. Also, the system provides potential as a "carrier-free" protein delivery approach. Delivery systems with no carrier materials have newly emerged, and, for example, engineered growth factors with binding affinities to the ECM have been demonstrated.[162] Our approach will contribute to development of further strategies in this field.

8.1.2 Thermally Triggered Self-Assembly of Protein Vesicles

We developed a versatile method for aqueous self-assembly of vesicles from folded proteins. It is driven by thermally triggered inverse phase transition, without any use of organic solvents. Folded and biologically functional proteins can be incorporated into vesicle membranes, and the protein vesicles can encapsulate various types of cargo including small molecules, proteins, and nanoparticles. These interesting properties of the protein vesicles are hypothesized to largely attribute to the "single-layer" vesicular membrane. Acquisition of direct evidences for formation of a single-layer membrane is highly recommended for future work. Also, in-depth investigation of the formation mechanism will be interesting and have an impact to the community of self-assembled materials.

In addition, stability of the vesicles is important for further applications. As described in Chapter 4, vesicles are considered as thermodynamically stable rather than kinetically trapped. As a step forward, assessment of their stability in biological fluids is recommended. Conditions including the presence of serum proteins or at body temperature will provide information about applicability of the vesicles.

8.1.3 Self-Assembly of Protein Nanosheets

Self-assembly of 2D nanosheets can be achieved under controlled processes, using recombinant protein building blocks. Drying-induced self-assembly results in formation of large protein sheets (> 180 μm in width), where and folded functional protein domains can be incorporated. For future study, further investigations on formation mechanism, molecular packing, and their mechanical properties are recommended. Especially, molecular packing is critical for prediction of thermodynamic stability. We hypothesize that lateral assembly of the protein building blocks, which is mediated by hydrophobic interactions, is thermodynamically favored, and this can be further confirmed by direct proofs about molecular packing. Also, effect of modification of the sequence of C_{10} on self-assembling behavior would be a next topic.

Fabrication of protein nanosheets remains underdeveloped. As discussed, only few examples of 2D peptide or peptoid assemblies have been demonstrated. Our approach using folded proteins is a new concept, and formation of large sheets is a promising result. Our rationale on protein design and self-assembly process will provide a new direction for development of strategies for fabrication of protein or peptide nanosheets.

8.1.4 Hierarchically Structured Porous Supraparticles

We developed a simple method to fabricate hierarchically structured porous protein-inorganic hybrid supraparticles. The porous hybrid particles with complex morphology are prepared by interfacial assembly of self-clustering flower-shaped nanoparticles. Such hierarchical assembly of clustering nanoparticles into supraparticles has not been demonstrated,[163] while the developed method is technically simple. Thus, our approach can offer a new opportunity in fabrication of complex super-colloidal structures. It is hypothesized that the interlocking interactions and interfacial assembly

result in kinetically trapped structures. The discrepancy of structural densities at the rim and center of supraparticles supports this hypothesis to some extent. For future work, further investigation on the role of kinetic and thermodynamic parameters is recommended, and it will strengthen the hypothesis. Also, control of supraparticles geometry into, for example, rods or fibers might be achieved by manipulation of the clustering behavior of the flower-shaped nanoparticles.

The incorporated protein $Z_R{-}C_{10}{-}Z_R$ provides high-affinity binding sites for protein immobilization. In this study, a potential protein therapeutic, $pRgpA_{CAT}{-}Z_E$, was immobilized in the supraparticles, and showed enhanced inactivation of TNF-α. The supraparticles could be used as a carrier for local delivery of $pRgpA_{CAT}{-}Z_E$ to diseased sites. Applications can also include biocatalysis, biosensors, and protein delivery. For enzyme immobilization, stabilization and activity enhancement have not been assessed yet, which is recommended as a future work.

8.2 Guidelines for Future Applications

The developed suprastructures provides a promising potential for practical applications. The modular design strategy enables combination of diverse biological functions and controlled physical properties, for a wide spectrum of applications. Fabrication of the suprastructures is technically simple, and they are created as general platforms for use of diverse therapeutic proteins. Compared to conventional methods that involve use of polymeric or inorganic carrier materials, the self-assembled suprastructures enables specific and physical incorporation of therapeutic proteins under biocompatible conditions. Nonetheless, application requires design and production of therapeutic fusion proteins, alterations in self-assembly processes, and specific methods for administration. In this regard, several important factors must be considered, which

include (1) choice of protein; (2) choice of suprastructure; (3) self-assembly protocols; (4) administration routes.

8.2.1 Choice of Protein

First, a protein therapeutic can be chosen, based on desired biological functions. Types of protein therapeutics can include: antibodies, anticoagulant, blood factors, enzymes, growth factors, hormones, cytokines, and thrombolytics.[164] In addition to biological activity, a critical criterion in choice of protein is whether a therapeutic protein can be successfully expressed, folded, and purified when it is fused with leucine zipper motif Z_E. Fusion of Z_E to folded proteins has been successful for various proteins: fluorescent proteins (mCherry, GFP,[50] EGFP), biomotors (kinesin-1[52]), enzymes (Rgp, GST[50]), cell-adhesive proteins (fibronectin[51]), and growth factors (FGF4). Both N and C terminal fusion of Z_E are possible in general, although position of active sites should be considered. Also, such proteins that exhibit activities as dimers or trimers might be less suitable since tethered Z_E might prevent their formation.

8.2.2 Choice of Suprastructure and Self-Assembly Protocols

Spherical protein coacervates, which can form in the ECM, are useful for application of protein therapeutics working in the extracellular environments. Growth factors, enzymes, or antibodies can be included, and proteins become present as either self-assembled particles or dissociated forms. Depending on solubility of therapeutic proteins, the concentration of dosed Z_R–ELP needs to be adjusted for their incorporation into Z_R–ELP coacervates. Once self-assembled coacervates form in the ECM, approximately 50% release of therapeutic proteins is anticipated during first 24 hr,

followed by long-term retention as self-assembled particles. Dissociation rates may differ depending on physical properties of the incorporated proteins, such as surface charge or hydrodynamic diameter.

Protein vesicles can be used as carriers for delivery of various types of cargo including small molecules, proteins, and nanoparticles. For encapsulation of cargo, we expect that hydrophobic interactions between cargo and ELP motifs are critical. Thus, alterations of ionic strength or use of additives may be necessary, depending of surface properties of encapsulated cargo. Therapeutic proteins can also be incorporated on vesicular membrane. Ionic strength should be altered since vesicle formation is strongly affected by the hydrodynamic diameter and surface properties of the therapeutic proteins. In general, high salt concentration (~ 1 M) is required for proteins with small effective head area.

One potential application of protein nanosheets is for cell delivery. The nanosheets can enable incorporation of a set of multiple proteins required for cell growth, including cell-adhesion proteins, growth factors, and affinity ligands. In assembly of those proteins into nanosheets, there is still lack of information about incorporation efficiency as a function of protein concentration. Thus, optimization of this process should be first completed to control biological functionality of the nanosheets. Cells can simply be deposited on the surface, and the sheets are sufficiently flexible for formulation of cell aggregates.[165] However, influences of surface chemistry and mechanical properties of the nanosheets on growth of cells should be investigated prior to applications.

Lastly, the hybrid porous supraparticles are useful for application of proteins that interact with soluble targets. For example, enzymes can be immobilized and biocatalysis can be conducted inside the particles. The pores are accessible to even large macromolecular substrates, as the hierarchy of porous structures is beneficial for efficient mass transport of substrates through the particles. Antibodies or affinity ligands can also be incorporated and used for modulation of biological responses, for example, by

sequestration of cytokines or chemokines. Immobilization of proteins can be achieved by 1 hr incubation in aqueous solution, while compositions of solution may need to altered, depending on requirements for protein activity.

8.2.3 Administration Routes

Although the developed suprastructures are created from biocompatible and inert components, information on their fate *in vivo* should be first obtained for administration. For example, consequences from administration of the porous protein-calcium phosphate hybrid supraparticles may limit their use to only specific applications such as bone regeneration.[166,167] To select an administration route, evaluations of biocompatibility, toxicity, and tolerance in various routes should be conducted. In general, micrometer-scale structures are not suitable for intravascular administration.[24] The suprastructures are at micrometer scale, and injections to local sites or topical applications to open tissues such as wounds are considered suitable for administration. Oral administration may be possible for protein vesicles or nanosheets although characterizations on their stabilization effect and biocompatibility should be first confirmed under simulated *in vivo* conditions.

APPENDIX A

PROTEIN SEQUENCES

Name	Sequence
Z_R–ELP	MKGSLEIRAAALRRRNTALRTRVAELRQRVQRLRNEVSQYETRYGPL$(G_4S)_2$ G$[(VPGVG)_2VPGFG(VPGVG)_2]_5$VPGC
Z_R–C_{10}–Z_R	MGLEIRAAALRRRNTALRTRVAELRQRVQRLRNEVSQYETRYGPLKLRDWM G$[(AG)_3PEG]_{10}$ALMPVDLEIRAAALRRRNTALRTRVAELRQRVQRLRNEVSQ YETRYGPLR
mCherry–Z_E	MGGSRSMVSKGEEDNMAIIKEFMRFKVHMEGSVNGHEFEIEGEGEGRPYE GTQTAKLKVTKGGPLPFAWDILSPQFMYGSKAYVKHPADIPDYLKLSFPEGF KWERVMNFEDGGVVTVTQDSSLQDGEFIYKVKLRGTNFPSDGPVMQKKT MGWEASSERMYPEDGALKGEIKQRLKLKDGGHYDAEVKTTYKAKKPVQLP GAYNVNIKLDITSHNEDYTIVEQYERAEGRHSTGGMDELYKSKLRGSGSLEIE AAALEQENTALETEVAELEQEVQRLENIVSQYRTRYGPLRSHHHHHH
EGFP–Z_E	MGGSRSMASKGEELFTGVVPILVELDGDVNGHKFSVSGEGEGDATYGKLTL KFICTTGKLPVPWPTLVTTLCYGVQCFSRYPDHMKRHDFFKSAMPEGYVQE RTIFFKDDGNYKTRAEVKFEGDTLVNRIELKGIDFKEDGNILGHKLEYNYNSH NVYIMADKQKNGIKVNFKTRHNIEDGSVQLADHYQQNTPIGDGPVLLPDN HYLSTQSALSKDPNEKRDHMVLLEFVTAAGITHGMDELYNLRGSGSLEIEAA ALEQENTALETEVAELEQEVQRLENIVSQYRTRYGPLRSHHHHHH
pRgpA$_{CAT}$–Z_E	MGQQTELGRNPNVRLLESTQQSVTKVQFRMDNLKFTEVQTPKGMAQVPT YTEGVNLSEKGMPTLPILSRSLAVSDTREMKVEVVSSKFIEKKNVLIAPSKGMI MRNEDPKKIPYVYGKSYSQNKFFPGEIATLDDPFILRDVRGQVVNFAPLQYN PVTKTLRIYTEITVAVSETSEQGKNILNKKGTFAGFEDTYKRMFMNYEPGRYT PVEEKQNGRMIVIVAKKYEGDIKDFVDWKNQRGLRTEVKVAEDIASPVTAN AIQQFVKQEYEKEGNDLTYVLLIGDHKDIPAKITPGIKSDQVYGQIVGNDHYN EVFIGRFSCESKEDLKTQIDRTIHYERNITTEDKWLGQALCIASAEGGPSADNG ESDIQHENVIANLLTQYGYTKIIKCYDPGVTPKNIIDAFNGGISLVNYTGHGSE TAWGTSHFGTTHVKQLTNSNQLPFIFDVACVNGDFLFSMPCFAEALMRAQ KDGKPTGTVAIIASTINQSWASPMRGQDEMNEILCEKHPNNIKRTFGGVTM NGMFAMVEKYKKDGEKMLDTWTVFGDPSLLVRTLVPTKMQVTAPAQINL TDASVNVSCDYNGAIATISANGKMFGSAVVENGTATINLTGLTNESTLTLTV VGYNKETVIKTINTNGEPNPYQPVSNLTATTQGQKVTLKWDAPSTKTNATT NTARSVDGIREMVLLSVSDAPELLRGSGSLEIEAAALEQENTALETEVAELEQ EVQRLENIVSQYRTRYGPLRSHHHHHH

*The protein domains and motifs are colored: Z_R (blue), Z_E (red), ELP (gray), ELP (brown), mCherry (pink), EGFP (green), pRgpA$_{CAT}$ (purple).

APPENDIX B

PLASMID MAPS AND DNA SEQUENCES

B.1 pQE60-His6ZE_Z_R-C_{10}−Z_R

Plasmid Map

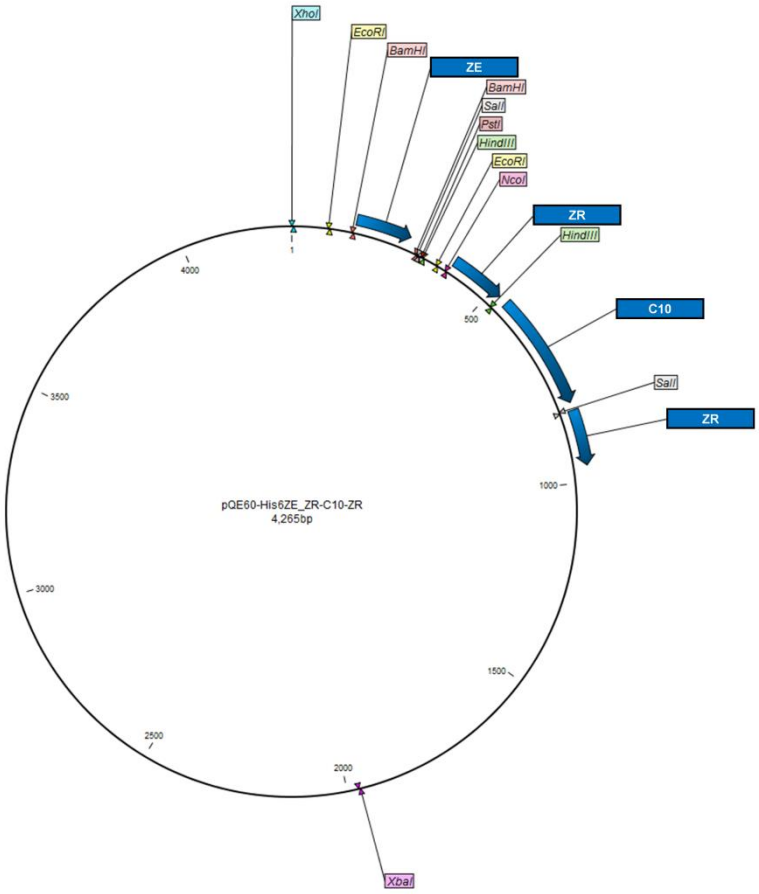

DNA Sequence

CTCGAGAAATCATAAAAAATTTATTTGCTTTGTGAGCGGATAACAATTATAATAGATTCAATT
GTGAGCGGATAACAATTTCACACAGAATTCATTAAAGAGGAGAAATTAACTATGAGAGGATC
GCATCACCATCACCATCACGGATCCCTGGAAATCGAAGCGGCGGCGCTGGAACAGGAAAACA
CCGCGCTGGAAACCGAAGTTGCGGAACTGGAACAGGAAGTTCAGCGTCTGGAAAACATCGTT
TCTCAGTACCGTACCCGTTACGGTCCGCTGGGTGGTGGTTTCTTCTTCCCGTAAGGATCCGTCG
ACCTGCAGCCAAGCTTAATTAGCTGAGCCGGATAACAATTTCACACAGAATTCATTAAAGAGG
AGAAATTAACCATGGGTCTGGAAATCCGTGCGGCGGCGCTGCGTCGTCGTAACACCGCGCTGC

GTACCCGTGTTGCGGAACTGCGTCAGCGTGTTCAGCGTCTGCGTAACGAAGTTTCTCAGTACG
AAACCCGTTACGGTCCGCTGAAGCTTCGCGATTGGATGGGTGCCGGCGCTGGTGCGGGCCCGG
AAGGTGCAGGCGCTGGTGCGGGCCCGGAAGGTGCCGGCGCTGGTGCGGGCCCGGAAGGTGCA
GGCGCTGGTGCGGGCCCGGAAGGTGCCGGCGCTGGTGCGGGCCCGGAAGGTGCAGGCGCTGG
TGCGGGCCCGGAAGGTGCCGGCGCTGGTGCGGGCCCGGAAGGTGCAGGCGCTGGTGCGGGCC
CGGAAGGTGCCGGCGCTGGTGCGGGCCCGGAAGGTGCAGGCGCTGGTGCGGGCCCGGAAGGT
GCCCTCATGCCGGTCGACCTGGAAATCCGTGCGGCGGCGCTGCGTCGTCGTAACACCGCGCTG
CGTACCCGTGTTGCGGAACTGCGTCAGCGTGTTCAGCGTCTGCGTAACGAAGTTTCTCAGTAC
GAAACCCGTTACGGTCCGCTGAGATAACATCACCATCACCATCACTAACCTTAATTAGCTGAG
CTTGGACTCCTGTTGATAGATCCAGTAATGACCTCAGAACTCCATCTGGATTTGTTCAGAACG
CTCGGTTGCCGCCGGGCGTTTTTTATTGGTGAGAATCCAAGCTAGCTTGGCGAGATTTTCAGG
AGCTAAGGAAGCTAAAATGGAGAAAAAAATCACTGGATATACCACCGTTGATATATCCCAAT
GGCATCGTAAAGAACATTTTGAGGCATTTCAGTCAGTTGCTCAATGTACCTATAACCAGACCG
TTCAGCTGGATATTACGGCCTTTTTAAAGACCGTAAAGAAAAATAAGCACAAGTTTTATCCGG
CCTTTATTCACATTCTTGCCCGCCTGATGAATGCTCATCCGGAATTTCGTATGGCAATGAAAGA
CGGTGAGCTGGTGATATGGGATAGTGTTCACCCTTGTTACACCGTTTTCCATGAGCAAACTGA
AACGTTTTCATCGCTCTGGAGTGAATACCACGACGATTTCCGGCAGTTTCTACACATATATTCG
CAAGATGTGGCGTGTTACGGTGAAAACCTGGCCTATTTCCCTAAAGGGTTTATTGAGAATATG
TTTTTCGTCTCAGCCAATCCCTGGGTGAGTTTCACCAGTTTTGATTTAAACGTGGCCAATATGG
ACAACTTCTTCGCCCCCGTTTTCACCATGCATGGGCAAATATTATACGCAAGGCGACAAGGTG
CTGATGCCGCTGGCGATTCAGGTTCATCATGCCGTCTGTGATGGCTTCCATGTCGGCAGAATG
CTTAATGAATTACAACAGTACTGCGATGAGTGGCAGGGCGGGGCGTAATTTTTTTAAGGCAGT
TATTGGTGCCCTTAAACGCCTGGGGTAATGACTCTCTAGCTTGAGGCATCAAATAAAACGAAA
GGCTCAGTCGAAAGACTGGGCCTTTCGTTTTATCTGTTGTTTGTCGGTGAACGCTCTCCTGAGT
AGGACAAATCCGCCGCTCTAGAGCTGCCTCGCGCGTTTCGGTGATGACGGTGAAAACCTCTGA
CACATGCAGCTCCCGGAGACGGTCACAGCTTGTCTGTAAGCGGATGCCGGGAGCAGACAAGC
CCGTCAGGGCGCGTCAGCGGGTGTTGGCGGGTGTCGGGGCGCAGCCATGACCCAGTCACGTA
GCGATAGCGGAGTGTATACTGGCTTAACTATGCGGCATCAGAGCAGATTGTACTGAGAGTGC
ACCATATGCGGTGTGAAATACCGCACAGATGCGTAAGGAGAAAATACCGCATCAGGCGCTCT
TCCGCTTCCTCGCTCACTGACTCGCTGCGCTCGGTCGTTCGGCTGCGGCGAGCGGTATCAGCTC
ACTCAAAGGCGGTAATACGGTTATCCACAGAATCAGGGGATAACGCAGGAAAGAACATGTGA
GCAAAAGGCCAGCAAAAGGCCAGGAACCGTAAAAAGGCCGCGTTGCTGGCGTTTTTCCATAG
GCTCCGCCCCCCTGACGAGCATCACAAAAATCGACGCTCAAGTCAGAGGTGGCGAAACCCGA
CAGGACTATAAAGATACCAGGCGTTTCCCCCTGGAAGCTCCCTCGTGCGCTCTCCTGTTCCGA
CCCTGCCGCTTACCGGATACCTGTCCGCCTTTCTCCCTTCGGGAAGCGTGGCGCTTTCTCATAG
CTCACGCTGTAGGTATCTCAGTTCGGTGTAGGTCGTTCGCTCCAAGCTGGGCTGTGTGCACGA
ACCCCCCGTTCAGCCCGACCGCTGCGCCTTATCCGGTAACTATCGTCTTGAGTCCAACCCGGT
AAGACACGACTTATCGCCACTGGCAGCAGCCACTGGTAACAGGATTAGCAGAGCGAGGTATG
TAGGCGGTGCTACAGAGTTCTTGAAGTGGTGGCCTAACTACGGCTACACTAGAAGGACAGTAT
TTGGTATCTGCGCTCTGCTGAAGCCAGTTACCTTCGGAAAAAGAGTTGGTAGCTCTTGATCCG
GCAAACAAACCACCGCTGGTAGCGGTGGTTTTTTTGTTTGCAAGCAGCAGATTACGCGCAGAA
AAAAAGGATCTCAAGAAGATCCTTTGATCTTTTCTACGGGGTCTGACGCTCAGTGGAACGAAA
ACTCACGTTAAGGGATTTTGGTCATGAGATTATCAAAAAGGATCTTCACCTAGATCCTTTTAA
ATTAAAAATGAAGTTTTAAATCAATCTAAAGTATATATGAGTAAACTTGGTCTGACAGTTACC
AATGCTTAATCAGTGAGGCACCTATCTCAGCGATCTGTCTATTTCGTTCATCCATAGTTGCCTG
ACTCCCCGTCGTGTAGATAACTACGATACGGGAGGGCTTACCATCTGGCCCCAGTGCTGCAAT
GATACCGCGAGACCCACGCTCACCGGCTCCAGATTTATCAGCAATAAACCAGCCAGCCGGAA
GGGCCGAGCGCAGAAGTGGTCCTGCAACTTTATCCGCCTCCATCCAGTCTATTAATTGTTGCC
GGGAAGCTAGAGTAAGTAGTTCGCCAGTTAATAGTTTGCGCAACGTTGTTGCCATTGCTACAG
GCATCGTGGTGTCACGCTCGTCGTTTGGTATGGCTTCATTCAGCTCCGGTTCCCAACGATCAAG
GCGAGTTACATGATCCCCCATGTTGTGCAAAAAAGCGGTTAGCTCCTTCGGTCCTCCGATCGT
TGTCAGAAGTAAGTTGGCCGCAGTGTTATCACTCATGGTTATGGCAGCACTGCATAATTCTCTT
ACTGTCATGCCATCCGTAAGATGCTTTTCTGTGACTGGTGAGTACTCAACCAAGTCATTCTGAG
AATAGTGTATGCGGCGACCGAGTTGCTCTTGCCCGGCGTCAATACGGGATAATACCGCGCCAC
ATAGCAGAACTTTAAAAGTGCTCATCATTGGAAAACGTTCTTCGGGGCGAAAACTCTCAAGGA
TCTTACCGCTGTTGAGATCCAGTTCGATGTAACCCACTCGTGCACCCAACTGATCTTCAGCATC

TTTTACTTTCACCAGCGTTTCTGGGTGAGCAAAAACAGGAAGGCAAAATGCCGCAAAAAAGG
GAATAAGGGCGACACGGAAATGTTGAATACTCATACTCTTCCTTTTTCAATATTATTGAAGCA
TTTATCAGGGTTATTGTCTCATGAGCGGATACATATTTGAATGTATTTAGAAAAATAAACAAA
TAGGGGTTCCGCGCACATTTCCCCGAAAAGTGCCACCTGACGTCTAAGAAACCATTATTATCA
TGACATTAACCTATAAAAATAGGCGTATCACGAGGCCCTTTCGTCTTCAC

B.2 pQE60-mCherry−Z_E

Plasmid Map

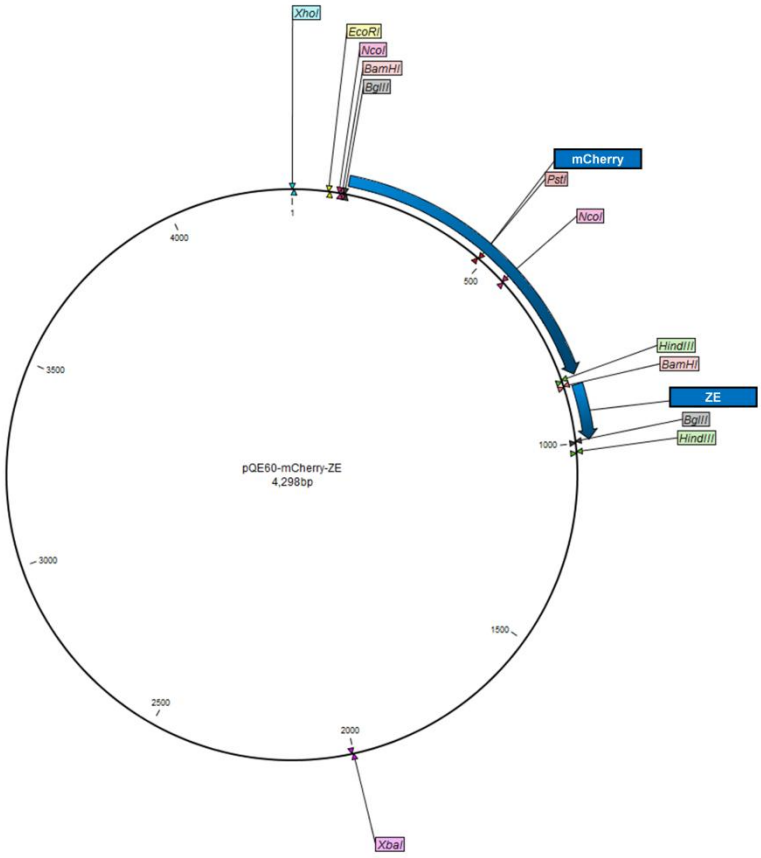

DNA Sequence

CTCGAGAAATCATAAAAAATTTATTTGCTTTGTGAGCGGATAACAATTATAATAGATTCAATT
GTGAGCGGATAACAATTTCACACAGAATTCATTAAAGAGGAGAAATTAACCATGGGAGGATC
CAGATCTATGGTGAGCAAGGGCGAGGAGGATAACATGGCCATCATCAAGGAGTTCATGCGCT
TCAAGGTGCACATGGAGGGCTCCGTGAACGGCCACGAGTTCGAGATCGAGGGCGAGGGCGAG
GGCCGCCCCTACGAGGGCACCCAGACCGCCAAGCTGAAGGTGACCAAGGGTGGCCCCCTGCC
CTTCGCCTGGGACATCCTGTCCCCTCAGTTCATGTACGGCTCCAAGGCCTACGTGAAGCACCC
CGCCGACATCCCCGACTACTTGAAGCTGTCCTTCCCCGAGGGCTTCAAGTGGGAGCGCGTGAT
GAACTTCGAGGACGGCGGCGTGGTGACCGTGACCCAGGACTCCTCCCTGCAGGACGGCGAGT

TCATCTACAAGGTGAAGCTGCGCGGCACCAACTTCCCCTCCGACGGCCCCGTAATGCAGAAGA
AGACCATGGGCTGGGAGGCCTCCTCCGAGCGGATGTACCCCGAGGACGGCGCCCTGAAGGGC
GAGATCAAGCAGAGGCTGAAGCTGAAGGACGGCGGCCACTACGACGCTGAGGTCAAGACCA
CCTACAAGGCCAAGAAGCCCGTGCAGCTGCCCGGCGCCTACAACGTCAACATCAAGTTGGAC
ATCACCTCCCACAACGAGGACTACACCATCGTGGAACAGTACGAACGCGCCGAGGGCCGCCA
CTCCACCGGCGGCATGGACGAGCTGTACAAGTCGAAGCTTCGCGGTAGTGGATCCCTGGAAA
TCGAAGCGGCGGCGCTGGAACAGGAAAACACCGCGCTGGAAACCGAAGTTGCGGAACTGGA
ACAGGAAGTTCAGCGTCTGGAAAACATCGTTTCTCAGTACCGTACCCGTTACGGTCCGCTGAG
ATCTCATCACCATCACCATCACTAAGCTTAATTAGCTGAGCTTGGACTCCTGTTGATAGATCCA
GTAATGACCTCAGAACTCCATCTGGATTTGTTCAGAACGCTCGGTTGCCGCCGGGCGTTTTTTA
TTGGTGAGAATCCAAGCTAGCTTGGCGAGATTTTCAGGAGCTAAGGAAGCTAAAATGGAGAA
AAAAATCACTGGATATACCACCGTTGATATATCCCAATGGCATCGTAAAGAACATTTTGAGGC
ATTTCAGTCAGTTGCTCAATGTACCTATAACCAGACCGTTCAGCTGGATATTACGGCCTTTTTA
AAGACCGTAAAGAAAAATAAGCACAAGTTTTATCCGGCCTTTATTCACATTCTTGCCCGCCTG
ATGAATGCTCATCCGGAATTTCGTATGGCAATGAAAGACGGTGAGCTGGTGATATGGGATAGT
GTTCACCCTTGTTACACCGTTTTCCATGAGCAAACTGAAACGTTTTCATCGCTCTGGAGTGAAT
ACCACGACGATTTCCGGCAGTTTCTACACATATATTCGCAAGATGTGGCGTGTTACGGTGAAA
ACCTGGCCTATTTCCCTAAAGGGTTTATTGAGAATATGTTTTTCGTCTCAGCCAATCCCTGGGT
GAGTTTCACCAGTTTTGATTTAAACGTGGCCAATATGGACAACTTCTTCGCCCCCGTTTTCACC
ATGCATGGGCAAATATTATACGCAAGGCGACAAGGTGCTGATGCCGCTGGCGATTCAGGTTC
ATCATGCCGTCTGTGATGGCTTCCATGTCGGCAGAATGCTTAATGAATTACAACAGTACTGCG
ATGAGTGGCAGGGCGGGGCGTAATTTTTTTAAGGCAGTTATTGGTGCCCTTAAACGCCTGGGG
TAATGACTCTCTAGCTTGAGGCATCAAATAAAACGAAAGGCTCAGTCGAAAGACTGGGCCTTT
CGTTTTATCTGTTGTTTGTCGGTGAACGCTCTCCTGAGTAGGACAAATCCGCCGCTCTAGAGCT
GCCTCGCGCGTTTCGGTGATGACGGTGAAAACCTCTGACACATGCAGCTCCCGGAGACGGTCA
CAGCTTGTCTGTAAGCGGATGCCGGGAGCAGACAAGCCCGTCAGGGCGCGTCAGCGGGTGTT
GGCGGGTGTCGGGGCGCAGCCATGACCCAGTCACGTAGCGATAGCGGAGTGTATACTGGCTT
AACTATGCGGCATCAGAGCAGATTGTACTGAGAGTGCACCATATGCGGTGTGAAATACCGCA
CAGATGCGTAAGGAGAAAATACCGCATCAGGCGCTCTTCCGCTTCCTCGCTCACTGACTCGCT
GCGCTCGGTCGTTCGGCTGCGGCGAGCGGTATCAGCTCACTCAAAGGCGGTAATACGGTTATC
CACAGAATCAGGGGATAACGCAGGAAAGAACATGTGAGCAAAAGGCCAGCAAAAGGCCAGG
AACCGTAAAAAGGCCGCGTTGCTGGCGTTTTTCCATAGGCTCCGCCCCCCTGACGAGCATCAC
AAAAATCGACGCTCAAGTCAGAGGTGGCGAAACCCGACAGGACTATAAAGATACCAGGCGTT
TCCCCCTGGAAGCTCCCTCGTGCGCTCTCCTGTTCCGACCCTGCCGCTTACCGGATACCTGTCC
GCCTTTCTCCCTTCGGGAAGCGTGGCGCTTTCTCATAGCTCACGCTGTAGGTATCTCAGTTCGG
TGTAGGTCGTTCGCTCCAAGCTGGGCTGTGTGCACGAACCCCCCGTTCAGCCCGACCGCTGCG
CCTTATCCGGTAACTATCGTCTTGAGTCCAACCCGGTAAGACACGACTTATCGCCACTGGCAG
CAGCCACTGGTAACAGGATTAGCAGAGCGAGGTATGTAGGCGGTGCTACAGAGTTCTTGAAG
TGGTGGCCTAACTACGGCTACACTAGAAGGACAGTATTTGGTATCTGCGCTCTGCTGAAGCCA
GTTACCTTCGGAAAAAGAGTTGGTAGCTCTTGATCCGGCAAACAAACCACCGCTGGTAGCGGT
GGTTTTTTTGTTTGCAAGCAGCAGATTACGCGCAGAAAAAAAGGATCTCAAGAAGATCCTTTG
ATCTTTTCTACGGGGTCTGACGCTCAGTGGAACGAAAACTCACGTTAAGGGATTTTGGTCATG
AGATTATCAAAAAGGATCTTCACCTAGATCCTTTTAAATTAAAAATGAAGTTTTAAATCAATC
TAAAGTATATATGAGTAAACTTGGTCTGACAGTTACCAATGCTTAATCAGTGAGGCACCTATC
TCAGCGATCTGTCTATTTCGTTCATCCATAGTTGCCTGACTCCCCGTCGTGTAGATAACTACGA
TACGGGAGGGCTTACCATCTGGCCCCAGTGCTGCAATGATACCGCGAGACCCACGCTCACCGG
CTCCAGATTTATCAGCAATAAACCAGCCAGCCGGAAGGGCCGAGCGCAGAAGTGGTCCTGCA
ACTTTATCCGCCTCCATCCAGTCTATTAATTGTTGCCGGGAAGCTAGAGTAAGTAGTTCGCCA
GTTAATAGTTTGCGCAACGTTGTTGCCATTGCTACAGGCATCGTGGTGTCACGCTCGTCGTTTG
GTATGGCTTCATTCAGCTCCGGTTCCCAACGATCAAGGCGAGTTACATGATCCCCCATGTTGT
GCAAAAAAGCGGTTAGCTCCTTCGGTCCTCCGATCGTTGTCAGAAGTAAGTTGGCCGCAGTGT
TATCACTCATGGTTATGGCAGCACTGCATAATTCTCTTACTGTCATGCCATCCGTAAGATGCTT
TTCTGTGACTGGTGAGTACTCAACCAAGTCATTCTGAGAATAGTGTATGCGGCGACCGAGTTG
CTCTTGCCCGGCGTCAATACGGGATAATACCGCGCCACATAGCAGAACTTTAAAAGTGCTCAT
CATTGGAAAACGTTCTTCGGGGCGAAAACTCTCAAGGATCTTACCGCTGTTGAGATCCAGTTC
GATGTAACCCACTCGTGCACCCAACTGATCTTCAGCATCTTTTACTTTCACCAGCGTTTCTGGG

TGAGCAAAAACAGGAAGGCAAAATGCCGCAAAAAAGGGAATAAGGGCGACACGGAAATGTT
GAATACTCATACTCTTCCTTTTTCAATATTATTGAAGCATTTATCAGGGTTATTGTCTCATGAG
CGGATACATATTTGAATGTATTTAGAAAAATAAACAAATAGGGGTTCCGCGCACATTTCCCCG
AAAAGTGCCACCTGACGTCTAAGAAACCATTATTATCATGACATTAACCTATAAAAATAGGCG
TATCACGAGGCCCTTTCGTCTTCAC

B.3 pQE60-EGFP−Z_E

Plasmid Map

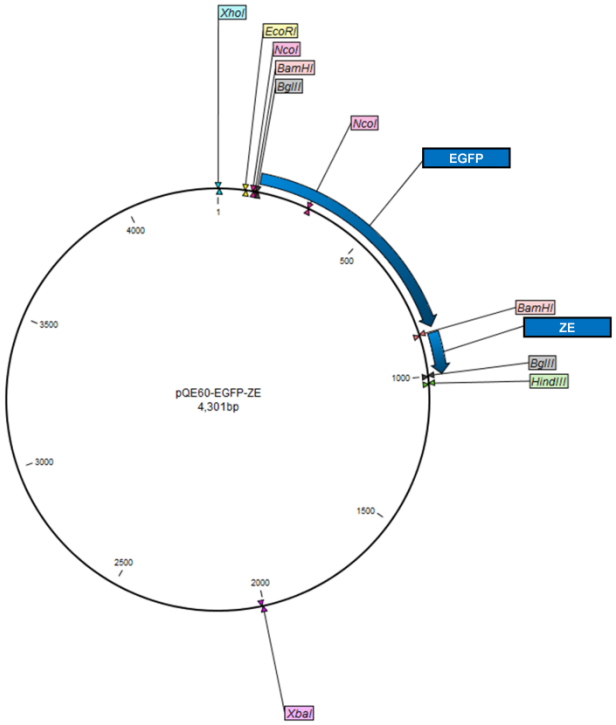

DNA Sequence

CTCGAGAAATCATAAAAAATTTATTTGCTTTGTGAGCGGATAACAATTATAATAGATTCAATT
GTGAGCGGATAACAATTTCACACAGAATTCATTAAAGAGGAGAAATTAACCATGGGAGGATC
CAGATCTATGGCTAGCAAAGGAGAAGAACTCTTCACTGGAGTTGTCCCAATTCTTGTTGAATT
AGATGGTGATGTTAACGGCCACAAGTTCTCTGTCAGTGGAGAGGGTGAAGGTGATGCAACAT
ACGGAAAACTTACCCTGAAGTTCATCTGCACTACTGGCAAACTGCCTGTTCCATGGCCAACAC
TAGTCACTACTCTGTGCTATGGTGTTCAATGCTTTTCAAGATACCCGGATCATATGAAACGGC
ATGACTTTTTCAAGAGTGCCATGCCCGAAGGTTATGTACAGGAAAGGACCATCTTCTTCAAAG
ATGACGGCAACTACAAGACACGTGCTGAAGTCAAGTTTGAAGGTGATACCCTTGTTAATAGA
ATCGAGTTAAAAGGTATTGACTTCAAGGAAGATGGCAACATTCTGGGACACAAATTGGAATA
CAACTATAACTCACACAATGTATACATCATGGCAGACAAACAAAAGAATGGAATCAAAGTGA
ACTTCAAGACCCGCCACAACATTGAAGATGGAAGCGTTCAACTAGCAGACCATTATCAACAA
AATACTCCAATTGGCGATGGCCCTGTCCTTTTACCAGACAACCATTACCTGTCCACACAATCTG

CCCTTTCGAAAGATCCCAACGAAAAGAGAGACCACATGGTCCTTCTTGAGTTTGTAACAGCTG
CTGGGATTACACATGGCATGGATGAACTGTACAATCTTCGCGGTAGTGGATCCCTGGAAATCG
AAGCGGCGGCGCTGGAACAGGAAAACACCGCGCTGGAAACCGAAGTTGCGGAACTGGAACA
GGAAGTTCAGCGTCTGGAAAACATCGTTTCTCAGTACCGTACCCGTTACGGTCCGCTGAGATC
TCATCACCATCACCATCACTAAGCTTAATTAGCTGAGCTTGGACTCCTGTTGATAGATCCAGTA
ATGACCTCAGAACTCCATCTGGATTTGTTCAGAACGCTCGGTTGCCGCCGGGCGTTTTTTATTG
GTGAGAATCCAAGCTAGCTTGGCGAGATTTTCAGGAGCTAAGGAAGCTAAAATGGAGAAAAA
AATCACTGGATATACCACCGTTGATATATCCCAATGGCATCGTAAAGAACATTTTGAGGCATT
TCAGTCAGTTGCTCAATGTACCTATAACCAGACCGTTCAGCTGGATATTACGGCCTTTTTAAAG
ACCGTAAAGAAAAATAAGCACAAGTTTTATCCGGCCTTTATTCACATTCTTGCCCGCCTGATG
AATGCTCATCCGGAATTTCGTATGGCAATGAAAGACGGTGAGCTGGTGATATGGGATAGTGTT
CACCCTTGTTACACCGTTTTCCATGAGCAAACTGAAACGTTTTCATCGCTCTGGAGTGAATACC
ACGACGATTTCCGGCAGTTTCTACACATATATTCGCAAGATGTGGCGTGTTACGGTGAAAACC
TGGCCTATTTCCCTAAAGGGTTTATTGAGAATATGTTTTTCGTCTCAGCCAATCCCTGGGTGAG
TTTCACCAGTTTTGATTTAAACGTGGCCAATATGGACAACTTCTTCGCCCCCGTTTTCACCATG
CATGGGCAAATATTATACGCAAGGCGACAAGGTGCTGATGCCGCTGGCGATTCAGGTTCATCA
TGCCGTCTGTGATGGCTTCCATGTCGGCAGAATGCTTAATGAATTACAACAGTACTGCGATGA
GTGGCAGGGCGGGGCGTAATTTTTTTAAGGCAGTTATTGGTGCCCTTAAACGCCTGGGGTAAT
GACTCTCTAGCTTGAGGCATCAAATAAAACGAAAGGCTCAGTCGAAAGACTGGGCCTTTCGTT
TTATCTGTTGTTTGTCGGTGAACGCTCTCCTGAGTAGGACAAATCCGCCGCTCTAGAGCTGCCT
CGCGCGTTTCGGTGATGACGGTGAAAACCTCTGACACATGCAGCTCCCGGAGACGGTCACAG
CTTGTCTGTAAGCGGATGCCGGGAGCAGACAAGCCCGTCAGGGCGCGTCAGCGGGTGTTGGC
GGGTGTCGGGGCGCAGCCATGACCCAGTCACGTAGCGATAGCGGAGTGTATACTGGCTTAAC
TATGCGGCATCAGAGCAGATTGTACTGAGAGTGCACCATATGCGGTGTGAAATACCGCACAG
ATGCGTAAGGAGAAAATACCGCATCAGGCGCTCTTCCGCTTCCTCGCTCACTGACTCGCTGCG
CTCGGTCGTTCGGCTGCGGCGAGCGGTATCAGCTCACTCAAAGGCGGTAATACGGTTATCCAC
AGAATCAGGGGATAACGCAGGAAAGAACATGTGAGCAAAAGGCCAGCAAAAGGCCAGGAAC
CGTAAAAAGGCCGCGTTGCTGGCGTTTTTCCATAGGCTCCGCCCCCCTGACGAGCATCACAAA
AATCGACGCTCAAGTCAGAGGTGGCGAAACCCGACAGGACTATAAAGATACCAGGCGTTTCC
CCCTGGAAGCTCCCTCGTGCGCTCTCCTGTTCCGACCCTGCCGCTTACCGGATACCTGTCCGCC
TTTCTCCCTTCGGGAAGCGTGGCGCTTTCTCATAGCTCACGCTGTAGGTATCTCAGTTCGGTGT
AGGTCGTTCGCTCCAAGCTGGGCTGTGTGCACGAACCCCCCGTTCAGCCCGACCGCTGCGCCT
TATCCGGTAACTATCGTCTTGAGTCCAACCCGGTAAGACACGACTTATCGCCACTGGCAGCAG
CCACTGGTAACAGGATTAGCAGAGCGAGGTATGTAGGCGGTGCTACAGAGTTCTTGAAGTGG
TGGCCTAACTACGGCTACACTAGAAGGACAGTATTTGGTATCTGCGCTCTGCTGAAGCCAGTT
ACCTTCGGAAAAAGAGTTGGTAGCTCTTGATCCGGCAAACAAACCACCGCTGGTAGCGGTGG
TTTTTTTGTTTGCAAGCAGCAGATTACGCGCAGAAAAAAAGGATCTCAAGAAGATCCTTTGAT
CTTTTCTACGGGGTCTGACGCTCAGTGGAACGAAAACTCACGTTAAGGGATTTTGGTCATGAG
ATTATCAAAAAGGATCTTCACCTAGATCCTTTTAAATTAAAAATGAAGTTTTAAATCAATCTA
AAGTATATATGAGTAAACTTGGTCTGACAGTTACCAATGCTTAATCAGTGAGGCACCTATCTC
AGCGATCTGTCTATTTCGTTCATCCATAGTTGCCTGACTCCCCGTCGTGTAGATAACTACGATA
CGGGAGGGCTTACCATCTGGCCCCAGTGCTGCAATGATACCGCGAGACCCACGCTCACCGGCT
CCAGATTTATCAGCAATAAACCAGCCAGCCGGAAGGGCCGAGCGCAGAAGTGGTCCTGCAAC
TTTATCCGCCTCCATCCAGTCTATTAATTGTTGCCGGGAAGCTAGAGTAAGTAGTTCGCCAGTT
AATAGTTTGCGCAACGTTGTTGCCATTGCTACAGGCATCGTGGTGTCACGCTCGTCGTTTGGTA
TGGCTTCATTCAGCTCCGGTTCCCAACGATCAAGGCGAGTTACATGATCCCCCATGTTGTGCA
AAAAAGCGGTTAGCTCCTTCGGTCCTCCGATCGTTGTCAGAAGTAAGTTGGCCGCAGTGTTAT
CACTCATGGTTATGGCAGCACTGCATAATTCTCTTACTGTCATGCCATCCGTAAGATGCTTTTC
TGTGACTGGTGAGTACTCAACCAAGTCATTCTGAGAATAGTGTATGCGGCGACCGAGTTGCTC
TTGCCCGGCGTCAATACGGGATAATACCGCGCCACATAGCAGAACTTTAAAAGTGCTCATCAT
TGGAAAACGTTCTTCGGGGCGAAAACTCTCAAGGATCTTACCGCTGTTGAGATCCAGTTCGAT
GTAACCCACTCGTGCACCCAACTGATCTTCAGCATCTTTTACTTTCACCAGCGTTTCTGGGTGA
GCAAAAACAGGAAGGCAAAATGCCGCAAAAAAGGGAATAAGGGCGACACGGAAATGTTGAA
TACTCATACTCTTCCTTTTTCAATATTATTGAAGCATTTATCAGGGTTATTGTCTCATGAGCGG
ATACATATTTGAATGTATTTAGAAAAATAAACAAATAGGGGTTCCGCGCACATTTCCCCGAAA

AGTGCCACCTGACGTCTAAGAAACCATTATTATCATGACATTAACCTATAAAAATAGGCGTAT
CACGAGGCCCTTTCGTCTTCAC

B.4 pQE60-pRgpA$_{CAT}$–Z$_{E}$

Plasmid Map

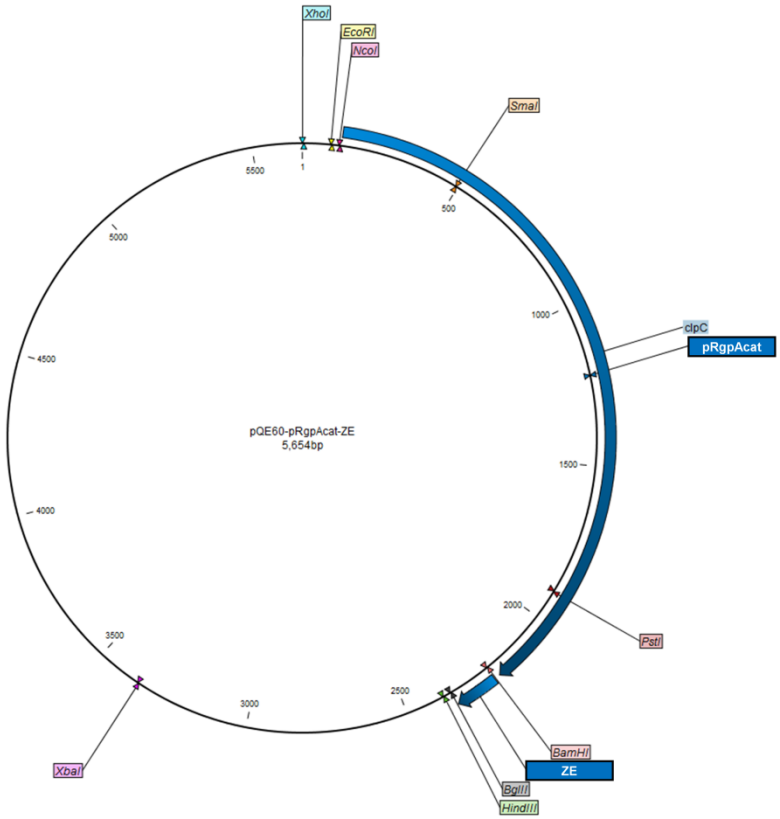

DNA Sequence

CTCGAGAAATCATAAAAAATTTATTTGCTTTGTGAGCGGATAACAATTATAATAGATTCAATT
GTGAGCGGATAACAATTTCACACAGAATTCATTAAAGAGGAGAAATTAACCATGGGTCAGCA
GACAGAGTTGGGACGCAATCCGAATGTGAGATTGCTCGAATCCACTCAGCAATCGGTGACAA
AGGTTCAGTTCCGTATGGACAACCTCAAGTTCACCGAAGTTCAAACCCCTAAGGGAATGGCAC
AAGTGCCGACCTATACAGAAGGGGTTAATCTTTCTGAAAAAGGGATGCCTACGCTTCCCATTC
TATCACGCTCTTTGGCGGTTTCAGACACTCGTGAGATGAAGGTAGAGGTTGTTTCCTCAAAGT
TCATCGAAAAGAAAAATGTCCTGATTGCACCCTCCAAGGGCATGATTATGCGTAACGAAGATC
CGAAAAAGATCCCTTACGTTTATGGAAAGAGCTACTCGCAAAACAAATTCTTCCCGGGAGAG
ATCGCCACGCTTGATGATCCTTTTATCCTTCGTGATGTGCGTGGACAGGTTGTAAACTTTGCGC
CTTTGCAGTATAACCCTGTGACAAAGACGTTGCGCATCTATACGGAAATCACTGTGGCAGTGA
GCGAAACTTCGGAGCAAGGCAAAAATATTCTGAACAAGAAAGGTACATTTGCCGGCTTTGAA
GACACATACAAGCGCATGTTCATGAACTACGAGCCAGGGCGTTACACACCGGTAGAGGAAAA

ACAAAATGGTCGTATGATCGTCATCGTAGCCAAAAAGTATGAGGGAGATATTAAAGATTTCGT
TGATTGGAAAAACCAACGCGGTCTCCGTACCGAGGTGAAAGTGGCAGAAGATATTGCTTCTCC
CGTTACAGCTAATGCTATTCAGCAATTCGTTAAGCAAGAATACGAGAAAGAAGGTAATGATTT
GACCTATGTTCTTTTGATTGGCGATCACAAAGATATTCCTGCCAAAATTACTCCGGGGATCAA
ATCCGACCAGGTATATGGACAAATAGTAGGTAATGACCACTACAACGAAGTCTTCATCGGTCG
TTTCTCATGTGAGAGCAAAGAGGATCTGAAGACACAAATCGATCGGACTATTCACTATGAGCG
CAATATAACCACGGAAGACAAATGGCTCGGTCAGGCTCTTTGTATTGCTTCGGCTGAAGGAGG
CCCATCCGCAGACAATGGTGAAAGTGATATCCAGCATGAGAATGTAATCGCCAATCTGCTTAC
CCAGTATGGCTATACCAAGATTATCAAATGTTATGATCCGGGAGTAACTCCTAAAAACATTAT
TGATGCTTTCAACGGAGGAATCTCGTTGGTCAACTATACGGGCCACGGTAGCGAAACAGCTTG
GGGTACGTCTCACTTCGGCACCACTCATGTGAAGCAGCTTACCAACAGCAACCAGCTACCGTT
TATTTTCGACGTAGCTTGTGTGAATGGCGATTTCCTATTCAGCATGCCTTGCTTCGCAGAAGCC
CTGATGCGTGCACAAAAAGATGGTAAGCCGACAGGTACTGTTGCTATCATAGCGTCTACGATC
AACCAGTCTTGGGCTTCTCCTATGCGCGGGCAGGATGAGATGAACGAAATTCTGTGCGAAAA
ACACCCGAACAACATCAAGCGTACTTTCGGTGGTGTCACCATGAACGGTATGTTTGCTATGGT
GGAAAAGTATAAAAAGGATGGTGAGAAGATGCTCGACACATGGACTGTATTCGGCGACCCCT
CGCTGCTCGTTCGTACACTTGTCCCGACCAAAATGCAGGTTACGGCTCCGGCTCAGATTAATTT
GACGGATGCTTCAGTCAACGTATCTTGCGATTATAATGGTGCTATTGCTACCATTTCAGCCAAT
GGAAAGATGTTCGGTTCTGCAGTTGTCGAAAATGGAACAGCTACAATCAATCTGACAGGTCTG
ACAAATGAAAGCACGCTTACCCTTACAGTAGTTGGTTACAACAAAGAGACGGTTATTAAGAC
CATCAACACTAATGGTGAGCCTAACCCCTACCAGCCTGTTTCCAACTTGACAGCTACAACGCA
GGGTCAGAAAGTAACGCTCAAGTGGGATGCACCGAGCACGAAAACCAATGCAACCACTAATA
CCGCTCGCAGCGTGGATGGCATACGAGAAATGGTTCTTCTGTCAGTCAGCGATGCCCCCGAAC
TTCTTCGCGGTAGTGGATCCCTGGAAATCGAAGCGGCGGCGCTGGAACAGGAAAACACCGCG
CTGGAAACCGAAGTTGCGGAACTGGAACAGGAAGTTCAGCGTCTGGAAAACATCGTTTCTCA
GTACCGTACCCGTTACGGTCCGCTGAGATCTCATCACCATCACCATCACTAAGCTTAATTAGCT
GAGCTTGGACTCCTGTTGATAGATCCAGTAATGACCTCAGAACTCCATCTGGATTTGTTCAGA
ACGCTCGGTTGCCGCCGGGCGTTTTTTATTGGTGAGAATCCAAGCTAGCTTGGCGAGATTTTC
AGGAGCTAAGGAAGCTAAAATGGAGAAAAAAATCACTGGATATACCACCGTTGATATATCCC
AATGGCATCGTAAAGAACATTTTGAGGCATTTCAGTCAGTTGCTCAATGTACCTATAACCAGA
CCGTTCAGCTGGATATTACGGCCTTTTTAAAGACCGTAAAGAAAAATAAGCACAAGTTTTATC
CGGCCTTTATTCACATTCTTGCCCGCCTGATGAATGCTCATCCGGAATTTCGTATGGCAATGAA
AGACGGTGAGCTGGTGATATGGGATAGTGTTCACCCTTGTTACACCGTTTTCCATGAGCAAAC
TGAAACGTTTTCATCGCTCTGGAGTGAATACCACGACGATTTCCGGCAGTTTCTACACATATAT
TCGCAAGATGTGGCGTGTTACGGTGAAAACCTGGCCTATTTCCCTAAAGGGTTTATTGAGAAT
ATGTTTTTCGTCTCAGCCAATCCCTGGGTGAGTTTCACCAGTTTTGATTTAAACGTGGCCAATA
TGGACAACTTCTTCGCCCCCGTTTTCACCATGCATGGGCAAATATTATACGCAAGGCGACAAG
GTGCTGATGCCGCTGGCGATTCAGGTTCATCATGCCGTCTGTGATGGCTTCCATGTCGGCAGA
ATGCTTAATGAATTACAACAGTACTGCGATGAGTGGCAGGGCGGGGCGTAATTTTTTTAAGGC
AGTTATTGGTGCCCTTAAACGCCTGGGGTAATGACTCTCTAGCTTGAGGCATCAAATAAAACG
AAAGGCTCAGTCGAAAGACTGGGCCTTTCGTTTTATCTGTTGTTTGTCGGTGAACGCTCTCCTG
AGTAGGACAAATCCGCCGCTCTAGAGCTGCCTCGCGCGTTTCGGTGATGACGGTGAAAACCTC
TGACACATGCAGCTCCCGGAGACGGTCACAGCTTGTCTGTAAGCGGATGCCGGGAGCAGACA
AGCCCGTCAGGGCGCGTCAGCGGGTGTTGGCGGGTGTCGGGGCGCAGCCATGACCCAGTCAC
GTAGCGATAGCGGAGTGTATACTGGCTTAACTATGCGGCATCAGAGCAGATTGTACTGAGAGT
GCACCATATGCGGTGTGAAATACCGCACAGATGCGTAAGGAGAAAATACCGCATCAGGCGCT
CTTCCGCTTCCTCGCTCACTGACTCGCTGCGCTCGGTCGTTCGGCTGCGGCGAGCGGTATCAGC
TCACTCAAAGGCGGTAATACGGTTATCCACAGAATCAGGGGATAACGCAGGAAAGAACATGT
GAGCAAAAGGCCAGCAAAAGGCCAGGAACCGTAAAAAGGCCGCGTTGCTGGCGTTTTTCCAT
AGGCTCCGCCCCCCTGACGAGCATCACAAAAATCGACGCTCAAGTCAGAGGTGGCGAAACCC
GACAGGACTATAAAGATACCAGGCGTTTCCCCCTGGAAGCTCCCTCGTGCGCTCTCCTGTTCC
GACCCTGCCGCTTACCGGATACCTGTCCGCCTTTCTCCCTTCGGGAAGCGTGGCGCTTTCTCAT
AGCTCACGCTGTAGGTATCTCAGTTCGGTGTAGGTCGTTCGCTCCAAGCTGGGCTGTGTGCAC
GAACCCCCCGTTCAGCCCGACCGCTGCGCCTTATCCGGTAACTATCGTCTTGAGTCCAACCCG
GTAAGACACGACTTATCGCCACTGGCAGCAGCCACTGGTAACAGGATTAGCAGAGCGAGGTA
TGTAGGCGGTGCTACAGAGTTCTTGAAGTGGTGGCCTAACTACGGCTACACTAGAAGGACAGT

ATTTGGTATCTGCGCTCTGCTGAAGCCAGTTACCTTCGGAAAAAGAGTTGGTAGCTCTTGATC
CGGCAAACAAACCACCGCTGGTAGCGGTGGTTTTTTTGTTTGCAAGCAGCAGATTACGCGCAG
AAAAAAAGGATCTCAAGAAGATCCTTTGATCTTTTCTACGGGGTCTGACGCTCAGTGGAACGA
AAACTCACGTTAAGGGATTTTGGTCATGAGATTATCAAAAAGGATCTTCACCTAGATCCTTTT
AAATTAAAAATGAAGTTTTAAATCAATCTAAAGTATATATGAGTAAACTTGGTCTGACAGTTA
CCAATGCTTAATCAGTGAGGCACCTATCTCAGCGATCTGTCTATTTCGTTCATCCATAGTTGCC
TGACTCCCCGTCGTGTAGATAACTACGATACGGGAGGGCTTACCATCTGGCCCCAGTGCTGCA
ATGATACCGCGAGACCCACGCTCACCGGCTCCAGATTTATCAGCAATAAACCAGCCAGCCGG
AAGGGCCGAGCGCAGAAGTGGTCCTGCAACTTTATCCGCCTCCATCCAGTCTATTAATTGTTG
CCGGGAAGCTAGAGTAAGTAGTTCGCCAGTTAATAGTTTGCGCAACGTTGTTGCCATTGCTAC
AGGCATCGTGGTGTCACGCTCGTCGTTTGGTATGGCTTCATTCAGCTCCGGTTCCCAACGATCA
AGGCGAGTTACATGATCCCCCATGTTGTGCAAAAAAGCGGTTAGCTCCTTCGGTCCTCCGATC
GTTGTCAGAAGTAAGTTGGCCGCAGTGTTATCACTCATGGTTATGGCAGCACTGCATAATTCT
CTTACTGTCATGCCATCCGTAAGATGCTTTTCTGTGACTGGTGAGTACTCAACCAAGTCATTCT
GAGAATAGTGTATGCGGCGACCGAGTTGCTCTTGCCCGGCGTCAATACGGGATAATACCGCGC
CACATAGCAGAACTTTAAAAGTGCTCATCATTGGAAAACGTTCTTCGGGGCGAAAACTCTCAA
GGATCTTACCGCTGTTGAGATCCAGTTCGATGTAACCCACTCGTGCACCCAACTGATCTTCAG
CATCTTTTACTTTCACCAGCGTTTCTGGGTGAGCAAAAACAGGAAGGCAAAATGCCGCAAAAA
AGGGAATAAGGGCGACACGGAAATGTTGAATACTCATACTCTTCCTTTTTCAATATTATTGAA
GCATTTATCAGGGTTATTGTCTCATGAGCGGATACATATTTGAATGTATTTAGAAAAATAAAC
AAATAGGGGTTCCGCGCACATTTCCCCGAAAAGTGCCACCTGACGTCTAAGAAACCATTATTA
TCATGACATTAACCTATAAAAATAGGCGTATCACGAGGCCCTTTCGTCTTCAC

APPENDIX C

PRIMER SEQUENCES

Sequences of the Oligonucleotide Primers Used for PCR

Name	Sequence (5’ to 3’)
FZR1	TATCATCCATGGGTCTGGAAATCCGTGCGGCGGCGCTG
RZR1	CGAAGCTTCAGCGGACCGTAACGGGTTTCGTACTG
FZR2	CCGCATGCCGCTGGAAATCCGTGCGGCGGCGCTG
RZR2	TATCATAGATCTCAGCGGACCGTAACGGGTTTCGTACTG
FZE	CTTCGCGGTAGTGGATCCCTGGAAATCGAAGC
RZE	TATCATAGATCTCAGCGGACCGTAACGGGTAC
FMF	TATCATAGATCTATGGTGAGCAAGGGCGAGGAGG
RMF	CAGGGATCCACTACCGCGAAGCTTCGACTTGTACAGCTCGTCCATGC
FEF	TATCATAGATCTATGGCTAGCAAAGGAGAAGAACTCTTC
REF	CAGGGATCCACTACCGCGAAGATTGTACAGTTCATCCATGCCATGTGTAATC
FRGP	TATCATCCATGGGTCAGCAGACAGAGTTGGGACGCAATC
RRGP	CAGGGATCCACTACCGCGAAGAAGTTCGGGGGCATC
FSDM1	GTGCCCGCATGCCGGTCGACCATCATCACCATC
RSDM1	GATGGTGATGATGGTCGACCGGCATGCGGGCAC
FSDM2	CATCACCATCACTAACCTTAATTAGCTGAGC
RSDM2	GCTCAGCTAATTAAGGTTAGTGATGGTGATG
FSDM3	CGGTCCGCTGAGATAACATCACCATCACC
RSDM3	GGTGATGGTGATGTTATCTCAGCGGACCG

REFERENCES

[1] Whitesides, G. M. & Grzybowski, B. Self-assembly at all scales. *Science* **295**, 2418-2421 (2002).

[2] Zhang, S. Fabrication of novel biomaterials through molecular self-assembly. *Nat. Biotechnol.* **21**, 1171-1178 (2003).

[3] Jones, D. S., Silverman, A. P. & Cochran, J. R. Developing therapeutic proteins by engineering ligand–receptor interactions. *Trends Biotechnol.* **26**, 498-505 (2008).

[4] Murphy, K. P., Travers, P., Walport, M. & Janeway, C. *Janeway's immunobiology*. (Garland Science, 2008).

[5] Rozario, T. & DeSimone, D. W. The extracellular matrix in development and morphogenesis: A dynamic view. *Dev. Biol.* **341**, 126-140 (2010).

[6] Hohenester, E. & Yurchenco, P. D. Laminins in basement membrane assembly. *Cell Adh Migr.* **7**, 56-63 (2012).

[7] Fang, P.-A., Conway, J. F., Margolis, H. C., Simmer, J. P. & Beniash, E. Hierarchical self-assembly of amelogenin and the regulation of biomineralization at the nanoscale. *Proc. Natl. Acad. Sci. U. S. A.* **108**, 14097-14102 (2011).

[8] Wallace, D. G. & Rosenblatt, J. Collagen gel systems for sustained delivery and tissue engineering. *Adv. Drug Del. Rev.* **55**, 1631-1649 (2003).

[9] Mano, J. F. *et al.* Natural origin biodegradable systems in tissue engineering and regenerative medicine: present status and some moving trends. *J. R. Soc. Interface* **4**, 999-1030 (2007).

[10] DiMarco, R. L. & Heilshorn, S. C. Multifunctional materials through modular protein engineering. *Adv. Mater.* **24**, 3923-3940 (2012).

[11] Bryksin, A. V., Brown, A. C., Baksh, M. M., Finn, M. G. & Barker, T. H. Learning from nature – Novel synthetic biology approaches for biomaterial design. *Acta Biomater.* **10**, 1761-1769 (2014).

[12] Lutolf, M. P. & Hubbell, J. A. Synthetic biomaterials as instructive extracellular microenvironments for morphogenesis in tissue engineering. *Nat. Biotech.* **23**, 47-55 (2005).

[13] Young, C. L., Britton, Z. T. & Robinson, A. S. Recombinant protein expression and purification: A comprehensive review of affinity tags and microbial applications. *Biotechnol. J.* **7**, 620-634 (2012).

[14] Gräslund, S., et al. Protein production and purification. *Nat. Methods* **5**, 135-146 (2008).

[15] Banta, S., Wheeldon, I. R. & Blenner, M. Protein engineering in the development of functional hydrogels. *Annu. Rev. Biomed. Eng.* **12**, 167-186 (2010).

[16] Stephanopoulos, N., Ortony, J. H. & Stupp, S. I. Self-assembly for the synthesis of functional biomaterials. *Acta Mater.* **61**, 912-930 (2013).

[17] Liu, J. C., Heilshorn, S. C. & Tirrell, D. A. Comparative cell response to artificial extracellular matrix proteins containing the RGD and CS5 cell-binding domains. *Biomacromolecules* **5**, 497-504 (2004).

[18] Silverman, B. R. & Champion, J. A. Presentation of fibronectin fragments using affinity protein interactions for enhanced retention and function. *Acta Biomater.* **10**, 4956-4960 (2014).

[19] Drury, J. L. & Mooney, D. J. Hydrogels for tissue engineering: scaffold design variables and applications. *Biomaterials* **24**, 4337-4351 (2003).

[20] Vo, T. N., Kasper, F. K. & Mikos, A. G. Strategies for controlled delivery of growth factors and cells for bone regeneration. *Adv. Drug Del. Rev.* **64**, 1292-1309 (2012).

[21] Ghosh, K., Ren, X.-D., Shu, X. Z., Prestwich, G. D. & Clark, R. A. Fibronectin functional domains coupled to hyaluronan stimulate adult human dermal fibroblast responses critical for wound healing. *Tissue Eng.* **12**, 601-613 (2006).

[22] Hudalla, G. A. *et al.* Gradated assembly of multiple proteins into supramolecular nanomaterials. *Nat. Mater.* **13**, 829-836 (2014).

[23] Sun, F., Zhang, W.-B., Mahdavi, A., Arnold, F. H. & Tirrell, D. A. Synthesis of bioactive protein hydrogels by genetically encoded SpyTag-SpyCatcher chemistry. *Proc. Natl. Acad. Sci. U. S. A.* **111**, 11269-11274 (2014).

[24] Mitragotri, S. & Lahann, J. Physical approaches to biomaterial design. *Nat. Mater.* **8**, 15-23 (2009).

[25] Decuzzi, P. *et al.* Size and shape effects in the biodistribution of intravascularly injected particles. *J. Control. Release* **141**, 320-327 (2010).

[26] Ilium, L. *et al.* Blood clearance and organ deposition of intravenously administered colloidal particles. The effects of particle size, nature and shape. *Int. J. Pharm.* **12**, 135-146 (1982).

[27] Champion, J. A. & Mitragotri, S. Role of target geometry in phagocytosis. *Proc. Natl. Acad. Sci. U. S. A.* **103**, 4930-4934 (2006).

[28] Champion, J., Walker, A. & Mitragotri, S. Role of particle size in phagocytosis of polymeric microspheres. *Pharm. Res.* **25**, 1815-1821 (2008).

[29] Ingber, D. E. Cellular mechanotransduction: putting all the pieces together again. *FASEB J.* **20**, 811-827 (2006).

[30] Griffin, M. A., Sen, S., Sweeney, H. L. & Discher, D. E. Adhesion-contractile balance in myocyte differentiation. *J. Cell Sci.* **117**, 5855-5863 (2004).

[31] Dalby, M. J., Riehle, M. O., Sutherland, D. S., Agheli, H. & Curtis, A. S. G. Use of nanotopography to study mechanotransduction in fibroblasts – methods and perspectives. *Eur. J. Cell Biol.* **83**, 159-169 (2004).

[32] Matsuurua, K. Rational design of self-assembled proteins and peptides for nano- and micro-sized architectures. *RSC Adv.* **4**, 2942-2953 (2014).

[33] Papapostolou, D. *et al.* Engineering nanoscale order into a designed protein fiber. *Proc. Natl. Acad. Sci. U. S. A.* **104**, 10853-10858 (2007).

[34] Fletcher, J. M. *et al.* Self-assembling cages from coiled-coil peptide modules. *Science* **340**, 595-599 (2013).

[35] Sinclair, J. C., Davies, K. M., Venien-Bryan, C. & Noble, M. E. M. Generation of protein lattices by fusing proteins with matching rotational symmetry. *Nat. Nanotech.* **6**, 558-562 (2011).

[36] Gradišar, H. *et al.* Design of a single-chain polypeptide tetrahedron assembled from coiled-coil segments. *Nat. Chem. Biol.* **9**, 362-366 (2013).

[37] King, N. P. *et al.* Accurate design of co-assembling multi-component protein nanomaterials. *Nature* **510**, 103-108 (2014).

[38] MacKay, J. A. *et al.* Self-assembling chimeric polypeptide-doxorubicin conjugate nanoparticles that abolish tumours after a single injection. *Nat. Mater.* **8**, 993-999 (2009).

[39] Koria, P. *et al.* Self-assembling elastin-like peptides growth factor chimeric nanoparticles for the treatment of chronic wounds. *Proc. Natl. Acad. Sci. U. S. A.* **108**, 1034-1039 (2011).

[40] Slaughter, B. V., Khurshid, S. S., Fisher, O. Z., Khademhosseini, A. & Peppas, N. A. Hydrogels in regenerative medicine. *Adv. Mater.* **21**, 3307-3329 (2009).

[41] Anderson, J. M., Rodriguez, A. & Chang, D. T. Foreign body reaction to biomaterials. *Semin. Immunol.* **20**, 86-100 (2008).

[42] Apostolovic, B., Danial, M. & Klok, H.-A. Coiled coils: attractive protein folding motifs for the fabrication of self-assembled, responsive and bioactive materials. *Chem. Soc. Rev.* **39**, 3541-3575 (2010).

[43] Burkhard, P., Stetefeld, J. & Strelkov, S. V. Coiled coils: a highly versatile protein folding motif. *Trends Cell Biol.* **11**, 82-88 (2001).

[44] Kim, P. S., Berger, B. & Wolf, E. MultiCoil: A program for predicting two-and three-stranded coiled coils. *Protein Sci.* **6**, 1179-1189 (1997).

[45] Vinson, C., Sigler, P. & McKnight, S. Scissors-grip model for DNA recognition by a family of leucine zipper proteins. *Science* **246**, 911-916 (1989).

[46] Murre, C. *et al.* Interactions between heterologous helix-loop-helix proteins generate complexes that bind specifically to a common DNA sequence. *Cell* **58**, 537-544 (1989).

[47] Krylov, D., Mikhailenko, I. & Vinson, C. A thermodynamic scale for leucine zipper stability and dimerization specificity: e and g interhelical interactions. *EMBO J.* **13**, 2849-2861 (1994).

[48] Harbury, P., Zhang, T., Kim, P. & Alber, T. A switch between two-, three-, and four-stranded coiled coils in GCN4 leucine zipper mutants. *Science* **262**, 1401-1407 (1993).

[49] Moll, J. R., Ruvinov, S. B., Pastan, I. & Vinson, C. Designed heterodimerizing leucine zippers with a ranger of pIs and stabilities up to 10(−15) M. *Protein Sci.* **10**, 649-655 (2001).

[50] Zhang, K., Diehl, M. R. & Tirrell, D. A. Artificial polypeptide scaffold for protein immobilization. *J. Am. Chem. Soc.* **127**, 10136-10137 (2005).

[51] Zhang, K., Sugawara, A. & Tirrell, D. A. Generation of surface-bound multicomponent protein gradients. *ChemBioChem* **10**, 2617-2619 (2009).

[52] Diehl, M. R., Zhang, K., Lee, H. J. & Tirrell, D. A. Engineering cooperativity in biomotor-protein assemblies. *Science* **311**, 1468-1471 (2006).

[53] MacEwan, S. R. & Chilkoti, A. Elastin-like polypeptides: Biomedical applications of tunable biopolymers. *Biopolymers* **94**, 60-77 (2010).

[54] Urry, D. W., Trapane, T. L. & Prasad, K. U. Phase-structure transitions of the elastin polypentapeptide–water system within the framework of composition–temperature studies. *Biopolymers* **24**, 2345-2356 (1985).

[55] Reiersen, H., Clarke, A. R. & Rees, A. R. Short elastin-like peptides exhibit the same temperature-induced structural transitions as elastin polymers: implications for protein engineering. *J. Mol. Biol.* **283**, 255-264 (1998).

[56] Christensen, T., Hassouneh, W., Trabbic-Carlson, K. & Chilkoti, A. Predicting transition temperatures of elastin-like polypeptide fusion proteins. *Biomacromolecules* **14**, 1514-1519 (2013).

[57] Kim, W. & Chaikof, E. L. Recombinant elastin-mimetic biomaterials: Emerging applications in medicine. *Adv. Drug Del. Rev.* **62**, 1468-1478 (2010).

[58] McGrath, K. P., Fournier, M. J., Mason, T. L. & Tirrell, D. A. Genetically directed syntheses of new polymeric materials. Expression of artificial genes encoding proteins with repeating -(AlaGly)3ProGluGly- elements. *J. Am. Chem. Soc.* **114**, 727-733 (1992).

[59] Petka, W. A., Harden, J. L., McGrath, K. P., Wirtz, D. & Tirrell, D. A. Reversible hydrogels from self-assembling artificial proteins. *Science* **281**, 389-392 (1998).

[60] Shen, W., Zhang, K., Kornfield, J. A. & Tirrell, D. A. Tuning the erosion rate of artificial protein hydrogels through control of network topology. *Nat. Mater.* **5**, 153-158 (2006).

[61] Shu, X., Shaner, N. C., Yarbrough, C. A., Tsien, R. Y. & Remington, S. J. Novel chromophores and buried charges control color in mFruits. *Biochemistry* **45**, 9639-9647 (2006).

[62] Palm, G. J. *et al.* The structural basis for spectral variations in green fluorescent protein. *Nat. Struct. Biol.* **4**, 361-365 (1997).

[63] O'Brien-Simpson, N. M., Veith, P. D., Dashper, S. G. & Reynolds, E. C. Porphyromonas gingivalis gingipains: the molecular teeth of a microbial vampire. *Curr. Protein Peptide Sci.* **4**, 409-426 (2003).

[64] Calkins, C. C., Platt, K., Potempa, J. & Travis, J. Inactivation of tumor necrosis factor-α by proteinases (gingipains) from the periodontal pathogen, Porphyromonas gingivalis : implications of immune evasion. *J. Biol. Chem.* **273**, 6611-6614 (1998).

[65] Mężyk-Kopeć, R. *et al.* Inactivation of membrane tumor necrosis factor alpha by gingipains from Porphyromonas gingivalis. *Infect. Immun.* **73**, 1506-1514 (2005).

[66] Gross, L. A., Baird, G. S., Hoffman, R. C., Baldridge, K. K. & Tsien, R. Y. The structure of the chromophore within DsRed, a red fluorescent protein from coral. *Proc. Natl. Acad. Sci. U. S. A.* **97**, 11990-11995 (2000).

[67] Stennicke, H. R. & Salvesen, G. S. Caspases: preparation and characterization. *Methods* **17**, 313-319 (1999).

[68] Wang, N. X. & von Recum, H. A. Affinity-based drug delivery. *Macromol. Biosci.* **11**, 321-332 (2011).

[69] Amsden, B. Solute diffusion within hydrogels. Mechanisms and models. *Macromolecules* **31**, 8382-8395 (1998).

[70] Sakiyama-Elbert, S. E. & Hubbell, J. A. Controlled release of nerve growth factor from a heparin-containing fibrin-based cell ingrowth matrix. *J. Control. Release* **69**, 149-158 (2000).

[71] Vulic, K. & Shoichet, M. S. Tunable growth factor delivery from injectable hydrogels for tissue engineering. *J. Am. Chem. Soc.* **134**, 882-885 (2011).

[72] Temenoff, J. S., Shin, H., Conway, D. E., Engel, P. S. & Mikos, A. G. In vitro cytotoxicity of redox radical initiators for cross-linking of oligo(poly(ethylene glycol) fumarate) macromers. *Biomacromolecules* **4**, 1605-1613 (2003).

[73] Kean, T. & Thanou, M. Biodegradation, biodistribution and toxicity of chitosan. *Adv. Drug Del. Rev.* **62**, 3-11 (2010).

[74] Foo, C. T. S. W. P., Lee, J. S., Mulyasasmita, W., Parisi-Amon, A. & Heilshorn, S. C. Two-component protein-engineered physical hydrogels for cell encapsulation. *Proc. Natl. Acad. Sci. U. S. A.* **106**, 22067-22072 (2009).

[75] Bella, A., Ray, S., Shaw, M. & Ryadnov, M. G. Arbitrary self-assembly of peptide extracellular microscopic matrices. *Angew. Chem. Int. Ed.* **51**, 428-431, doi:10.1002/anie.201104647 (2012).

[76] Koutsopoulos, S., Unsworth, L. D., Nagai, Y. & Zhang, S. Controlled release of functional proteins through designer self-assembling peptide nanofiber hydrogel scaffold. *Proc. Natl. Acad. Sci. U. S. A.* (2009).

[77] Toledano, S., Williams, R. J., Jayawarna, V. & Ulijn, R. V. Enzyme-triggered self-assembly of peptide hydrogels via reversed hydrolysis. *J. Am. Chem. Soc.* **128**, 1070-1071 (2006).

[78] Simnick, A. J., Valencia, C. A., Liu, R. & Chilkoti, A. Morphing low-affinity ligands into high-avidity nanoparticles by thermally triggered self-assembly of a genetically encoded polymer. *ACS Nano* **4**, 2217-2227 (2010).

[79] Carlson, J. C. T. *et al.* Chemically controlled self-assembly of protein nanorings. *J. Am. Chem. Soc.* **128**, 7630-7638 (2006).

[80] Lieleg, O. & Ribbeck, K. Biological hydrogels as selective diffusion barriers. *Trends Cell Biol.* **21**, 543-551 (2011).

[81] Cirulis, J. T. *et al.* Fibrillins, fibulins, and matrix-associated glycoprotein modulate the kinetics and morphology of in vitro self-assembly of a recombinant elastin-like polypeptide. *Biochemistry* **47**, 12601-12613 (2008).

[82] Singhal, A., Haynes, C. A. & Hansen, C. L. Microfluidic measurement of antibody-antigen binding kinetics from low-abundance samples and single cells. *Anal. Chem.* **82**, 8671-8679 (2010).

[83] Ciocan, E. & Ciocan, R. Optimized numerical pharmacokinetics model for optical molecular probes based on diffusion coefficients in matrigel measured using fluorescence imaging. *31st Annu. Int. Conf. IEEE EMBS*, 4925-4928 (2009).

[84] Lieleg, O., Baumgärtel, R. M. & Bausch, A. R. Selective filtering of particles by the extracellular matrix: an electrostatic bandpass. *Biophys. J.* **97**, 1569-1577 (2009).

[85] Bird, R. B., Stewart, W. E. & Lightfoot, E. N. *Transport phenomena*. (Wiley, 2006).

[86] Stylianopoulos, T. *et al.* Diffusion of particles in the extracellular matrix: the effect of repulsive electrostatic interactions. *Biophys. J.* **99**, 1342-1349 (2010).

[87] Vitale, S. A. & Katz, J. L. Liquid droplet dispersions formed by homogeneous liquid–liquid nucleation: The ouzo effect. *Langmuir* **19**, 4105-4110 (2003).

[88] Lee, T. A. T., Cooper, A., Apkarian, R. P. & Conticello, V. P. Thermo-reversible self-assembly of nanoparticles derived from elastin-mimetic polypeptides. *Adv. Mater.* **12**, 1105-1110 (2000).

[89] Dreher, M. R. *et al.* Temperature triggered self-assembly of polypeptides into multivalent spherical micelles. *J. Am. Chem. Soc.* **130**, 687-694 (2007).

[90] Kim, W., Thévenot, J., Ibarboure, E., Lecommandoux, S. & Chaikof, E. L. Self-assembly of thermally responsive amphiphilic diblock copolypeptides into spherical micellar nanoparticles. *Angew. Chem. Int. Ed.* **49**, 4257-4260 (2010).

[91] Furgeson, D. Y., Dreher, M. R. & Chilkoti, A. Structural optimization of a "smart" doxorubicin–polypeptide conjugate for thermally targeted delivery to solid tumors. *J. Control. Release* **110**, 362-369 (2006).

[92] Shamji, M. F. *et al.* Development and characterization of a fusion protein between thermally responsive elastin-like polypeptide and interleukin-1 receptor antagonist: Sustained release of a local antiinflammatory therapeutic. *Arthritis Rheum.* **56**, 3650-3661 (2007).

[93] Shamji, M. F. *et al.* Synthesis and characterization of a thermally-responsive tumor necrosis factor antagonist. *J. Control. Release* **129**, 179-186 (2008).

[94] Urry, D. W., Parker, T. M., Reid, M. C. & Gowda, D. C. Biocompatibility of the Bioelastic Materials, Poly(GVGVP) and Its γ-Irradiation Cross-Linked Matrix: Summary of Generic Biological Test Results. *J. Bioact. Compat. Polym.* **6**, 263-282 (1991).

[95] Shen, W. *Structure, dynamics, and properties of artificial protein hydrogels assembled through coiled-coil domains*, California Institute of Technology, (2005).

[96] Silva, E. A. & Mooney, D. J. Effects of VEGF temporal and spatial presentation on angiogenesis. *Biomaterials* **31**, 1235-1241 (2010).

[97] Discher, D. E. & Eisenberg, A. Polymer vesicles. *Science* **297**, 967-973 (2002).

[98] Discher, B. M. *et al.* Polymersomes: tough vesicles made from diblock copolymers. *Science* **284**, 1143-1146 (1999).

[99] Battaglia, G., Ryan, A. J. & Tomas, S. Polymeric vesicle permeability: a facile chemical assay. *Langmuir* **22**, 4910-4913 (2006).

[100] Luo, L. & Eisenberg, A. Thermodynamic size control of block copolymer vesicles in solution. *Langmuir* **17**, 6804-6811 (2001).

[101] Meeuwissen, S. A., Kim, K. T., Chen, Y., Pochan, D. J. & van Hest, J. C. M. Controlled shape transformation of polymersome stomatocytes. *Angew. Chem. Int. Ed.* **50**, 7070-7073 (2011).

[102] Bellomo, E. G., Wyrsta, M. D., Pakstis, L., Pochan, D. J. & Deming, T. J. Stimuli-responsive polypeptide vesicles by conformation-specific assembly. *Nat Mater* **3**, 244-248 (2004).

[103] Holowka, E. P., Pochan, D. J. & Deming, T. J. Charged polypeptide vesicles with controllable diameter. *J. Am. Chem. Soc.* **127**, 12423-12428 (2005).

[104] Vargo, K. B., Parthasarathy, R. & Hammer, D. A. Self-assembly of tunable protein suprastructures from recombinant oleosin. *Proc. Natl. Acad. Sci. U. S. A.* **109**, 11657-11662 (2012).

[105] Leng, Y. *et al.* Integration of a fluorescent molecular biosensor into self-assembled protein nanowires: a large sensitivity enhancement. *Angew. Chem. Int. Ed.* **49**, 7243-7246 (2010).

[106] Amado, E., Schöps, R., Brandt, W. & Kressler, J. Spontaneous formation of giant bioactive protein-block copolymer vesicles in water. *ACS Macro Lett.* **1**, 1016-1019 (2012).

[107] Martín, L., Castro, E., Ribeiro, A., Alonso, M. & Rodríguez-Cabello, J. C. Temperature-triggered self-assembly of elastin-like block co-recombinamers:the controlled formation of micelles and vesicles in an aqueous medium. *Biomacromolecules* **13**, 293-298 (2012).

[108] Cirulis, J. T. & Keeley, F. W. Kinetics and morphology of self-assembly of an elastin-like polypeptide based on the alternating domain arrangement of human tropoelastin. *Biochemistry* **49**, 5726-5733 (2010).

[109] Osborne, J. L., Farmer, R. & Woodhouse, K. A. Self-assembled elastin-like polypeptide particles. *Acta Biomater.* **4**, 49-57 (2008).

[110] Israelachvili, J. N. *Intermolecular and surface forces: revised third edition*. (Elsevier Science, 2011).

[111] Valiaev, A. *et al.* Hydration and conformational mechanics of single, end-tethered elastin-like polypeptides. *J. Am. Chem. Soc.* **130**, 10939-10946 (2008).

[112] Lam, C. N. *et al.* The nature of protein interactions governing globular protein-polymer block copolymer self-assembly. *Biomacromolecules* **15**, 1248-1258 (2014).

[113] Zacharias, D. A., Violin, J. D., Newton, A. C. & Tsien, R. Y. Partitioning of lipid-modified monomeric GFPs into membrane microdomains of live cells. *Science* **296**, 913-916 (2002).

[114] Jenekhe, S. A. & Chen, X. L. Self-assembled aggregates of rod-coil block copolymers and their solubilization and encapsulation of fullerenes. *Science* **279**, 1903-1907 (1998).

[115] Park, S., Lim, J.-H., Chung, S.-W. & Mirkin, C. A. Self-assembly of mesoscopic metal-polymer amphiphiles. *Science* **303**, 348-351 (2004).

[116] Hamley, I. W., Dehsorkhi, A. & Castelletto, V. Self-assembled arginine-coated peptide nanosheets in water. *Chem. Commun.* **49**, 1850-1852 (2013).

[117] Jiang, T. *et al.* Structurally defined nanoscale sheets from self-assembly of collagen-mimetic peptides. *J. Am. Chem. Soc.* **136**, 4300-4308 (2014).

[118] Jiang, T., Xu, C., Zuo, X. & Conticello, V. P. Structurally homogeneous nanosheets from self-assembly of a collagen-mimetic peptide. *Angew. Chem. Int. Ed.* **53**, 8367-8371 (2014).

[119] Nam, K. T. *et al.* Free-floating ultrathin two-dimensional crystals from sequence-specific peptoid polymers. *Nat. Mater.* **9**, 454-460 (2010).

[120] Sanii, B. *et al.* Shaken, not stirred: collapsing a peptoid monolayer to produce free-floating, stable nanosheets. *J. Am. Chem. Soc.* **133**, 20808-20815 (2011).

[121] Sleytr, U. B., Sára, M., Messner, P. & Pum, D. Two-dimensional protein crystals (S-layers): Fundamentals and applications. *J. Cell. Biochem.* **56**, 171-176 (1994).

[122] Andrushchenko, V. V., Vogel, H. J. & Prenner, E. J. Solvent-dependent structure of two tryptophan-rich antimicrobial peptides and their analogs studied by FTIR and CD spectroscopy. *Biochim. Biophys. Acta* **1758**, 1596-1608 (2006).

[123] Barth, A. Infrared spectroscopy of proteins. *Biochim. Biophys. Acta* **1767**, 1073-1101 (2007).

[124] Bigioni, T. P. *et al.* Kinetically driven self assembly of highly ordered nanoparticle monolayers. *Nat. Mater.* **5**, 265-270 (2006).

[125] Currey, J. D. Hierarchies in biomineral structures. *Science* **309**, 253-254 (2005).

[126] Palmer, L. C., Newcomb, C. J., Kaltz, S. R., Spoerke, E. D. & Stupp, S. I. Biomimetic systems for hydroxyapatite mineralization inspired by bone and enamel. *Chem. Rev.* **108**, 4754-4783 (2008).

[127] Politi, Y., Arad, T., Klein, E., Weiner, S. & Addadi, L. Sea urchin spine calcite forms via a transient amorphous calcium carbonate phase. *Science* **306**, 1161-1164 (2004).

[128] Landis, W. J., Silver, F. H. & Freeman, J. W. Collagen as a scaffold for biomimetic mineralization of vertebrate tissues. *J. Mater. Chem.* **16**, 1495-1503 (2006).

[129] Chang, M. C., Ko, C.-C. & Douglas, W. H. Preparation of hydroxyapatite-gelatin nanocomposite. *Biomaterials* **24**, 2853-2862 (2003).

[130] Pouget, E. *et al.* Hierarchical architectures by synergy between dynamical template self-assembly and biomineralization. *Nat. Mater.* **6**, 434-439 (2007).

[131] Dalas, E., Kallitsis, J. K. & Koutsoukos, P. G. Crystallization of hydroxyapatite on polymers. *Langmuir* **7**, 1822-1826 (1991).

[132] Murphy, W. L., Kohn, D. H. & Mooney, D. J. Growth of continuous bonelike mineral within porous poly(lactide-co-glycolide) scaffolds in vitro. *J. Biomed. Mater. Res.* **50**, 50-58 (2000).

[133] Liu, X. *et al.* Multilevel hierarchically ordered artificial biomineral. *Small* **10**, 152-159 (2014).

[134] Zhang, W., Liao, S. S. & Cui, F. Z. Hierarchical self-assembly of nano-fibrils in mineralized collagen. *Chem. Mater.* **15**, 3221-3226 (2003).

[135] Ge, J., Lei, J. & Zare, R. N. Protein-inorganic hybrid nanoflowers. *Nat. Nanotech.* **7**, 428-432 (2012).

[136] Wang, L.-B. *et al.* A new nanobiocatalytic system based on allosteric effect with dramatically enhanced enzymatic performance. *J. Am. Chem. Soc.* **135**, 1272-1275 (2013).

[137] Bommarius, A. S. & Paye, M. F. Stabilizing biocatalysts. *Chem. Soc. Rev.* **42**, 6534-6565 (2013).

[138] Nara, M., Morii, H., Yumoto, F., Kagi, H. & Tanokura, M. Fourier transform infrared spectroscopic study on the Ca2+-bound coordination structures of synthetic peptide analogues of the calcium-binding site III of troponin C. *Biopolymers* **82**, 339-343 (2006).

[139] Kretsinger, R. H. & Nockolds, C. E. Carp muscle calcium-binding protein. II. Structure determination and general description. *J. Biol. Chem.* **248**, 3313-3326 (1973).

[140] Bohner, M. *et al.* Synthesis of spherical calcium phosphate particles for dental and orthopedic applications. *Biomatter* **3**, e25103 (2013).

[141] Miszta, K. *et al.* Hierarchical self-assembly of suspended branched colloidal nanocrystals into superlattice structures. *Nat. Mater.* **10**, 872-876 (2011).

[142] Sacanna, S., Irvine, W. T. M., Chaikin, P. M. & Pine, D. J. Lock and key colloids. *Nature* **464**, 575-578 (2010).

[143] Voorhees, P. W. Ostwald ripening of two-phase mixtures. *Annu. Rev. Mater. Sci.* **22**, 197-215 (1992).

[144] Wilner, O. I. *et al.* Enzyme cascades activated on topologically programmed DNA scaffolds. *Nat. Nanotech.* **4**, 249-254 (2009).

[145] Beutler, B. & Cerami, A. The biology of cachectin/TNF-α primary mediator of the host response. *Annu. Rev. Immunol.* **7**, 625-655 (1989).

[146] Feldmann, M. Pathogenesis of arthritis: recent research progress. *Nat. Immunol.* **2**, 771-773 (2001).

[147] Tabas, I. & Glass, C. K. Anti-inflammatory therapy in chronic disease: challenges and opportunities. *Science* **339**, 166-172 (2013).

[148] Grattendick, K. J., Nakashima, J. M., Feng, L., Giri, S. N. & Margolin, S. B. Effects of three anti-TNF-α drugs: Etanercept, infliximab and pirfenidone on release of TNF-α in medium and TNF-α associated with the cell in vitro. *Int. Immunopharmacol.* **8**, 679-687 (2008).

[149] Mpofu, S., Fatima, F. & Moots, R. J. Anti-TNF-α therapies: they are all the same (aren't they?). *Rheumatology* **44**, 271-273 (2005).

[150] Chowers, Y. & Allez, M. Efficacy of anti-TNF in Crohn's disease: how does it work? *Curr. Drug Targets* **11**, 138-142 (2010).

[151] Moots, R., Taggart, A. & Walker, D. Biologic therapy in clinical practice: enthusiasm must be tempered by caution. *Rheumatology* **42**, 614-616 (2003).

[152] Zalevsky, J. *et al.* Dominant-negative inhibitors of soluble TNF attenuate experimental arthritis without suppressing innate immunity to infection. *J. Immunol.* **179**, 1872-1883 (2007).

[153] Chan, J. M. K. *et al.* Intraarticular gene transfer of TNFR:Fc suppresses experimental arthritis with reduced systemic distribution of the gene product. *Mol. Ther.* **6**, 727-736 (2002).

[154] Pike, R., McGraw, W., Potempa, J. & Travis, J. Lysine- and arginine-specific proteinases from Porphyromonas gingivalis. Isolation, characterization, and evidence for the existence of complexes with hemagglutinins. *J. Biol. Chem.* **269**, 406-411 (1994).

[155] Shi, Y. *et al.* Genetic analyses of proteolysis, hemoglobin binding, and hemagglutination of Porphyromonas gingivalis. Construction of mutants with a combination of rgpA, rgpB, kgp, and hagA. *J. Biol. Chem.* **274**, 17955-17960 (1999).

[156] Guo, Y., Nguyen, K.-A. & Potempa, J. Dichotomy of gingipains action as virulence factors: from cleaving substrates with the precision of a surgeon's knife to a meat chopper-like brutal degradation of proteins. *Periodontol. 2000* **54**, 15-44 (2010).

[157] Eichinger, A. *et al.* Crystal structure of gingipain R: an Arg-specific bacterial cysteine proteinase with a caspase-like fold. *EMBO J.* **18**, 5453-5462 (1999).

[158] Hennet, T., Richter, C. & Peterhans, E. Tumour necrosis factor-alpha induces superoxide anion generation in mitochondria of L929 cells. *Biochem. J* **289**, 587-592 (1993).

[159] Chiu, W.-C., Lai, Y.-P. & Chou, M.-Y. Humanization and characterization of an anti-human TNF-α murine monoclonal antibody. *PLoS One* **6**, e16373 (2011).

[160] He, M. M. *et al.* Small-molecule inhibition of TNF-α. *Science* **310**, 1022-1025, doi:10.1126/science.1116304 (2005).

[161] Voss Jr, E. W., Workman, C. & Mummert, M. Detection of protease activity using a fluorescence-enhancement globular substrate. *BioTechniques* **20**, 286-291 (1996).

[162] Martino, M. M. *et al.* Growth factors engineered for super-affinity to the extracellular matrix enhance tissue healing. *Science* **343**, 885-888 (2014).

[163] Grzelczak, M., Vermant, J., Furst, E. M. & Liz-Marzán, L. M. Directed self-assembly of nanoparticles. *ACS Nano* **4**, 3591-3605 (2010).

[164] Carter, P. J. Introduction to current and future protein therapeutics: A protein engineering perspective. *Exp. Cell Res.* **317**, 1261-1269 (2011).

[165] Yang, J. *et al.* Cell sheet engineering: Recreating tissues without biodegradable scaffolds. *Biomaterials* **26**, 6415-6422 (2005).

[166] Gauthier, O. *et al.* In vivo bone regeneration with injectable calcium phosphate biomaterial: A three-dimensional micro-computed tomographic, biomechanical and SEM study. *Biomaterials* **26**, 5444-5453 (2005).

[167] Inzana, J. A. *et al.* 3D printing of composite calcium phosphate and collagen scaffolds for bone regeneration. *Biomaterials* **35**, 4026-4034 (2014).

VITA

WON MIN PARK

Won Min was born in Seoul, South Korea. He received a B.S. in Chemical Engineering from Hanyang University, Seoul, South Korea in 2007 and a M.S. in Chemical & Biomolecular Engineering from Korea Advanced Institute of Science and Technology, Daejeon, South Korea in 2009. He worked as a research scientist at Korea Institute of Science and Technology, Seoul, South Korea in 2009 before coming to Georgia Institute of Technology to pursue a doctorate in Chemical Engineering.